Nature Communications

https://doi.org/10.1038/s41467-026-71246-w

Article in Press

Cartilage targeting hydrogel nanoplatform degrades BRD4 to alleviate osteoarthritis via Nav1.7 axis

Received: 22 August 2025

Accepted: 16 March 2026

Cite this article as: Zhao, Q., Xu, T., Du, Z. *et al.* Cartilage targeting hydrogel nanoplatform degrades BRD4 to alleviate osteoarthritis via Nav1.7 axis. *Nat Commun* (2026). https://doi.org/10.1038/s41467-026-71246-w

Qirui Zhao, Tongtong Xu, Zuchao Du, Xiaoqing Lu, Yan Zhang, Linjia Peng, Zixuan Gao, Weicheng Wang, Binyu Zhu, Zhigang Liu, Guangjie Yang, Hui Zhao, Zhiming Song, Qiankun Lou, Jiaming Li, Zhiguang Ren, Zhe Yu, Wei Wang, Yanlei Liu, Hui Liang, Jesus M. de la Fuente & Daxiang Cui

Cartilage targeting hydrogel nanoplatform degrades BRD4 to alleviate osteoarthritis via Nav1.7 axis

Qirui Zhao[1,2#], Tongtong Xu[3#], Zuchao Du[4#], Xiaoqing Lu[1,2#], Yan Zhang[2#], Linjia Peng[2], Zixuan Gao[2], Weicheng Wang[5], Binyu Zhu[5], Zhigang Liu[1], Guangjie Yang[1], Hui Zhao[6], Zhiming Song[7], Qiankun Lou[1,2], Jiaming Li[1,2], Zhiguang Ren[2], Zhe Yu[2], Wei Wang[5], Yanlei Liu[5], Hui Liang[2], de la Fuente, Jesus M[5,8], Daxiang Cui[2,5,9*]

[1]Department of Orthopedics, The First Affiliated Hospital of Henan University, Kaifeng 475000, China

[2]Henan Province Engineering Technology Research Center of Intelligent Diagnosis and Treatment, The First Affiliated Hospital, School of Medicine, Henan University, Kaifeng 475000, China.

[3]GCP Lab, The First Affiliated Hospital of Henan University, Kaifeng 475000, China

[4]Department of Hepatopancreatobiliary Surgery, The First Affiliated Hospital of Henan University, School of Medicine, Henan University, Kaifeng, Henan, 475000, China

[5]Institute of Nano Biomedicine and Engineering, School of Sensing Science and Engineering, School of Electronic Information and Electrical Engineering, Shanghai JiaoTong university, Shanghai 200240, China

[6]Department of Vascular Surgery, The First Affiliated Hospital of Henan University, Kaifeng 475000, China

[7]Department of Cardiology, The First Affiliated Hospital of Henan University, Kaifeng 475000, China

[8]Instituto de Nanociencia y Materiales de Aragon, CSIC-University of Zaragoza and CIBER-BBN, University of Zaragoza, Zaragoza 50009, Spain

[9]Henan Intelligent Diagnosis and Treatment Technology Research Engineering Center, Kaifeng

475000, China

[#] These authors are regarded as co-first authors

[*] **Correspondence to:**

Daxiang Cui

E-mail: dxcui@sjtu.edu.cn (**Daxiang Cui)**

Abstract

Osteoarthritis (OA) is a common degenerative joint disease with limited disease-modifying therapies. Emerging evidence suggests that epigenetic dysregulation contributes to cartilage degeneration, but effective strategies to selectively target these pathways remain lacking. Here we show that the BRD4/Nav1.7 axis drives inflammatory and metabolic dysfunction in OA. Integrated single-cell and transcriptomic analyses identify BRD4 as a key regulator that enhances Nav1.7 transcription, promoting mitochondrial impairment and catabolic activation in chondrocytes. To therapeutically target this pathway, we develop a biomimetic hydrogel system incorporating chondrocyte membrane-coated nanoparticles for cartilage-specific delivery of a BRD4 proteolysis-targeting chimera (PROTAC), a molecule designed to induce selective protein degradation. This nanoplatform enables efficient intra-articular delivery, immune evasion and targeted retention in cartilage. Treatment suppresses inflammatory responses, restores mitochondrial function and reduces cartilage degeneration and pain behaviors in two mouse models of OA. These findings establish targeted BRD4 degradation as a disease-modifying strategy and provide a precision nanotherapeutic platform for OA.

Introduction

Osteoarthritis (OA) is the most prevalent degenerative joint disorder and severely impairs the quality of life in middle-aged and elderly populations [1]. It is characterized by cartilage destruction, synovial inflammation, osteophyte formation, and chronic pain, leading to restricted mobility and, in advanced cases, functional disability [2, 3]. With global population aging, the incidence and disability rates of OA have continued to rise, posing a significant public health burden [4, 5]. Current clinical management strategies for OA primarily aim to alleviate symptoms and delay structural deterioration. These approaches include oral nonsteroidal anti-inflammatory drugs (NSAIDs), intra-articular hyaluronic acid injections, and joint replacement surgery [6]. However, these approaches largely remain palliative, lacking precision in targeting underlying disease mechanisms, especially during the early and middle stages when cartilage deterioration may still be reversible [7]. Therefore, there is an urgent need to investigate OA pathogenesis at the molecular level to facilitate the development of critical targeted therapies.

In recent years, the role of epigenetic regulator BRD4 (Bromodomain-containing protein 4) in OA has garnered increasing attention [8, 9]. BRD4 recognizes histone acetylation marks and regulates the transcription of genes involved in inflammatory responses and cellular metabolism, thereby promoting inflammatory activation and extracellular matrix (ECM) degradation in chondrocytes [10, 11]. Studies have shown that BRD4 is highly expressed in OA cartilage, with its elevated activity closely associated with cartilage deterioration [12, 13]. Meanwhile, the voltage-gated sodium channel Nav1.7, traditionally recognized for its role in nociceptive signaling in neurons, has been found to be aberrantly expressed in chondrocytes and implicated in both cartilage dysfunction and pain perception [14-16]. Emerging evidence suggests that BRD4 may contribute to OA progression by modulating Nav1.7 transcriptional activity [14]. However, whether BRD4 activates Nav1.7 expression through epigenetic mechanisms to establish a pathogenic signaling

axis remains unclear and requires further investigation.

From a therapeutic perspective, the emergence of Proteolysis Targeting Chimera (PROTAC) technology has offered a critical approach for targeting "undruggable" proteins [17]. Unlike traditional small-molecule inhibitors, PROTACs induce selective protein degradation by recruiting target proteins to E3 ubiquitin ligases, thereby enabling efficient and sustained elimination of disease-associated proteins [18, 19]. As a nuclear protein, BRD4 is inherently challenging to inhibit efficiently through conventional methods, whereas PROTACs provide a feasible means for its precise modulation [20, 21]. Despite their promise, PROTACs face notable limitations, including high molecular weight, poor membrane permeability, and insufficient tissue specificity, which restrict their performance in complex biological environments [22]. In recent years, stimulus-responsive nano-PROTAC technology has emerged as an innovative therapeutic strategy. By incorporating PROTACs into nanocarriers and integrating internal or external stimuli such as redox conditions, enzymatic activity, or light, this strategy enables spatiotemporal control of protein degradation, thereby enhancing targeting precision, reducing systemic toxicity, and facilitating the clinical translation of PROTAC-based therapies [23]. To further improve therapeutic efficacy, the development of nanocarrier platforms with tissue-targeting capabilities has become a critical breakthrough [24]. Cartilage tissue is characterized by poor vascularization and strong barrier properties, making effective drug penetration and sustained retention highly dependent on intelligent delivery systems. In recent years, multifunctional nanomaterials have been extensively validated for precise drug delivery across complex biological barriers, including the blood-brain barrier and the cartilage barrier, by rational modulation of their physicochemical properties. These advances provide a strong theoretical basis for the design of the drug delivery platform used in the present study [25]. Moreover, highly programmable delivery systems represented by DNA nanostructures have attracted increasing attention as an emerging frontier in biomedicine. Owing

to their excellent biocompatibility and structural design flexibility, DNA-based nanostructures exhibit distinct advantages for the precise delivery of diverse bioactive cargos, including proteins and nucleic acids [26].

Based on these considerations, the present study aimed to elucidate the key mechanism by which BRD4 activates Nav1.7 expression through histone acetylation, thereby promoting cartilage degeneration and OA progression. The study further defined the pathogenic role of the BRD4/Nav1.7 axis in the OA disease process. On this foundation, a cartilage-targeted PROTAC nanodelivery system was developed to achieve precise BRD4 degradation at the epigenetic level, with the objective of intervening at the upstream origin of disease progression. This work not only advances the mechanistic understanding of OA pathogenesis by revealing the noncanonical role of Nav1.7 and its epigenetic regulation, but also provides technical validation for the integration of PROTAC-based protein degradation with targeted nanodelivery strategies in OA. From a clinical perspective, the findings identify critical therapeutic targets and intervention strategies for early cartilage protection, disease modification, and pain alleviation, thereby offering a conceptual and translational framework for precision medicine approaches in degenerative joint diseases.

Results

Identification of Degeneration-Associated Chondrocyte Populations via Single-Cell Sequencing

To systematically identify chondrocyte subpopulations closely associated with OA progression, articular cartilage tissues were harvested from the knee joints of mice in the normal group (Sham surgery) and the OA model group (8 weeks post-destabilization of the medial meniscus [DMM] surgery). scRNA-seq was performed using the 10x Genomics platform (Figure 1A). After stringent quality control, 14,743 cells were retained for downstream analysis, including 7,870 cells from the Sham group and 6,873 cells from the OA group. Data were normalized, followed by PCA for dimensionality reduction and t-distributed stochastic neighbor embedding (t-SNE) for cell clustering. Nineteen distinct cell clusters (Clusters 0–18) were identified (Figure 1B).

Cluster annotation was performed based on established marker gene expression patterns and prior reports [27]. Using Adamts5 and Mmp13 as markers of degenerative chondrocytes, Cluster 4 was annotated as the degenerative chondrocyte population (Figure 1C-D; Supplementary Table 1). Cell proportion analysis revealed a marked increase in both chondrocytes and degenerative chondrocytes, with the latter showing the most pronounced elevation (Figure 1E-F).

Identification of the Key Regulator BRD4 via Transcriptomic Profiling and Marker Gene Integration

To further identify key regulators governing the function of degeneration-associated chondrocytes (Cluster 4), bulk RNA sequencing was performed on cartilage tissues from Sham and OA mice (8 weeks post-DMM surgery) (Supplementary Fig. 1A), with six biological replicates per group (n = 6). RNA integrity was confirmed (RIN > 8.0), followed by standard quality control. Differential expression analysis was conducted using the limma package (v3.56.2), with thresholds

of $log_2FC > 0.5$ or < -0.5 and $p < 0.05$. A total of 689 upregulated and 714 downregulated genes were identified (Supplementary Fig. 1B). Sample clustering results are shown in Supplementary Fig. 1C. GO enrichment analysis revealed that the upregulated genes were significantly associated with pathways such as the negative regulation of cartilage development (Supplementary Fig. 1D-E), suggesting epigenetic and transcriptional dysregulation in OA-associated cartilage degeneration.

To precisely pinpoint key regulators associated with degenerative chondrocytes (Cluster 4), an intersection analysis was conducted between the upregulated genes identified in the degenerative chondrocyte cluster from scRNA-seq and those obtained from bulk RNA-seq. This intersection yielded 18 candidate genes (Supplementary Fig. 1F). PPI network analysis using STRING (v12.0) indicated that BRD4 occupied a central hub position within the network (degree = 15) (Supplementary Fig. 1G) and exhibited strong interactions with epigenetic regulators such as EP300. Previous studies have implicated BRD4 in OA progression [12]. Notably, BRD4 was significantly upregulated in both datasets, with log_2FC values of 1.14 in scRNA-seq and 2.02 in bulk RNA-seq, both reaching statistical significance ($p < 0.05$) (Supplementary Fig. 1H).

Silencing BRD4 Alleviates Mitochondrial Dysfunction in TNF-α-Treated ATDC5 Cells

To evaluate the role of BRD4 in oxidative stress and mitochondrial injury, ATDC5 cells were divided into four groups: Ctrl, TNF-α, TNF-α + sh-NC, and TNF-α + sh-BRD4 (workflow shown in Supplementary Fig. 2A). BRD4 knockdown efficiency was first confirmed. RT-qPCR and WB analyses showed that, compared with the Ctrl group, BRD4 mRNA ($P<0.001$, 95.00% CI=-1.646 to -1.061) and protein ($P<0.001$, 95.00% CI=-3.824 to -3.549) levels were significantly upregulated in the TNF-α group. In contrast, BRD4 mRNA ($P<0.001$, 95.00% CI=0.3041 to 0.8892) and protein ($P<0.001$, 95.00% CI=4.079 to 4.354) expression was markedly reduced in

the TNF-α + sh-BRD4 group compared with the TNF-α + sh-NC group (Supplementary Fig. 2B-C).

Reactive oxygen species (ROS) levels were measured using the DCFH-DA probe. ROS production was significantly elevated in the TNF-α group relative to the Ctrl group (P<0.001, 95.00% CI=-1.343 to -0.8898), whereas it was markedly reduced in the TNF-α + sh-BRD4 group compared to the TNF-α + sh-NC group (P<0.001, 95.00% CI=0.8165 to 1.270) (Supplementary Fig. 2D). TEM revealed pronounced mitochondrial swelling and cristae disruption in the TNF-α group, whereas mitochondrial ultrastructure was notably improved in the TNF-α + sh-BRD4 group, with more preserved cristae compared with the TNF-α + sh-NC group (Supplementary Fig. 2E). Subsequently, JC-1 staining was used to assess changes in ΔΨm. The TNF-α group showed a significant decrease in the JC-1 A/M ratio relative to the Ctrl group (P<0.001, 95.00% CI=0.5565 to 1.084). This reduction was reversed by BRD4 knockdown (P<0.001, 95.00% CI=-1.000 to -0.4731), as evidenced by a significantly increased A/M ratio in the TNF-α + sh-BRD4 group relative to the TNF-α + sh-NC group (Supplementary Fig. 2F-G). Consistently, WB analysis showed that TNF-α markedly reduced the expression of mitochondrial functional proteins TFAM (P<0.001, 95.00% CI=0.8323 to 1.008) and ATP synthase subunit beta (ATPB) (P<0.001, 95.00% CI=0.3754 to 0.6646). In contrast, both TFAM (P<0.001, 95.00% CI=-0.4877 to -0.3123) and ATPB (P=0.001, 95.00% CI=-0.4179 to -0.1287) expression were markedly upregulated in the TNF-α + sh-BRD4 group relative to the TNF-α + sh-NC group (Supplementary Fig. 2H). Immunofluorescence staining produced consistent results, further confirming the improvement in mitochondrial function (Supplementary Fig. 2I-J).

To assess cellular energy metabolism, intracellular ATP levels were quantified. ATP content was significantly reduced in the TNF-α group compared with the Ctrl group (P=0.003, 95.00% CI=0.6229 to 2.384), while BRD4 knockdown notably restored ATP levels in the TNF-α + sh-

BRD4 group compared to the TNF-α + sh-NC group (*P*=0.009, 95.00% CI=-2.100 to -0.3396) (Supplementary Fig. 2K).

Collectively, these data demonstrate that BRD4 silencing effectively suppresses TNF-α-induced ROS accumulation, rescues mitochondrial ultrastructure, stabilizes ΔΨm, and enhances ATP synthesis, indicating a pivotal regulatory role of BRD4 in chondrocyte mitochondrial dysfunction (Supplementary Fig. 2L).

Silencing BRD4 Promotes Anabolic Metabolism and Suppresses Catabolic Activity in TNF-α-Treated ATDC5 Cells

To examine the role of BRD4 in TNF-α-induced metabolic imbalance, ATDC5 cells were assigned to four groups: Ctrl, TNF-α, TNF-α + sh-NC, and TNF-α + sh-BRD4 (workflow shown in Supplementary Fig. 3A). RT-qPCR analysis demonstrated that inflammatory cytokine expression was markedly elevated after TNF-α stimulation, with significant increases in IL-6 (*P*<0.001, 95.00% CI=-4.755 to -4.331) and IL-1β (*P*<0.001, 95.00% CI=-10.11 to -8.839) compared with the Ctrl group. However, their expression was markedly reduced in the TNF-α + sh-BRD4 group relative to the TNF-α + sh-NC group (IL-6: *P*<0.001, 95.00% CI=1.095 to 1.519; IL-1β: *P*<0.001, 95.00% CI=1.479 to 2.747) (Supplementary Fig. 3B). WB analysis further confirmed that IL-6 protein levels were significantly increased in the TNF-α group (*P*<0.001, 95.00% CI=-2.632 to -2.381) and significantly decreased (*P*<0.001, 95.00% CI=3.511 to 3.762) following BRD4 knockdown (Supplementary Fig. 3C). Consistent results from immunofluorescence staining further validated the inhibitory effect of BRD4 silencing on TNF-α-induced inflammation (Supplementary Fig. 3D).

The impact of BRD4 silencing on anabolic metabolism was then evaluated. RT-qPCR showed that Sox9 (*P*<0.001, 95.00% CI=0.2529 to 0.5204) and Col2a1 (*P*<0.001, 95.00% CI=0.4580 to

0.5486) mRNA levels were significantly downregulated in the TNF-α group compared with the Ctrl group, whereas both transcripts were significantly restored in the TNF-α + sh-BRD4 group relative to the TNF-α + sh-NC group (Sox9: $P<0.001$, 95.00% CI=-0.4304 to -0.1629; Col2a1: $P<0.001$, 95.00% CI=-0.4420 to -0.3514) (Supplementary Fig. 3E). WB analysis yielded consistent results, showing that SOX9 ($P<0.001$, 95.00% CI=0.3291 to 0.5509) and COL II ($P<0.001$, 95.00% CI=0.3889 to 0.7045) protein levels were markedly decreased in the TNF-α group and significantly increased after BRD4 silencing (SOX9: $P<0.001$, 95.00% CI=-0.7343 to -0.5124; COL II: $P<0.001$, 95.00% CI=-0.6478 to -0.3322) (Supplementary Fig. 3F). Immunofluorescence staining further demonstrated enhanced SOX9 and COL II signals in the TNF-α + sh-BRD4 group (Supplementary Fig. 3G), indicating restoration of anabolic activity.

To evaluate cartilage matrix degradation, the expression of matrix-degrading enzymes Mmp13, Adamts4, and Adamts5 was assessed. RT-qPCR results showed that mRNA levels of all three genes were significantly downregulated in the TNF-α + sh-BRD4 group (Mmp13: $P<0.001$, 95.00% CI=2.438 to 3.269; Adamts4: $P<0.001$, 95.00% CI=1.831 to 2.602; Adamts5: $P<0.001$, 95.00% CI=0.9654 to 1.201) (Supplementary Fig. 3H). Consistently, WB analysis showed that MMP13 protein expression was markedly increased in the TNF-α group compared with the Ctrl group ($P<0.001$, 95.00% CI=-1.538 to -1.342), and significantly suppressed by BRD4 knockdown ($P<0.001$, 95.00% CI=2.039 to 2.235) (Supplementary Fig. 3I). This expression pattern was further validated by immunofluorescence staining (Supplementary Fig. 3J).

Collectively, these results demonstrate that BRD4 silencing attenuates TNF-α-induced inflammatory responses, restores anabolic metabolism, and suppresses catabolic enzyme expression, thereby contributing to the maintenance of cartilage metabolic homeostasis.

Transcriptomic Profiling Identifies Nav1.7 as a Downstream Target of BRD4

To systematically identify key downstream effectors regulated by BRD4, transcriptome sequencing was performed on ATDC5 cells from the sh-NC and sh-BRD4 groups (workflow shown in Supplementary Fig. 4A). Differential expression analysis was conducted using the limma package (v3.56.2) with a threshold of $|\log_2 FC| > 0.5$ and $p < 0.05$, resulting in 184 upregulated and 392 downregulated genes (Supplementary Fig. 4B-C). GO enrichment analysis revealed that downregulated genes were predominantly associated with "ion transmembrane transport" and "sodium channel activity," indicating that BRD4 knockdown markedly affects ion channel–related functions in chondrocytes (Supplementary Fig. 4D).

Based on the global expression matrix, WGCNA was performed (soft-threshold power = 6; scale-free $R^2 > 0.85$) (Supplementary Fig. 4E). Module-trait relationship analysis identified the blue module as being most strongly correlated with BRD4 knockdown ($R = -0.99$, $p < 0.001$). Genes within this module were filtered using MM > 0.8 and GS > 0.6 and intersected with DEGs, yielding 534 candidate genes (Supplementary Fig. 4F).

To further refine potential target genes, the LASSO regression was applied to the 534 candidates, identifying seven feature genes (Supplementary Fig. 4G). Among them, Scn9a, which encodes the voltage-gated sodium channel Nav1.7, emerged as the most significantly upregulated gene ($\log_2 FC = 1.81$, $p < 0.05$) (Supplementary Fig. 4H). Through the integrated analysis of transcriptomic profiling, WGCNA, and machine learning-based feature selection, Scn9a was identified as a critical downstream effector regulated by BRD4.

Additionally, GSEA of the whole-transcriptome dataset revealed significant downregulation of pathways related to potassium ion channels, the tricarboxylic acid (TCA) cycle and respiratory chain, and ECM metabolism, including collagen synthesis and degradation, following BRD4 depletion (Supplementary Fig. 4I). These results suggest that BRD4 contributes to cartilage degeneration by coordinately regulating ion channel activity, cellular energy metabolism, and

ECM remodeling.

Nav1.7 Expression Is Elevated in OA Chondrocytes and Contributes to Sodium Current Formation

To evaluate the expression pattern of Nav1.7 (encoded by Scn9a) under osteoarthritic conditions, an OA-like cellular model was established by TNF-α treatment of ATDC5 cells. (workflow shown in Figure 2A). RT-qPCR analysis demonstrated a significant upregulation of Scn9a mRNA in the TNF-α group compared with the Ctrl group (P<0.001, 95.00% CI=0.425 to 0.788) (Figure 2B). Consistently, WB analysis revealed a marked increase in Nav1.7 protein expression following TNF-α stimulation (P<0.001, 95.00% CI=7.89 to 8.16) (Figure 2C). Immunofluorescence staining further showed enhanced Nav1.7 fluorescence intensity in TNF-α-treated cells, with prominent localization to the plasma membrane (Figure 2D). To confirm subcellular distribution, membrane and cytoplasmic fractions were isolated for WB analysis. Nav1.7 was predominantly detected in the membrane fraction, and membrane-associated Nav1.7 expression was significantly increased in the TNF-α group (P<0.001, 95.00% CI=2.85 to 3.13) (Figure 2E). These results indicate that Nav1.7 is transcriptionally and translationally upregulated under OA-like conditions and exhibits enhanced membrane localization, consistent with its function as a voltage-gated sodium channel.

Whole-cell patch-clamp recordings were then performed to assess Nav1.7 functional activity. Depolarizing voltage steps from -60 mV to +50 mV elicited robust inward sodium currents (Figure 2F). Compared to the Ctrl group, the TNF-α-treated group exhibited a significantly increased sodium current amplitude (Figure 2G). Application of 1 μM TTX markedly suppressed the inward current, indicating a TTX-sensitive (TTX-S) sodium current consistent with Nav1.7 electrophysiological properties (Figure 2H).

To further verify the specific contribution of Nav1.7, ATDC5 cells were treated with either the non-selective sodium channel blocker TTX (1 μM) or the Nav1.7-selective inhibitor ProTx II (25 nM). Both treatments significantly reduced sodium current amplitudes relative to the TNF-α group (Figure 2I). Normalized and overlaid current traces under TTX and ProTx II conditions displayed highly similar activation and inactivation kinetics (Figure 2J). Kinetic analysis revealed no significant differences between TTX-S and ProTx II-sensitive currents in inactivation time constant (1.00 ± 0.05 ms vs. 1.06 ± 0.08 ms) or time to peak (1.44 ± 0.08 ms vs. 1.52 ± 0.05 ms) (Figure 2K). Together, these findings indicate that the TNF-α-induced sodium current in ATDC5 cells is primarily mediated by Nav1.7, supporting its potential role as a key contributor to OA progression.

Nav1.7 Deletion Alleviates Cartilage Degeneration and Pain-Related Behaviors in OA

To elucidate the role of Nav1.7 in chondrocytes during OA progression, cartilage-specific Nav1.7 knockout mice ($Nav1.7^{chondrocyte}$) and control littermates ($Nav1.7^{flox}$) were generated and subjected to DMM and MIA models to mimic traumatic and chemically induced OA, respectively (workflow shown in Supplementary Fig. 5A). H&E (P<0.001, 95.00% CI=-3.06 to -1.27) and Safranin O staining (P<0.001, 95.00% CI=-2.81 to -1.19) revealed that, in both DMM and MIA models, $Nav1.7^{chondrocyte}$ mice exhibited markedly attenuated cartilage degeneration, improved matrix staining, and significantly lower OARSI scores compared to $Nav1.7^{flox}$ controls (Supplementary Fig. 5B-D). Furthermore, in the DMM model, $Nav1.7^{chondrocyte}$ mice showed reduced osteophyte formation, decreased subchondral bone plate thickening, and significantly lower synovial hyperplasia scores (Supplementary Fig. 5E), indicating that Nav1.7 deletion effectively mitigates OA-associated histopathological changes.

To assess the impact of Nav1.7 deletion on OA-associated pain behaviors, open field tests and

von Frey mechanical stimulation assays were conducted in both DMM and MIA models. In both models, Nav1.7^{chondrocyte} mice displayed significantly increased locomotor activity and higher mechanical withdrawal thresholds compared with Nav1.7^{flox} controls (Supplementary Fig. 5F-G). These findings indicate that the loss of Nav1.7 in chondrocytes exerts a protective effect by alleviating both structural pathology and pain perception in OA.

To further investigate the underlying mechanisms, the expression of key metabolic markers in cartilage tissue was evaluated in both models. Immunohistochemical staining revealed that, relative to Nav1.7^{flox} mice, Nav1.7^{chondrocyte} mice showed significantly increased expression of COL II and ACAN, indicating enhanced anabolic metabolism. Conversely, MMP13 and COMP fragment levels were markedly reduced, reflecting suppression of matrix degradation (Supplementary Fig. 5H-J). These findings indicate that chondrocyte-specific Nav1.7 deletion preserves cartilage homeostasis by promoting matrix synthesis and inhibiting catabolic processes.

Finally, we examined whether Nav1.7 deficiency affected BRD4 expression. The results showed that, compared with the Nav1.7^{flox} group, there was no significant change in BRD4 expression levels in the articular cartilage of the Nav1.7^{chondrocyte} group (Supplementary Fig. 5K-L). These findings indicate that the regulatory role of BRD4 in chondrocytes and OA is independent of Nav1.7.

BRD4 Promotes Nav1.7 Transcriptional Activation Through Histone Acetylation

Based on the preceding bioinformatics analysis, we investigated whether BRD4 regulates Scn9a transcription. ATDC5 cells were divided into four groups: Ctrl, TNF-α, TNF-α + sh-NC, and TNF-α + sh-BRD4 (workflow shown in Figure 3A). RT-qPCR analysis showed that Scn9a mRNA expression was significantly increased in the TNF-α group compared with the Ctrl group (P<0.001, 95.00% CI=-1.019 to -0.6073), while BRD4 knockdown significantly reduced Scn9a

expression relative to the TNF-α + sh-NC group (P<0.001, 95.00% CI=0.8440 to 1.256) (Figure 3B). Consistently, WB analysis revealed that Nav1.7 protein levels were significantly elevated following TNF-α stimulation (P<0.001, 95.00% CI=-0.8013 to -0.5987) and were substantially suppressed by BRD4 silencing (P<0.001, 95.00% CI=1.339 to 1.541) (Figure 3C).

To further examine the functional association between BRD4 and Nav1.7, immunofluorescence co-staining was performed. Compared with the Ctrl group, the TNF-α group exhibited a significant increase in Nav1.7-positive cells (P<0.001, 95.00% CI=-1.863 to -1.250) as well as Nav1.7/BRD4 double-positive cells (P<0.001, 95.00% CI=-1.591 to -0.9419). In contrast, both populations were significantly reduced in the TNF-α + sh-BRD4 group relative to the TNF-α + sh-NC group (P<0.001, 95.00% CI=0.5371 to 1.363) (Figure 3D). These findings suggest that BRD4 knockdown not only inhibits Nav1.7 protein expression but also reduces its co-localization with BRD4, indicating a functional regulatory relationship.

Mechanistically, ChIP-qPCR analysis demonstrated that histone H3 acetylation (H3ac) at the Scn9a promoter was significantly increased in the TNF-α group relative to the Ctrl group, whereas BRD4 knockdown markedly reduced H3ac enrichment compared with the TNF-α + sh-NC group (Figure 3E). Consistent with these findings, dual-luciferase reporter assays showed that Scn9a promoter activity was significantly enhanced by TNF-α treatment (P<0.001, 95.00% CI=-0.533 to -0.234) and significantly suppressed following BRD4 silencing (P<0.001, 95.00% CI=0.197 to 0.496) (Figure 3F).

These results collectively indicate that BRD4 enhances Nav1.7 expression by promoting localized histone acetylation at the Scn9a promoter, thereby increasing its transcriptional activity.

BRD4-Mediated Activation of Nav1.7 Exacerbates Mitochondrial Dysfunction in TNF-α-Treated ATDC5 Cells

To clarify the interplay between BRD4 and Nav1.7 in oxidative stress regulation, TNF-α-treated ATDC5 cells were assigned to four groups: sh-NC, sh-BRD4, OD1 (Nav1.7 activator), and sh-BRD4 + OD1 (workflow shown in Supplementary Fig. 6A). Intracellular ROS levels were assessed using the DCFH-DA fluorescent probe. Compared with the sh-NC group, ROS levels were significantly reduced in the sh-BRD4 group (P<0.001, 95.00% CI=0.3529 to 0.8204), but markedly elevated in the OD1 group (P<0.001, 95.00% CI=-2.264 to -1.796). Notably, ROS levels were also significantly elevated in the sh-BRD4 + OD1 group compared with sh-BRD4 alone (P<0.001, 95.00% CI=-0.9137 to -0.4463) (Supplementary Fig. 6B-C). These findings suggest that activation of Nav1.7 can reverse the inhibitory effect of BRD4 knockdown on ROS production.

Subsequently, ΔΨm was evaluated using JC-1 staining. The JC-1 A/M ratio was significantly increased in the sh-BRD4 group relative to sh-NC (P=0.002, 95.00% CI=0.2543 to 0.8990). In contrast, the A/M ratio was significantly decreased in both the OD1 (P<0.001, 95.00% CI=-1.239 to -0.5943) and sh-BRD4 + OD1 groups (P=0.002, 95.00% CI=-0.8890 to -0.2443) relative to their respective controls (Supplementary Fig. 6D-E). TEM further supported these findings: mitochondria in the sh-BRD4 group displayed more intact cristae and reduced swelling, whereas OD1 treatment induced pronounced cristae disruption, which was further aggravated in the sh-BRD4 + OD1 group (Supplementary Fig. 6F).

To further assess the status of cellular energy metabolism, mitochondrial function-related proteins and intracellular ATP levels were measured. WB analysis revealed that TFAM (P<0.001, 95.00% CI=-0.8297 to -0.6436) and ATPB (P<0.001, 95.00% CI=-1.247 to -1.059) protein levels were significantly increased in the sh-BRD4 group compared with sh-NC. In contrast, both TFAM (P<0.001, 95.00% CI=0.4869 to 0.6731) and ATPB (P<0.001, 95.00% CI=0.1494 to 0.3373) expression were markedly reduced in the OD1 group relative to sh-NC, and in the sh-BRD4 + OD1 group compared to sh-BRD4 alone (TFAM: P<0.001, 95.00% CI=0.9703 to 1.156; ATPB:

P<0.001, 95.00% CI=1.039 to 1.227) (Supplementary Fig. 6G-H). Consistently, ATP quantification revealed a significant increase in the sh-BRD4 group compared with sh-NC (*P*<0.001, 95.00% CI=-2.850 to -1.497), while ATP levels were significantly decreased in the OD1 (*P*=0.01, 95.00% CI=0.1869 to 1.540) and sh-BRD4 + OD1 groups (*P*=0.01, 95.00% CI=-1.573 to -0.2202) compared to their respective controls (Supplementary Fig. 6I). Taken together, these results indicate that BRD4 exacerbates TNF-α-induced ROS accumulation, mitochondrial dysfunction, and energy metabolism disturbances through Nav1.7 activation.

BRD4 Activation of Nav1.7 Suppresses Anabolic Metabolism and Promotes Catabolic Activity in TNF-α-Treated ATDC5 Cells

To delineate the roles of BRD4 and Nav1.7 in inflammatory and metabolic regulation, TNF-α-treated ATDC5 cells were assigned to four groups: sh-NC, sh-BRD4, OD1 (Nav1.7 activator), and sh-BRD4 + OD1 (workflow shown in Supplementary Fig. 7A). RT-qPCR analysis revealed that IL-6 (*P*<0.001, 95.00% CI=0.6360 to 1.257) and IL-1β (*P*<0.001, 95.00% CI=0.5842 to 1.449) mRNA levels were significantly reduced in the sh-BRD4 group compared to the sh-NC group. In contrast, both cytokines were significantly upregulated in the OD1 group relative to sh-NC (IL-6: *P*<0.001, 95.00% CI=-9.284 to -8.663; IL-1β: *P*<0.001, 95.00% CI=-8.072 to -7.208) and in the sh-BRD4 + OD1 group compared to sh-BRD4 alone (IL-6: *P*<0.001, 95.00% CI=1.257 to -0.6360; IL-1β: *P*<0.001, 95.00% CI=-1.389 to -0.5242) (Supplementary Fig. 7B). WB and immunofluorescence analyses corroborated these findings, indicating that Nav1.7 activation counteracts the anti-inflammatory effects of BRD4 knockdown (Supplementary Fig. 7C-D).

The impact on anabolic metabolism was next evaluated. RT-qPCR revealed that Sox9 and Col2a1 were significantly upregulated in the sh-BRD4 group compared with sh-NC (Sox9: *P*<0.001, 95.00% CI=-1.546 to -0.6272; Col2a1: *P*<0.001, 95.00% CI=-1.170 to -0.8100), but

significantly downregulated in the OD1 group (Sox9: $P<0.001$, 95.00% CI=0.1005 to 1.020; Col2a1: $P<0.001$, 95.00% CI=0.3533 to 0.7134) and the sh-BRD4 + OD1 group (Sox9: $P<0.001$, 95.00% CI=0.6272 to 1.546; Col2a1: $P<0.001$, 95.00% CI=0.9133 to 1.273) (Supplementary Fig. 7E). WB analysis further confirmed these findings: SOX9 ($P<0.001$, 95.00% CI=-0.5841 to -0.3492) and COL II ($P<0.001$, 95.00% CI=0.7126 to 0.9474) protein levels were elevated in the sh-BRD4 group but markedly reduced in the OD1 (Sox9: $P<0.001$, 95.00% CI=0.7126 to 0.9474; Col2a1: $P<0.001$, 95.00% CI=0.6473 to 0.8527) and sh-BRD4 + OD1 groups (Sox9: $P<0.001$, 95.00% CI=0.7326 to 0.9674; Col2a1: $P<0.001$, 95.00% CI=0.9073 to 1.113) (Supplementary Fig. 7F).

Immunofluorescence staining revealed enhanced fluorescence intensity of SOX9 and COL II in the sh-BRD4 group, which was markedly reduced following OD1 treatment (Supplementary Fig. 7G), indicating that BRD4 suppresses cartilage anabolic metabolism through Nav1.7 signaling.

To further define the cooperative role of BRD4 and Nav1.7 in catabolic regulation, the expression of matrix-degrading enzymes was examined. RT-qPCR analysis demonstrated that Mmp13, Adamts4, and Adamts5 were significantly downregulated in the sh-BRD4 group compared with the sh-NC group (Mmp13: $P=0.007$, 95.00% CI=0.2505 to 1.389; Adamts4: $P=0.02$, 95.00% CI=0.1315 to 1.495; Adamts5: $P<0.001$, 95.00% CI=0.5507 to 1.049). In contrast, their expression was significantly elevated in both the OD1 group (relative to the sh-NC group) (Mmp13: $P<0.001$, 95.00% CI=-9.519 to -8.381; Adamts4: $P<0.001$, 95.00% CI=-4.478 to -3.115; Adamts5: $P<0.001$, 95.00% CI=-1.026 to -0.5274) and the sh-BRD4 + OD1 group (relative to the sh-BRD4 group) (Mmp13: $P<0.002$, 95.00% CI=-1.599 to -0.4605; Adamts4: $P=0.02$, 95.00% CI=-1.528 to -0.1648; Adamts5: $P<0.001$, 95.00% CI=-1.093 to -0.5940) (Supplementary Fig. 7H). Consistently, WB analysis revealed that BRD4 silencing significantly suppressed MMP13 protein expression, whereas OD1-mediated Nav1.7 activation robustly restored MMP13 levels (all

P<0.001) (Supplementary Fig. 7I). Immunofluorescence staining further confirmed that MMP13-positive signals were strongly enhanced following OD1 stimulation. Although BRD4 knockdown inhibited this upregulation, OD1 treatment partially reversed the effect (Supplementary Fig. 7J).

Collectively, these results indicate that Nav1.7 not only mediates BRD4-driven suppression of anabolic metabolism but also contributes to its promotion of cartilage matrix degradation.

The BRD4-Targeting PROTAC dBET1 Exhibits Low Cytotoxicity and Effectively Induces BRD4 Degradation

To assess the feasibility of pharmacologically targeting BRD4 in chondrocytes, the effects of the PROTAC dBET1 on BRD4 expression and cell viability were evaluated in ATDC5 cells. WB analysis showed that dBET1 markedly reduced BRD4 protein levels at concentrations ≥0.5 μM, with degradation reaching a plateau beyond 1 μM (Supplementary Fig. 8A and Supplementary Fig. 8C). Time-course experiments further demonstrated that 1 μM dBET1 induced a progressive decrease in BRD4 expression, achieving maximal degradation at 24 hours (Supplementary Fig. 8B and S8D). These findings indicate that dBET1 effectively promotes BRD4 degradation in ATDC5 cells in a dose- and time-dependent manner.

Cytotoxicity was then assessed using a CCK-8 assay under two conditions: direct exposure to dBET1 (0.1–10 μM) for 24 hours, and 2-hour dBET1 pretreatment followed by TNF-α (1 μg/mL) co-treatment for 18 hours. Cell viability was significantly reduced only at 10 μM, whereas concentrations between 0.1 and 5 μM showed no significant cytotoxicity (Supplementary Fig. 8E-F). Long-term toxicity assessment further revealed that treatment with 1 μM dBET1 did not induce cytotoxic effects in ATDC5 cells or MSCs over extended culture periods (Supplementary Fig. 8G–H). Collectively, these results demonstrate that dBET1 efficiently induces BRD4 degradation while maintaining a favorable cytotoxicity profile, supporting the selection of 1 μM as the optimal

concentration for subsequent experiments.

Preparation and Characterization of CCM@PM

To develop a cartilage-targeted delivery platform for BRD4 PROTAC, plasma membranes were isolated from P1 primary chondrocytes and used to coat functionalized MSNs (workflow shown in Supplementary Fig. 10A). RT-qPCR analysis showed a progressive reduction in Col2a1 and Acan expression with increasing passage number, whereas Col1a expression remained relatively stable, indicating chondrocyte dedifferentiation and supporting the selection of P1 cells for membrane extraction (Supplementary Fig. 9A). Morphologically, P1 chondrocytes displayed a polygonal shape (Supplementary Fig. 9B). Alcian blue staining confirmed abundant glycosaminoglycan production, and COL II immunofluorescence further verified preservation of the chondrocyte phenotype (Supplementary Fig. 9C). Immunofluorescence analysis demonstrated that P1-derived membranes were enriched in adhesion molecules, including integrin β1, α3, αV, CD44, N-cadherin, and E-cadherin, supporting their suitability for targeted delivery (Supplementary Fig. 9D).

Successful conjugation of the cartilage-targeting peptide to mesoporous silica nanoparticles (PepM) was verified by FTIR analysis. The FTIR spectra of PepM exhibited characteristic absorption peaks corresponding to C=O, C–N, and C–H functional groups, indicating effective peptide modification (Supplementary Fig. 10B). To further evaluate whether PepM mesoporous silica nanoparticles possessed pore structure features suitable for dBET1 loading, nitrogen adsorption-desorption isotherms and pore size distribution analyses were performed. The nitrogen adsorption-desorption isotherms demonstrated that PepM exhibited favorable adsorption capacity across the entire relative pressure range, displaying a typical mesoporous material isotherm, from which the specific surface area parameters were obtained (Supplementary Fig. 11A). Pore size

distribution analysis based on DFT revealed a narrowly distributed pore size range, with a dominant pore diameter in the nanometer scale (Supplementary Fig. 11B), which meets the requirements for dBET1 loading and diffusion. Elution experiments showed that both PM and CCM@PM exhibited slow and reversible release behavior without resistance to elution characteristic of covalent binding, indicating that dBET1 was encapsulated within the nanoparticles via non-covalent interactions (Supplementary Fig. 12). In addition, zeta potential measurements further confirmed alterations in the surface charge properties following modification (Supplementary Fig. 10C).

TEM combined with EDS analysis revealed that PM nanoparticles were spherical with an average diameter of approximately 194 nm, and exhibited nitrogen and sulfur signals, confirming successful organic functionalization (Supplementary Fig. 10D). Fluorescence spectroscopy of FITC-labeled PROTAC-loaded PM showed a characteristic absorption peak at 516 nm, indicating effective drug encapsulation (Supplementary Fig. 10E).

Following incubation of PM with chondrocyte cell membranes, CCM@PM nanoparticles displayed a slightly increased diameter and a dense peripheral coating by TEM. EDS analysis detected uniform phosphorus signals in addition to nitrogen and sulfur, confirming retention of membrane phospholipid components (Supplementary Fig. 10F). Dynamic light scattering (DLS) measurements further confirmed the increase in particle size, supporting successful membrane encapsulation (Supplementary Fig. 10G). Confocal fluorescence imaging demonstrated strong colocalization between FITC-labeled PM (green) and DiI-labeled CCM (red), indicating efficient fusion of the chondrocyte membrane with the nanoparticle surface (Supplementary Fig. 10H). WB analysis confirmed that CCM@PM retained key chondrocyte membrane proteins, including CD44, integrin β1, and N-cadherin (Supplementary Fig. 10I), supporting preservation of biomimetic adhesion and recognition functions critical for targeted cartilage delivery.

CCM@PM Mediates Cartilage-Specific Cellular Uptake via Dual Clathrin-Dependent and Macropinocytic Pathways while Preserving PROTAC Activity

To characterize the cellular uptake of CCM@PM in chondrocytes, Cy5.5-labeled PM, RM@PM, and CCM@PM were incubated with chondrocytes for 2 hours. Confocal microscopy showed markedly stronger intracellular red fluorescence in the CCM@PM group than in the PM or RM@PM groups (Supplementary Fig. 13A). Flow cytometry confirmed a significantly higher mean fluorescence intensity for CCM@PM, indicating that chondrocyte membrane coating substantially enhanced uptake efficiency (Supplementary Fig. 13B-C). In contrast, uptake levels across BMSCs and RAW264.7 macrophages were comparable among all three formulations, suggesting that the CCM coating confers cartilage-specific targeting (Supplementary Fig. 13D).

Endocytic mechanisms underlying CCM@PM internalization were then examined. Cy5.5-labeled CCM@PM was incubated with chondrocytes, followed by addition of transferrin (clathrin-mediated), dextran (macropinocytosis), or cholera toxin (caveolae-mediated) during the final 30 minutes. Confocal imaging revealed strong colocalization of CCM@PM with transferrin and dextran, but minimal overlap with cholera toxin (Supplementary Fig. 13E). Pearson correlation analysis confirmed that CCM@PM was predominantly internalized via clathrin-mediated endocytosis and macropinocytosis (Supplementary Fig. 13F). Consistently, pretreatment with Dynasore (clathrin inhibitor) or Rottlerin (macropinocytosis inhibitor) significantly reduced CCM@PM uptake, whereas other inhibitors had limited effects (Supplementary Fig. 13G).

To determine the contribution of membrane proteins to targeted uptake, CCM@PM was subjected to functional blocking with antibodies against CD44, integrin β1, α1, α3, αV, E-cadherin, and N-cadherin, with trypsin digestion as a positive control. All blocking conditions significantly reduced CCM@PM internalization, with E-cadherin inhibition producing the most pronounced

reduction, approaching the effect of trypsin treatment (Supplementary Fig. 13H).

To compare the extracellular release behavior of PROTACs delivered by different carrier systems, the *in vitro* release kinetics of dBET1 from PM and CCM@PM were first evaluated. The results showed that both formulations exhibited a time-dependent cumulative release profile. However, PM displayed a relatively faster release rate, whereas CCM@PM showed a lower release fraction within the first 12 h (Supplementary Fig. 14A), indicating that cell membrane coating can partially retard premature drug release. To investigate the intracellular trafficking and subcellular localization dynamics of BRD4-PROTAC following cellular internalization, FITC-labeled BRD4-PROTAC was subjected to confocal imaging in conjunction with Rab5 (an early endosome marker) or LAMP1 (a lysosomal marker) staining at different time points. The fluorescence signal of BRD4-PROTAC was predominantly distributed in a punctate pattern at the cell periphery and exhibited pronounced colocalization with Rab5-positive vesicles, suggesting that the PROTAC initially enters cells via classical endocytic pathways and localizes to early endosome-associated compartments (Supplementary Fig. 14B-C). With prolonged incubation, the BRD4-PROTAC fluorescence gradually transitioned from a highly punctate, vesicular distribution to a more diffuse cytoplasmic pattern, accompanied by a reduced degree of overlap with LAMP1-labeled lysosomes and the appearance of fluorescence signals dissociated from lysosomal compartments (Supplementary Fig. 14D-E). These time-resolved imaging results indicate that, following endosomal/lysosomal accumulation, BRD4-PROTAC can undergo partial lysosomal escape and progressively accumulate within the cytosolic space.

The intracellular functional activity of PROTACs following release from the nanoscale delivery systems was further evaluated. WB analysis revealed that treatment with free dBET1 led to a progressive reduction in BRD4 protein levels beginning at 6 h, with near-complete depletion observed at 24-48 h. In comparison, cells treated with PM or CCM@PM also exhibited time-

dependent BRD4 downregulation; however, the degradation kinetics were relatively slower and more gradual (Supplementary Fig. 14F). Quantitative analysis further demonstrated that, at equivalent incubation times, free dBET1 induced the greatest extent of BRD4 degradation, followed by PM and then CCM@PM (Supplementary Fig. 14G). These results indicate that dBET1 retains its BRD4-targeting degradation activity after being released from the nanocarrier systems.

In summary, the cartilage cell membrane coating endows the nanodelivery system with specific cellular recognition and enhanced uptake efficiency, with internalization mediated by membrane protein–dependent clathrin-mediated endocytosis and macropinocytosis. Following cellular entry, the encapsulated PROTAC is capable of escaping lysosomal sequestration, being released into the cytosol, and maintaining its BRD4-degrading activity. Together, these findings demonstrate that CCM@PM offers a significant advantage in achieving precise cellular delivery while preserving the functional efficacy of PROTACs.

Preparation and Characterization of Rh-Gel@CCM@PM

To develop an injectable nanoparticle delivery system with favorable physicochemical properties, this study utilized the natural herbal molecule Rh to form a three-dimensional network hydrogel (Rh-Gel) via non-covalent self-assembly (Figure 4A). Rh was dissolved in sodium bicarbonate buffer at elevated temperature and allowed to cool, yielding a stable red gel. UV-visible spectroscopy showed characteristic absorption peaks at 260 nm and 435 nm, consistent with stable π-π stacking interactions (Figure 4B). Fluorescence analysis showed a prominent emission peak at 592 nm, suggesting densely packed fluorescent aggregates within the hydrogel (Figure 4C). Zeta potential analysis demonstrated that Rh-Gel possessed a moderate surface charge suitable for stable nanoparticle incorporation (Figure 4D). SEM imaging showed a porous three-

dimensional network composed of interwoven nanofibers (Figure 4E). Furthermore, Rh-Gel exhibited temperature-dependent degradation behavior: it gradually degraded over three days at physiological temperature (37°C) but remained stable at 25°C, highlighting its suitability for *in vivo* applications (Figure 4F).

CCM@PM nanoparticles were encapsulated within Rh-Gel to fabricate the Rh-Gel@CCM@PM composite system. UV-visible absorption spectra revealed characteristic peaks corresponding to both Rh and FITC-labeled CCM@PM, indicating successful integration of the two components (Figure 4G). The Zeta potential of the composite shifted toward the characteristic value of CCM, further confirming the successful embedding of CCM@PM into the hydrogel matrix (Figure 4H). Confocal microscopy demonstrated a strong colocalization of the green FITC signal with the red fluorescence of the hydrogel, suggesting uniform distribution and efficient encapsulation of the nanoparticles within the gel network (Figure 4I).

The pH-responsive release behavior of Rh-Gel@CCM@PM was then evaluated. CCM@PM release was markedly accelerated at pH 5.5 compared with pH 7.4, while release under neutral conditions remained relatively slow (Figure 4J). TEM analysis showed that released CCM@PM maintained consistent particle size and structural integrity without aggregation throughout the release process (Figure 4K). WB analysis further confirmed that released nanoparticles retained high levels of key chondrocyte membrane proteins, including CD44, Integrin β1, and N-cadherin, demonstrating preservation of membrane protein structure and function following hydrogel encapsulation (Figure 4L).

To systematically evaluate the mechanical responsiveness and injectability of the Rh-Gel@CCM@PM hydrogel, rheological characterization was first performed. During amplitude sweep measurements, the hydrogel exhibited a typical viscoelastic response in the low-strain region; with increasing strain, the storage modulus gradually decreased and eventually reached a

plateau, indicating structural yielding (Supplementary Fig. 15A). Cyclic shear tests demonstrated that under alternating low- and high-shear conditions, both the storage modulus and loss modulus displayed reproducible and periodic variations, reflecting the reversible mechanical behavior of the hydrogel (Supplementary Fig. 15B). Frequency sweep analysis showed that across the frequency range of 0.1-100 Hz, the storage modulus consistently exceeded the loss modulus, indicating stable frequency-dependent viscoelastic properties (Supplementary Fig. 15C). Time sweep measurements further revealed that under constant strain, both moduli remained relatively stable over time, suggesting good structural integrity (Supplementary Fig. 15D). In addition, viscosity-shear rate analysis indicated pronounced shear-thinning behavior, with viscosity continuously decreasing as the shear rate increased (Supplementary Fig. 15E), supporting the suitability of the hydrogel for injectable applications.

With respect to injectability, the hydrogel could be smoothly extruded through syringes equipped with needles of different gauges. Continuous filamentous or droplet-like gel structures were readily formed using 23G, 25G, and 27G needles (Supplementary Fig. 15F). Photographs of the injection process further illustrated the flow behavior and shape retention of the hydrogel under applied mechanical force (Supplementary Fig. 15G). To evaluate stability under simulated joint cavity conditions, the hydrogel was incubated in synovial fluid–mimicking solution and monitored over time. Macroscopic observation revealed progressive swelling and volumetric changes, accompanied by a gradual color transition of the surrounding medium from transparent to yellow (Supplementary Fig. 15H).

To assess long-term storage stability and suitability for repeated administration, samples stored under a nitrogen atmosphere at 4 °C for 0, 1, 2, 4, and 8 weeks were systematically evaluated for appearance, injectability, and rheological properties. Throughout the 0–8 week storage period, the hydrogel maintained a uniform brown appearance without visible macroscopic alterations

(Supplementary Fig. 16A). Samples from all storage time points could be smoothly extruded through a 27G needle, exhibiting consistent filament formation and droplet behavior (Supplementary Fig. 16B). Shear rheological analysis further demonstrated that all samples retained stable shear-thinning characteristics, with viscosity decreasing as shear rate increased and no noticeable shifts in the viscosity profiles across different storage durations (Supplementary Fig. 16C–G).

In summary, Rh-Gel@CCM@PM exhibits robust structural integrity, acid-responsive behavior, sustained membrane protein retention, and reliable injectability, even after prolonged storage.

Adhesion, Penetration, and Retention Properties of Rh-Gel@CCM@PM in Cartilage Tissue

To assess the contribution of CCM coating to cartilage targeting, the adhesion and distribution of Cy5.5-labeled PM, RM@PM, and CCM@PM were compared in murine cartilage tissue. Fresh cartilage samples were incubated with each formulation for 12 hours, followed by PBS washing and SEM analysis. CCM@PM displayed markedly stronger adhesion to cartilage fibers than PM or RM@PM. Notably, trypsin pretreatment significantly reduced CCM@PM binding, indicating that membrane proteins mediate its high-affinity interaction with cartilage tissue (Supplementary Fig. 17A).

Three-dimensional penetration was further evaluated by confocal imaging of cartilage sections. Both CCM@PM and Rh-Gel@CCM@PM penetrated deeply into the cartilage matrix, whereas PM and RM@PM were largely restricted to superficial layers (Supplementary Fig. 17B). These findings suggest that the CCM structure enhances tissue penetration. For *in vivo* evaluation, a murine knee joint intra-articular injection model was established, and local fluorescence signals were monitored on days 1, 10, 28, and 35 post-injection. Rh-Gel@CCM@PM exhibited the

strongest fluorescence intensity, slowest signal decay, and longest intra-articular retention among all groups. Kinetic analysis revealed a significantly prolonged half-life for Rh-Gel@CCM@PM (Supplementary Fig. 17C-D). Importantly, no detectable fluorescence was observed in major organs for any formulation on days 1 or 10, indicating favorable tissue specificity (Supplementary Fig. 17E).

In summary, Rh-Gel@CCM@PM exhibits good cartilage adhesion, enhanced tissue penetration, and prolonged *in vivo* retention within the joint cavity.

Rh-Gel@CCM@PM Exhibits Favorable Biocompatibility

To systematically evaluate the *in vivo* biocompatibility of Rh-Gel@CCM@PM, mice were subjected to intra-articular injections once weekly for eight consecutive weeks. Treatment groups included Rh-Gel@CCM@PM, Rh-Gel, Rh solution (Rh Sol), and PBS. At the end of the treatment period, blood samples were collected for hematological and serum biochemical analyses. All groups exhibited normal levels of white blood cells (WBC), red blood cells (RBC), and platelets (PLT), as well as liver and kidney function markers, including alanine aminotransferase (ALT), aspartate aminotransferase (AST), blood urea nitrogen (BUN), and creatinine (CRE). No significant differences were detected between the Rh-Gel@CCM@PM group and the PBS control group (Supplementary Fig. 18A-B).

Histological evaluation of major organs was subsequently performed. Heart, liver, spleen, lungs, kidneys, and joint tissues were harvested, paraffin-embedded, and stained with H&E. No signs of inflammation, necrosis, or cellular degeneration were observed in any organs from the Rh-Gel@CCM@PM group. Moreover, no pathological differences were detected compared with the Rh-Gel, Rh Sol, or PBS groups (Supplementary Fig. 18C).

Rh-Gel@CCM@PM Hydrogel Attenuates Mitochondrial Dysfunction in TNF-α-Treated ATDC5 Cells

A TNF-α-induced ATDC5 cell model was established, and cells were assigned to four groups: TNF-α, Rh-Gel, CCM@PM, and Rh-Gel@CCM@PM (workflow shown in Figure 5A). WB analysis demonstrated that, compared with the TNF-α group, both CCM@PM and Rh-Gel@CCM@PM significantly reduced BRD4 protein levels (CCM@PM: $P<0.001$, 95.00% CI=0.5857 to 0.7877; Rh-Gel@CCM@PM: $P<0.001$, 95.00% CI=0.6323 to 0.8343) and Nav1.7 (CCM@PM: $P<0.001$, 95.00% CI=0.4406 to 0.6927; Rh-Gel@CCM@PM: $P<0.001$, 95.00% CI=0.4939 to 0.7461). RT-qPCR analysis showed that Nav1.7 mRNA expression mirrored its protein changes, whereas BRD4 mRNA levels remained unchanged among groups, indicating that BRD4 suppression primarily occurred through post-translational regulation (Figure 5B-D). These findings indicate that Rh-Gel@CCM@PM may exert mitochondrial protective effects by inhibiting the BRD4/Nav1.7 pathway.

To assess intracellular oxidative stress, DCFH-DA fluorescence probes were used to measure ROS accumulation. Compared with the TNF-α group, both the Rh-Gel ($P<0.001$, 95.00% CI=0.3484 to 0.8716) and CCM@PM ($P<0.001$, 95.00% CI=0.6251 to 1.148) groups showed significantly decreased ROS levels. Furthermore, ROS reduction was even more pronounced in the Rh-Gel@CCM@PM group relative to the individual treatment groups ($P=0.04$, 95.00% CI=0.01509 to 0.5382) (Figure 5E). ΔΨm was then evaluated using JC-1 staining. The results demonstrated that, compared with the TNF-α group, both the Rh-Gel ($P=0.004$, 95.00% CI=-0.9097 to -0.2103) and CCM@PM ($P<0.001$, 95.00% CI=-1.446 to -0.7470) groups exhibited significantly increased JC-1 A/M ratios. Importantly, the Rh-Gel@CCM@PM group showed a further significant elevation in A/M ratio compared to the Rh-Gel and CCM@PM groups ($P=0.005$, 95.00% CI=-0.8863 to -0.1870) (Figure 5F-G), suggesting superior preservation of mitochondrial

integrity. TEM revealed that, compared with the TNF-α group, both the Rh-Gel and CCM@PM groups exhibited more intact mitochondrial cristae structures. Notably, cristae morphology was more clearly restored in the Rh-Gel@CCM@PM group, indicating superior mitochondrial preservation (Figure 5H).

To further investigate changes in cellular energy metabolism, we assessed the expression of mitochondrial function-related proteins TFAM and ATPB, along with intracellular ATP levels. WB analysis showed that, relative to the TNF-α group, both Rh-Gel and CCM@PM treatments significantly upregulated TFAM (Rh-Gel: P<0.001, 95.00% CI=-0.6200 to -0.4867; CCM@PM: P<0.001, 95.00% CI=-2.123 to -1.990) and ATPB (Rh-Gel: P<0.001, 95.00% CI=-3.863 to -3.657; CCM@PM: P<0.001, 95.00% CI=-13.40 to -13.19) expression. Notably, Rh-Gel@CCM@PM induced a further and more pronounced upregulation of both TFAM and ATPB compared with either treatment alone (Figure 5I). Consistent with these findings, ATP quantification revealed the highest ATP content in the Rh-Gel@CCM@PM group among all groups tested (Figure 5J).

In addition, we further validated the effects of Rh-Gel@CCM@PM hydrogel on mitochondrial function in TNF-treated HACs. The overall response patterns closely mirrored those observed in ATDC5 cells, confirming that Rh-Gel@CCM@PM effectively alleviates TNF-induced mitochondrial dysfunction in human primary chondrocytes (Supplementary Fig. 19).

Rh-Gel@CCM@PM Hydrogel promotes Anabolic Activity and suppresses Catabolic Processes in Chondrocytes

A TNF-α-stimulated ATDC5 cell model was established to assess anabolic and catabolic regulation under inflammatory conditions. Cells were divided into four groups: TNF-α, Rh-Gel, CCM@PM, and Rh-Gel@CCM@PM (workflow shown in Figure 6A). RT-qPCR analysis revealed that mRNA levels of inflammatory cytokines IL-6 (Rh-Gel: P<0.001, 95.00% CI=0.1245

to 0.3489; CCM@PM: *P*<0.001, 95.00% CI=0.1411 to 0.3655) and IL-1β (Rh-Gel: *P*<0.001, 95.00% CI=0.2884 to 0.7049; CCM@PM: *P*<0.001, 95.00% CI=0.5918 to 1.008) were significantly downregulated in both the Rh-Gel and CCM@PM groups compared with the TNF-α group. Notably, the Rh-Gel@CCM@PM group exhibited a further and more pronounced reduction in these cytokines (Figure 6B). WB analysis confirmed that IL-6 protein levels were lowest in the Rh-Gel@CCM@PM group (Figure 6C), which was further supported by immunofluorescence staining (Figure 6D). Although a quantitative release profile of FITC-dBET1 was not independently presented, the prolonged BRD4 degradation and Nav1.7 inhibition in the Rh-Gel@CCM@PM group compared with free dBET1 indicate effective intracellular release and sustained cytosolic bioavailability of the PROTAC.

Subsequently, key markers of anabolic metabolism were evaluated. RT-qPCR results demonstrated that, compared with the TNF-α group, both Rh-Gel and CCM@PM treatments significantly upregulated mRNA expression of Sox9 (Rh-Gel: *P*=0.004, 95.00% CI=-0.7089 to -0.1644; CCM@PM: P<0.001, 95.00% CI=-2.136 to -1.591) and Col2a1 (Rh-Gel: *P*=0.002, 95.00% CI=-0.4608 to -0.1325; CCM@PM: *P*<0.001, 95.00% CI=-1.454 to -1.126). Importantly, Rh-Gel@CCM@PM treatment led to an even greater increase in these transcripts (Figure 6E). WB analysis revealed corresponding increases in SOX9 and COL II protein expression, again most prominent in the Rh-Gel@CCM@PM group (Figure 6F). Immunofluorescence staining further demonstrated the strongest SOX9 and COL II signals following Rh-Gel@CCM@PM treatment (Figure 6G). These results collectively indicate that Rh-Gel@CCM@PM markedly enhances the anabolic capacity of ATDC5 cells under inflammatory stress.

Catabolic activity was subsequently assessed. RT-qPCR analysis showed that Mmp13, Adamts4, and Adamts5 mRNA levels were significantly reduced in both Rh-Gel and CCM@PM groups compared with TNF-α alone, with further suppression in the Rh-Gel@CCM@PM group

(Figure 6H). Consistent with these findings, WB analysis revealed that MMP13 protein levels were lowest in the Rh-Gel@CCM@PM group (Figure 6I). Immunofluorescence staining further confirmed this trend, showing the weakest MMP13-positive signal in the Rh-Gel@CCM@PM group (Figure 6J-K). These results indicate that Rh-Gel@CCM@PM effectively suppresses the expression of cartilage matrix degradation-associated enzymes, thereby exerting a pronounced anti-catabolic effect. Compared with free dBET1, the Rh-Gel@CCM@PM group exhibited a more sustained therapeutic window for both BRD4 degradation and Nav1.7 inhibition, which was maintained throughout the ≤24 h observation period. This prolonged activity is consistent with the proposed triggered-release mechanism involving gradual release from the Rh-Gel matrix combined with endosomal acidification and intracellular reductive conditions-induced drug release from CCM@PM. These findings indicate that the PROTAC undergoes effective intracellular dissociation and achieves sustained cytosolic availability.

In parallel, we further examined the effects of Rh-Gel@CCM@PM hydrogel on cartilage anabolic and catabolic metabolism in TNF-treated HACs. The overall experimental trends were largely consistent with those observed in ATDC5 cells, demonstrating that Rh-Gel@CCM@PM hydrogel promotes anabolic activity while suppressing catabolic responses in TNF-stimulated human primary chondrocytes (Supplementary Fig. 20).

Rh-Gel@CCM@PM Hydrogel Alleviates Cartilage Damage and Pain-Related Behaviors in DMM-Induced OA Mice

A DMM-induced OA mouse model was established and mice were assigned to five groups: Sham, DMM, Rh-Gel, CCM@PM, and Rh-Gel@CCM@PM (schematic in Figure 7A). To verify the regulatory effect of Rh-Gel@CCM@PM on the BRD4/Nav1.7 axis *in vivo*, WB was performed to assess BRD4 and Nav1.7 expression in knee cartilage tissue. Compared with the Sham group,

the DMM group showed significant upregulation of both BRD4 (P<0.001, 95.00% CI=-2.359 to -2.188) and Nav1.7 (P<0.001, 95.00% CI=-6.820 to -6.666); both were markedly reduced in the Rh-Gel and CCM@PM groups. Notably, the Rh-Gel@CCM@PM group exhibited the most pronounced suppression of BRD4 and Nav1.7 expression (Figure 7B).

Behavioral assessments demonstrated that DMM mice exhibited significantly reduced locomotor distance and decreased mechanical pain thresholds relative to Sham controls. Both parameters were partially improved by Rh-Gel and CCM@PM, whereas Rh-Gel@CCM@PM treatment produced the greatest recovery of locomotor activity and the most pronounced attenuation of pain sensitivity (Figure 7C-D).

Micro-CT analysis revealed severe subchondral bone remodeling in the DMM group, characterized by disorganized trabecular architecture and significantly increased BV/TV (P<0.001, 95.00% CI=-32.35 to -17.58), BMD (P<0.001, 95.00% CI=-25.78 to -14.13), and Tb.Th indices (P<0.001, 95.00% CI=-0.06715 to -0.03619). These abnormalities were partially alleviated in the Rh-Gel and CCM@PM groups, while the Rh-Gel@CCM@PM group showed well-aligned trabecular bone with significantly reduced bone morphometric parameters (Figure 7E-F). H&E and SO/FG staining further demonstrated cartilage deterioration in the DMM group, including reduced cartilage thickness, surface irregularity, and diminished staining intensity. Both Rh-Gel and CCM@PM groups showed partial morphological restoration, whereas the Rh-Gel@CCM@PM group exhibited improved cartilage integrity, with a continuous surface and enhanced staining (Figure 7G). Consistent with these findings, the OARSI score was significantly reduced in the Rh-Gel@CCM@PM group (Figure 7H). Immunofluorescence staining showed that COL II and ACAN levels were increased in the Rh-Gel@CCM@PM group, while IL-6 expression was significantly suppressed, indicating enhanced matrix preservation and reduced inflammation (Figure 7I).

Rh-Gel@CCM@PM Hydrogel Alleviates Cartilage Damage and Pain-Related Behaviors in MIA-Induced OA Mice

A mouse model of OA was established using MIA, and animals were assigned to five groups: Sham, MIA, Rh-Gel, CCM@PM, and Rh-Gel@CCM@PM to evaluate the therapeutic effects of each intervention on OA progression (schematic in Figure 8A). Behavioral assessments showed that, compared with the Sham group, MIA mice exhibited markedly reduced locomotor activity and significantly lower mechanical pain thresholds. Both Rh-Gel and CCM@PM partially improved these deficits, whereas Rh-Gel@CCM@PM produced the most pronounced recovery, with behavioral outcomes approaching those of the Sham group (Figure 8B-C). These findings suggest that Rh-Gel@CCM@PM effectively mitigates MIA-induced behavioral abnormalities and chronic pain.

Micro-CT analysis revealed severe subchondral bone remodeling in the MIA group, characterized by disorganized trabeculae and significantly increased BV/TV (P<0.001, 95.00% CI=-31.56 to -14.40), BMD (P<0.001, 95.00% CI=-22.41 to -15.83), and Tb.Th indices (P<0.001, 95.00% CI=-0.07014 to -0.03320). These abnormalities were moderately alleviated by Rh-Gel or CCM@PM, while Rh-Gel@CCM@PM restored near-normal trabecular architecture with significant reductions in all bone morphometric parameters (Figure 8D-E). Histological staining further confirmed cartilage deterioration in the MIA group, characterized by reduced cartilage thickness, surface roughness, and diminished staining intensity. Rh-Gel and CCM@PM treatments attenuated cartilage damage to varying degrees. In contrast, the Rh-Gel@CCM@PM group exhibited markedly improved cartilage morphology, including a smoother surface, greater thickness, and uniform staining (Figure 8F). Quantitative analyses demonstrated that the Rh-Gel@CCM@PM group had the lowest OARSI score and the highest GAG content and cartilage

thickness among all groups (Figure 8G-I).

To validate the joint-protective mechanism, the expression levels of BRD4 and Nav1.7 proteins in joint tissues were examined. WB analysis revealed that BRD4 (P<0.001, 95.00% CI=-2.807 to -2.693) and Nav1.7 (P<0.001, 95.00% CI=-6.803 to -6.674) expression were significantly elevated in the MIA group compared to the Sham group. Treatment with either Rh-Gel or CCM@PM significantly reduced the expression of both proteins, while Rh-Gel@CCM@PM led to an even more pronounced downregulation (Figure 8J). Immunofluorescence staining further demonstrated that Rh-Gel@CCM@PM treatment markedly enhanced the expression of COL II and ACAN while significantly suppressing IL-6 levels, indicating its superior regulatory effects on anabolic metabolism and inflammatory responses (Figure 8K). Collectively, these findings suggest that Rh-Gel@CCM@PM delays MIA-induced OA progression by suppressing the BRD4/Nav1.7 axis, preserving cartilage matrix homeostasis, and alleviating subchondral bone remodeling disorders.

Discussion

In the study of OA pathogenesis, the epigenetic regulator BRD4 has increasingly been recognized as a potential central contributor [10, 13]. Previous research has largely focused on the pro-inflammatory role of BRD4, demonstrating that it drives synovial inflammation and cartilage matrix degradation by regulating inflammatory cytokines and matrix-degrading enzymes such as IL-6 and MMPs [11, 28]. Building on these findings, the present study further elucidates an epigenetic mechanism by which BRD4 regulates Nav1.7 expression at the chondrocyte level. Specifically, the results demonstrate that BRD4 enhances the transcriptional expression of Scn9a (Nav1.7) by promoting histone acetylation at its promoter region. This discovery broadens the functional scope of BRD4 in OA and indicates that, beyond its established involvement in inflammatory signaling networks, BRD4 may also modulate chondrocyte function by regulating ion channel expression, thereby influencing metabolic homeostasis.

This study systematically proposes the involvement of the BRD4/Nav1.7 axis in OA and establishes a direct regulatory relationship through integrated multi-omics analyses and functional validation. Previous investigations into OA pathogenesis have largely focused on inflammatory cytokine activation or mechanical stress–related pathways, while the contributions of ion channel regulation and metabolic intervention have received limited attention [29, 30]. Using approaches such as ChIP-qPCR and dual-luciferase reporter assays, this study confirms that BRD4 directly associates with the Nav1.7 promoter and transcriptionally activates its expression. On this basis, we propose a regulatory framework in which BRD4-dependent histone acetylation enhances Nav1.7 transcription, thereby contributing to metabolic dysregulation in chondrocytes. This conceptual advance supports a shift in OA research from a predominantly inflammation-centered model toward an integrated epigenetic-ion channel regulatory paradigm.

At the therapeutic level, although PROTAC technology has gained traction in oncology, its

application in degenerative diseases such as OA remains unexplored. In this study, we introduce a BRD4-targeting PROTAC into the OA treatment paradigm and demonstrate its ability to efficiently degrade BRD4, leading to marked suppression of downstream Nav1.7 expression and restoration of chondrocyte metabolic homeostasis. Compared with conventional BRD4 inhibitors (e.g., JQ1), the targeted protein degradation strategy circumvents functional recovery mediated by residual protein pools, rendering it more suitable for long-term regulation in chronic diseases.

Furthermore, we developed the Rh-Gel@CCM@PM by integrating MSNs, biomembrane coating, and a herbal hydrogel matrix. This multifunctional platform significantly enhances the tissue penetration and stability of PROTACs. In contrast to conventional liposome- or polymer-based carriers, which often lack targeting specificity and may induce systemic toxicity, this system preferentially accumulates in articular cartilage, enabling low-dose, highly targeted therapy with minimal adverse effects, representing a substantial advancement in OA drug delivery strategies. Importantly, the hydrogel maintains a stable gel state under synovial fluid-mimicking conditions at 37°C and exhibits favorable injectability and shape retention, rendering it theoretically suitable for repeated intra-articular administration. Consistent with this premise, no joint blockage or gel displacement was observed following repeated injections over an 8-week period, supporting the feasibility and safety of long-term use.

With respect to the release kinetics and intracellular bioavailability of BRD4-PROTAC, although FITC-labeled PROTAC was not employed for direct quantitative release analysis or visualization of endosomal escape, the functional outcomes provide strong indirect evidence. Compared with free dBET1, the Rh-Gel@CCM@PM group exhibited more sustained BRD4 degradation and prolonged suppression of Nav1.7 expression, accompanied by persistent improvements in mitochondrial function and cellular metabolic status. This temporal consistency aligns well with the prolonged intra-articular retention and staged release behavior of the delivery

system, supporting the conclusion that the PROTAC remains cytosolically available and functionally active following intracellular release.

In addition, although self-assembled rhein-based hydrogels (Rh-Gel) have been reported in previous studies [31-33], Rh-Gel in the present system does not merely serve as a generic hydrogel matrix but instead fulfills indispensable and non-redundant functions. First, Rh-Gel exhibits characteristic shear-thinning behavior and in situ gelation capability, enabling smooth injectability while rapidly transitioning into a gel state after intra-articular administration. This property markedly prolongs residence on the cartilage surface and establishes a staged release microenvironment, thereby ensuring stable and sustained BRD4 PROTAC activity within the joint. Second, compared with PM or CCM@PM alone, incorporation of Rh-Gel significantly reduces mechanical washout during joint motion, providing effective "shear protection" for the encapsulated payload. This contribution is reflected in the graded therapeutic efficacy observed among the PM, CCM@PM, and Rh-Gel@CCM@PM groups.

Meanwhile, MSNs were selected as the core carrier primarily due to their tunable and well-defined pore architecture, which is particularly suitable for efficient loading of macromolecular PROTACs. Their favorable surface chemistry also facilitates stable cell membrane coating, thereby conferring cartilage-targeting capability. Moreover, the controlled release behavior of MSNs is well aligned with the in situ sustained-release mechanism of Rh-Gel, allowing synergistic coupling between the two components. In contrast, liposomal systems are prone to membrane destabilization in synovial fluid, whereas polymer-based carriers often suffer from batch-to-batch variability and inconsistent degradation profiles, which may compromise payload stability, injection reproducibility, and translational controllability. Collectively, the integration of Rh-Gel and MSNs achieves a more favorable balance among stability, sustained release, local retention, and safety, providing clear advantages for further preclinical development.

Although an independent *in vitro* elution profile was not generated in this study, Rh-Gel@CCM@PM exhibited stable pharmacological efficacy and sustained intra-articular retention throughout the continuous 8-week dosing regimen *in vivo*, with no evidence of rapid therapeutic attenuation or particle clearance from the joint cavity. These functional outcomes provide indirect but meaningful support for the stability of drug loading under physiological conditions. Mechanistically, drug release is driven by coordinated processes, including staged exudation from the in situ–formed hydrogel within the joint space, endosomal acidification, and the intracellular reductive environment, collectively enabling noncovalent dissociation of the PROTAC from CCM@PM and subsequent cytosolic entry. Although direct visualization of PROTAC release or endosomal escape using FITC-labeled constructs was not presented, functional readouts offer a comparable form of "release kinetics evidence." Compared with free dBET1, Rh-Gel@CCM@PM induced more sustained BRD4 degradation and prolonged metabolic recovery, with a temporal profile closely matching its local retention and staged-release behavior. Collectively, these observations indicate that the PROTAC remains cytosolically active and achieves effective intracellular action. Future studies will incorporate labeled PROTACs to directly characterize *in vitro* release dynamics and endosomal escape, enabling more refined validation of the delivery process.

Regarding membrane source–dependent variability, neonatal, adult, and osteoarthritic cartilage may differ in receptor density, integrin and adhesion profiles, and glycosylation patterns, potentially influencing interactions between membrane-camouflaged nanoparticles and cartilage matrix or cells. In this study, P1-derived CCM was selected to ensure membrane structural integrity and preparation consistency. Importantly, the robust intra-articular retention and therapeutic efficacy observed in disease models, together with molecular and phenotypic validation in human primary chondrocytes, support the translational relevance of this strategy in

adult and OA settings. Future work will systematically compare membranes derived from adult or OA cartilage sources and assess their effects on cellular uptake, tissue retention, and therapeutic outcomes, thereby further strengthening the translational foundation of this delivery platform.

In terms of *in vitro* and *in vivo* functional validation, this study employed a TNF-α–induced ATDC5 inflammatory model together with two murine OA models (DMM and MIA) to comprehensively evaluate therapeutic efficacy across multiple dimensions, including cellular metabolism, mitochondrial function, matrix synthesis, and pain-related behaviors. The results demonstrated clear advantages in cartilage protection, metabolic restoration, and pain alleviation. This full-spectrum research approach, encompassing mechanistic exploration, therapeutic intervention, and outcome evaluation, enhanced the study's credibility and translational potential and provided a solid foundation for future preclinical development. Furthermore, validation in human primary chondrocytes confirmed that the dBET1-loaded hydrogel modulates the BRD4/Nav1.7 axis and preserves cartilage matrix homeostasis, supporting cross-species consistency and underscoring the potential clinical feasibility of this therapeutic strategy.

BRD4 contains two bromodomains (BD1 and BD2) that recognize acetylated lysine residues and mediate chromatin association, as well as a histone acetyltransferase (HAT) domain capable of catalyzing histone lysine acetylation [34]. In the present study, TNF-α stimulation markedly increased histone H3ac at the Scn9a promoter, whereas BRD4 knockdown significantly reduced H3ac enrichment at this locus (Figure 3E). In conjunction with previous reports, these findings suggest that BRD4-mediated regulation of Scn9a promoter activity may be closely associated with changes in local H3 acetylation. Moreover, BRD4 has been shown to bind chromatin by recognizing acetylated histone lysine residues and to directly recruit distinct transcription factors, thereby facilitating transcriptional activation of target promoters [35-37]. Consistent with this mechanism, we observed that TNF-α markedly enhanced Scn9a promoter activity, while BRD4

silencing led to a pronounced suppression of promoter-driven transcription (Figure 3F). Collectively, these data support a model in which BRD4 activates Scn9a transcription through histone acetylation–dependent chromatin engagement and transcription factor recruitment. Identification of the specific transcription factors involved in this BRD4-dependent regulatory process will be a key focus of future studies.

Nav1.7 is a voltage-gated sodium channel that has traditionally been regarded as a key mediator of electrical signal transmission and pain perception in neurons [38, 39]. In recent years, a limited number of studies have reported Nav1.7 expression in non-neuronal tissues, although its functional relevance in these contexts has remained largely unclear [14]. Notably, emerging evidence has demonstrated the presence of Nav1.7 in chondrocytes and implicated its involvement in joint degeneration, highlighting the potential importance of ion channels in regulating pathological metabolism within joint tissues [14]. Previous studies have suggested that voltage-gated sodium channels may influence cellular metabolic homeostasis by modulating membrane excitability, ionic influx, and mitochondrial membrane potential dynamics [30]. Nevertheless, the precise signaling nodes through which Nav1.7 operates in chondrocytes remain to be elucidated. In the present study, we establish that elevated Nav1.7 expression in chondrocytes is functionally significant and closely associated with mitochondrial dysfunction and metabolic imbalance. These findings extend the role of Nav1.7 beyond that of a canonical “pain target” to that of a potential “metabolic regulator” and implicate Nav1.7 as a previously underappreciated contributor to cartilage degeneration. More broadly, this work provides insights into the involvement of ion channels in non-neuronal pathological processes. However, the specific molecular pathways by which Nav1.7 upregulation impacts mitochondrial function and cellular energy metabolism warrant further investigation.

Overall, this study further elucidates the mechanistic role of BRD4 in OA progression by

demonstrating that BRD4 regulates Scn9a (Nav1.7) transcription through enhanced histone acetylation at its promoter region. A pathogenic role of the BRD4/Nav1.7 axis in chondrocyte metabolic dysregulation is proposed and experimentally validated. In parallel, a cartilage-targeting drug delivery system is developed to enable efficient BRD4 degradation and effective suppression of downstream signaling pathways (Figure 9). Scientifically, this work advances the integration of epigenetic regulation and ion channel function in OA pathophysiology. Technologically, it demonstrates the feasibility of combining PROTAC-based protein degradation with targeted delivery strategies. Clinically, it offers critical directions for early OA intervention and pain management. Nevertheless, several limitations remain. Long-term toxicity and immunogenicity have not yet been systematically evaluated. Future studies will focus on quantifying targeting specificity through receptor-blocking or competitive binding assays, as well as comparisons between homologous and heterologous membrane sources. Comprehensive evaluations of systemic biodistribution, pharmacokinetics, and organ toxicity, including long-term and repeated dosing studies, will also be required. In addition, comparative validation using adult- or OA-derived membrane sources will be performed to further strengthen evidence for targeting precision and long-term safety. Moreover, validation will be expanded using clinical samples and large-animal models, and interactions between BRD4 and other ion channels or metabolic regulators will be explored to deepen mechanistic understanding and broaden the therapeutic applicability of the proposed strategy.

Methods

Ethical Statement

All animal experiments were approved by the Animal Ethics Committee of The First Affiliated Hospital of Henan University (No. 2025-03-069). All procedures complied with the Guide for the Care and Use of Laboratory Animals.

Single-Cell RNA Sequencing (scRNA-seq)

Cells were isolated from the knee cartilage tissue of C57BL/6J mice in the sham-operated (control) group and the OA model group (eight weeks post-destabilization of the medial meniscus (DMM) surgery) (n=1 per group). Single-cell suspensions were prepared using a three-step digestion protocol with collagenase II (Sigma, C6885) and collagenase D (Roche, 11088858001). Single-cell capture and cDNA library construction were performed on the 10x Genomics Chromium platform (Single Cell 3' Reagent Kits v3.1). Raw sequencing data were aligned to the reference genome (GRCm38 mm10) using Cell Ranger (v6.1.2). Stringent quality control was applied to retain cells with 200–4000 detected genes, while cells with more than 10% mitochondrial gene content were excluded.

Single-Cell Data Analysis

Data analysis was conducted using the Seurat package (v5.1.0) in R (v4.3.0). Quality control filters were set to retain cells with 200-6000 detected genes and mitochondrial gene content below 10%. Gene expression data were normalized using the LogNormalize method with a scaling factor of 10,000, and the top 2000 highly variable genes were identified using the vst method. Dimensionality reduction was performed by principal component analysis (PCA) based on 50 principal components (PCs), with the top 30 PCs selected via ElbowPlot. Batch effects associated

with sample origin (orig.ident) were corrected using the Harmony algorithm. Clustering was conducted based on the top 30 Harmony-corrected PCs, and the optimal resolution parameter (0.4) was determined through multiresolution comparison using the clustree method. Marker gene identification and differential expression analysis were performed with thresholds set at min.pct = 0.25 and logfc.threshold = 0.25, retaining only significantly upregulated genes. All analyses were performed using R (v4.3.0). Because the sample size for each group was n = 1, single-cell sequencing was used solely for cell type identification and cell state characterization, rather than for cross-group statistical inference. The Harmony algorithm (v1.2.0) was applied solely to remove technical batch effects associated with sample origin and to enable joint visualization in a unified low-dimensional space. Key differential conclusions were derived from bulk RNA sequencing data with biological replicates and were further supported by subsequent functional validation experiments.

Transcriptome Sequencing and Analysis

Full-thickness cartilage was collected from the knee joints of mice in the sham group and the OA group (eight weeks post-DMM surgery) (n=6 per group). Total RNA was extracted using TRIzol reagent (Invitrogen), and RNA integrity was verified with an Agilent 2100 Bioanalyzer, ensuring a RIN > 8.0. RNA libraries were constructed using the NEBNext Ultra II RNA Library Prep Kit and sequenced on the Illumina NovaSeq 6000 platform with 150 bp paired-end reads, targeting a depth of 40 million reads per sample. Raw data were quality-checked using FastQC (v0.11.9), aligned to the mm10 reference genome with Hisat2 (v2.2.1), and quantified using featureCounts (v2.0.3). Differential expression analysis was performed with the limma package (v3.56.2) in R (v4.3.0), applying the voom method for normalization. Genes with $|\log_2 \text{fold change}| > 0.5$ and $p < 0.05$ were considered significantly differentially expressed.

Gene Ontology (GO) Enrichment Analysis

GO enrichment analysis was conducted on the differentially expressed genes (DEGs) identified from bulk RNA-seq using the clusterProfiler package (v4.6.2) in R (v4.3.0). Gene annotation was based on the org.Mm.eg.db database (v3.16.0). Statistical significance of enrichment was assessed using the hypergeometric test, with *p*-values adjusted by the Benjamini-Hochberg method (adjusted $p < 0.05$). Visualization was carried out using enrichplot (v1.18.4), with the top 20 most significantly enriched pathways displayed (showCategory = 20).

Visualization of Gene Overlap

To illustrate the overlap between genes specifically upregulated in degeneration-associated chondrocyte clusters identified by single-cell analysis (min.pct = 0.25, logfc.threshold = 0.25) and DEGs from bulk RNA-seq ($|\log_2 FC| > 0.5$, *p*-value < 0.05), a Venn diagram was generated using the Microbioinformatics online analysis platform (http://www.bioinformatics.com.cn). Two gene lists derived from the single-cell and transcriptome datasets were used as input, and the diagram was produced with default parameters.

Protein-Protein Interaction (PPI) Network Analysis

The PPI network of the intersecting genes was constructed using the STRING database (v12.0), with a confidence score threshold of 0.400. The resulting network file was imported into Cytoscape (v3.9.1) for topological analysis. Node degree and betweenness centrality were calculated using the CytoHubba plugin (v0.1). Core nodes were defined as those within the top 10% ranked by degree.

Weighted Gene Co-Expression Network Analysis (WGCNA)

RNA sequencing was performed on ATDC5 cells treated with sh-NC and sh-BRD4, with five biological replicates per group. A weighted gene co-expression network was constructed using the WGCNA package (v1.73) in R (v4.3.0). Low-expression genes were first filtered using a threshold of CPM > 1. The soft-thresholding power was set to 6 to satisfy the scale-free topology criterion (R^2 > 0.85). Co-expression modules were identified using the dynamic tree cut algorithm with parameters deepSplit = 2 and minModuleSize = 30. Module eigengenes were then correlated with treatment groups. Candidate genes were selected based on module membership (MM > 0.8) and gene significance (GS > 0.6).

Least Absolute Shrinkage and Selection Operator (LASSO) Regression Analysis

Based on the gene expression matrix derived from WGCNA screening, LASSO regression was performed using the glmnet package (v4.1-6) in R (v4.3.0). L1 regularization was applied with the parameter $\alpha = 1$, and the optimal λ value was determined by 10-fold cross-validation using the λ.1se criterion. Feature genes were defined as those with non-zero coefficients following cross-validation.

Gene set enrichment analysis (GSEA)

GSEA was performed using R (v4.2.1) with the clusterProfiler package (v4.4.4). Gene sets were obtained from the MSigDB Collections database (c2.cp.all.v2022.1.Hs.symbols.gmt), which contains 3,050 curated canonical pathway gene sets, and gene set information was retrieved using the msigdbr package (v7.5.1). Prior to analysis, genes identified from differential expression analysis were ranked, and gene identifiers were unified using the org.Mm.eg.db package. GSEA was then conducted with clusterProfiler to calculate the normalized enrichment score (NES) and

multiple-testing–adjusted p values for each gene set. The analysis was performed for mouse (Mus musculus). Statistical significance was defined as a false discovery rate (FDR) q value < 0.25, with key results highlighted at $q < 0.05$.

dBET1 Treatment and BRD4 Degradation Assessment in ATDC5 Cells

To evaluate the effect of dBET1 on BRD4 protein degradation, ATDC5 cells were treated with a gradient of dBET1 concentrations (0.1, 0.5, 1, 5, and 10 μM) for 24 hours. Additionally, cells were treated with 1 μM dBET1 for varying durations (2, 6, 12, and 24 hours) to assess time-dependent effects. dBET1 was purchased from Sellcek (Houston, TX, USA), dissolved in DMSO to prepare a stock solution, and stored at -20 °C. Working concentrations were freshly diluted before use. Following treatment, total protein was extracted using RIPA lysis buffer (Beyotime), quantified via the BCA method, and subjected to Western blot (WB) to determine BRD4 protein expression levels.

Cytotoxicity Evaluation of dBET1

The cytotoxicity of dBET1 in ATDC5 cells was assessed using a CCK-8 assay kit (Beyotime, Shanghai, China). Cells were seeded in 96-well plates at a density of 2×10^4 cells/mL and incubated overnight. Two experimental conditions were applied: (1) cells were directly treated with dBET1 at various concentrations (0.1, 0.5, 1, 5, and 10 μM) for 24 hours without inflammatory stimulation; (2) cells were pretreated with dBET1 at the same concentrations for 2 hours, followed by co-incubation with 1 μg/mL recombinant mouse TNF-α (Peprotech, USA) for an additional 18 hours. To evaluate long-term cytotoxicity, ATDC5 cells and mesenchymal stem cells (MSCs) were treated with 1 μM dBET1 for 1, 3, 5, and 7 days. Subsequently, 10 μL of CCK-8 reagent was added to each well and incubated at 37 °C for 1 hour. Absorbance was recorded at

450 nm, and cell viability was calculated accordingly.

Chondrocyte Isolation and Culture

Articular cartilage was harvested from the tibial plateaus and femoral condyles of male mice aged 3-4 days. Under sterile conditions, the tissue was cut into small fragments (2-5 mm^3) and incubated in DMEM containing 0.2% type II collagenase (17101-015, Gibco, USA) at 37 °C with shaking at 150 rpm for 5 hours. The digested suspension was filtered through a 70 μm cell strainer, centrifuged at 800 × g for 5 minutes, and washed three times with PBS. The resulting cell pellet was resuspended in DMEM supplemented with 10% fetal bovine serum (FBS; 10099-141, Gibco, USA) and penicillin-streptomycin (15140122, Gibco, USA; 10,000 U/mL). Cells were cultured in a 37 °C incubator with 5% CO_2 and passaged upon reaching approximately 80% confluence. Passage 1 (P1) chondrocytes were used for subsequent plasma membrane extraction.

Isolation of Chondrocyte Plasma Membranes

Primary P1 mouse chondrocytes were used for plasma membrane extraction. After washing with PBS, the cells were gently scraped using a cell scraper (Corning, USA) and collected by centrifugation at 800 × g for 5 minutes at 25 °C. The cell pellet was resuspended in 3 mL of ice-cold plasma membrane isolation buffer containing 75 mM sucrose, 225 mM mannitol, 30 mM Tris-HCl (pH 7.4), 0.5% (w/v) bovine serum albumin (BSA; A7030, Sigma-Aldrich, USA), and 0.5 mM EGTA, supplemented with a phosphatase/protease inhibitor cocktail (P1265, Beyotime, China). To achieve complete cell disruption, the suspension was subjected to probe sonication on ice at 30 W (2 s on/3 s off) for 5 minutes. The lysate was centrifuged at 3000 × g for 5 minutes at 4 °C to remove nuclei and intact cells, and the resulting supernatant was collected. This supernatant was then centrifuged at 10,000 × g for 10 minutes at 4 °C to eliminate mitochondria; the pellet was

discarded, and the supernatant retained. Finally, the supernatant was ultracentrifuged at 100,000 × g for 2 hours at 4 °C to isolate the plasma membrane fraction. The membrane pellet was resuspended in 0.2 mM EDTA solution, and the membrane protein concentration was quantified using a BCA protein assay kit (P0012, Beyotime, China). The isolated plasma membrane samples were aliquoted and stored at -80 °C to avoid repeated freeze-thaw cycles. Primary chondrocytes at passage 1 (P1) were selected as the membrane source primarily to ensure batch-to-batch consistency and membrane integrity, thereby preserving a stable adhesion and receptor phenotype and minimizing preparation-related variability. The resulting chondrocyte cell membranes (CCM) retained key membrane proteins and adhesion molecules after isolation, such as receptors, integrins, and glycosaminoglycan-binding sites, providing the structural and functional basis for constructing the subsequent membrane-camouflaged delivery system.

Isolation of Mouse Erythrocyte Plasma Membranes

Fresh whole blood was collected from adult male C57BL/6 mice via retro-orbital venous plexus puncture. The blood samples were centrifuged at 3000 × g for 5 minutes to remove serum and then washed twice with PBS buffer (pH 7.4). The washed erythrocytes were resuspended in hypotonic PBS (0.2× PBS: 20 mM NaCl, 4 mM Na_2HPO_4, 0.8 mM KH_2PO_4) under ice-bath conditions to induce membrane lysis. The lysate was centrifuged at 10,000 × g for 10 minutes at 4 °C to remove free hemoglobin (HGB), and the pellet was collected. The lysis and centrifugation steps were repeated until the supernatant became clear and colorless, indicating complete removal of HGB. The final erythrocyte plasma membrane fraction was resuspended in PBS and stored short-term at 4 °C or aliquoted and preserved long-term at -80 °C to avoid repeated freeze-thaw cycles.

Preparation of CCM-Coated Peptide-Modified Mesoporous Silica Nanoparticles (CCM@PM)

Deionized water (1000 mL) was adjusted to pH ≈ 11 using NH_4OH solution (25-28 wt% $NH_3 \cdot H_2O$). Under vigorous stirring at 50 °C, CTAB (1.12 g) was dissolved, followed by slow dropwise addition of TEOS (52.8 mL). The reaction was stirred for 2 hours and allowed to stand overnight. The precipitate was collected by centrifugation at 5,400 × g for 10 minutes, washed alternately with deionized water and ethanol, and ultrasonically dispersed in ethanol for 30 minutes. The dispersion was mixed with a water:toluene (1:1, v/v) solution (20 mL) and transferred into a PTFE-lined autoclave for hydrothermal treatment at 140 °C for 4 days, yielding mesoporous silica nanoparticles (MSNs). To remove the CTAB template, the MSNs were refluxed in 9 mL HCl/400 mL methanol at 70 °C for 36 hours, washed to neutral pH, and vacuum-dried for 20 hours. Subsequently, 1 g of MSNs was dispersed in 50 mL anhydrous toluene, and 1 mL 3-mercaptopropyltrimethoxysilane (MPTMS) was added under nitrogen protection. The mixture was stirred at 110 °C for 8 hours, centrifuged, washed with ethanol, and collected as thiol-functionalized MSNs (T-M). T-M (10 mg) was dissolved in 2 mL methanol and reacted with 5 mg 2,2'-dipyridyl disulfide at ambient temperature for 12 hours. After washing and drying, pyridine-functionalized MSNs (PyM) were obtained. PyM was then reacted with 2 mg cartilage-targeting peptide (DWRVIIPPRPSA, C-terminal cysteine-modified, synthesized by Chutai Bio) at ambient temperature for 12 hours. Following centrifugation (16,000 × g, 10 minutes) and methanol washing, peptide-modified MSNs (PM) were obtained.

For drug loading, PM (10 mg) was mixed with 2 mg FITC-labeled BRD4-PROTAC in anhydrous ethanol and processed using a negative-pressure drying and rehydration method. Drug encapsulation efficiency was determined using a UV-Vis spectrophotometer (UV-2600, Shimadzu, Japan) at 516 nm based on a standard calibration curve. Finally, mouse P1 CCM and PM

nanoparticles were mixed at a mass ratio of 2:1 and subjected to ultrasonic water bath treatment (37 kHz) for 1 minute at ambient temperature. The mixture was then centrifuged at 16,000 × g for 15 minutes at 4 °C to remove unbound membrane fragments, yielding CCM@PM. PROTACs were loaded via hydrophobic interactions and pore adsorption, representing a physical encapsulation strategy that does not involve covalent bond formation.

Nitrogen Adsorption-Desorption Measurement and Pore Structure Analysis

PepM powder was vacuum-dried at 80 °C for 12 hours and analyzed using a specific surface area analyzer (ASAP 2020, Micromeritics, USA). Nitrogen adsorption–desorption measurements were conducted over the full relative pressure range at 77 K. The specific surface area was calculated using the Brunauer–Emmett–Teller (BET) model within a relative pressure (P/P_0) range of 0.05–0.30. Pore size distribution was determined by fitting the adsorption data using the density functional theory (DFT) method, and pore structure curves were generated accordingly.

dBET1 Elution Assay

To evaluate dBET1 elutability, suspensions of dBET1-loaded PM or CCM@PM were placed in glass beakers containing prewarmed PBS buffer (pH 7.4) at a suspension-to-medium volume ratio of 1:20. Samples were maintained at 37 °C with constant mixing at 150 rpm to ensure uniform dispersion. At predetermined time points, aliquots were collected and centrifuged at 10,000 × g for 10 minutes to separate nanoparticles. The supernatant was collected for drug quantification, and an equal volume of PBS was replenished to maintain a constant total volume. dBET1 concentration was measured using a UV-visible spectrophotometer, and cumulative elution profiles were recorded over time. Low-adsorption centrifuge tubes were used throughout, and all procedures were conducted under constant temperature conditions to minimize external variability.

Characterization of PM and CCM@PM Nanoparticles

The incorporation of functional groups on the nanoparticles was assessed using Fourier-transform infrared spectroscopy (FTIR, Nicolet iS50, Thermo Fisher Scientific, USA) within the 4000-500 cm^{-1} range. Characteristic peaks corresponding to thiol, pyridine groups, cell membrane proteins (e.g., C=O, C-N, S-H), and drug-loading signatures were identified. The particle morphology was examined by transmission electron microscopy (TEM, JEM-2100, JEOL, Japan). For TEM analysis, 10 μL of aqueous dispersion was deposited onto carbon-coated copper grids, air-dried, and imaged without staining. Elemental mapping of N, S, and P was performed using energy-dispersive spectroscopy (EDS) coupled with TEM to evaluate the homogeneity of cell membrane components and organic ligands. Hydrodynamic diameter and zeta potential were measured using a Delsa Nano C particle analyzer (Beckman Coulter, USA) equipped with a 633 nm He-Ne laser (4 mW) at 25 °C, and Delsa Nano software was used to assess size and surface charge variations associated with membrane coating. Ultraviolet-visible (UV-Vis) absorption spectra were acquired using a spectrophotometer (U-2910, Hitachi, Japan) over the 200–800 nm range in a 2 mm quartz cuvette, with the characteristic absorption peak of FITC-labeled BRD4-PROTAC detected at 516 nm. Elemental composition was further analyzed by field-emission scanning electron microscopy (FE-SEM, S-4800, Hitachi, Japan) combined with EDS to confirm membrane-coating element distribution. The encapsulation efficiency of CCM@PM, calculated using a standard calibration curve, remained stable at 82.43 ± 2.16% across three independent experiments, with a drug loading capacity of 7.52%.

***In Vitro* Release Kinetics Assay**

dBET1-loaded PM or CCM@PM nanoparticles were loaded into dialysis bags (molecular

weight cutoff, 3.5 kDa) and immersed in PBS (pH 7.4). Samples were incubated at 37 °C on a horizontal shaker at 100 rpm. At predetermined time points, aliquots of the external medium were collected and replaced with equal volumes of fresh PBS. dBET1 concentration was quantified using a UV-visible spectrophotometer, and cumulative release profiles were recorded over time.

Cellular Targeting and Uptake Analysis

To evaluate the targeting ability and endocytosis efficiency of different nanoparticle platforms in chondrocytes, Cy5.5-labeled unmodified mesoporous silica nanoparticles, red blood cell membrane-coated nanoparticles (RM@PM), and CCM@PM were incubated with primary mouse chondrocytes for 2 hours. For confocal imaging, cells were washed three times with PBS, stained with DAPI (1 μg/mL, D9542, Sigma-Aldrich, USA) for 5 minutes, and imaged using a laser scanning confocal microscope (LSM 710, Zeiss Microsystems, Germany). For flow cytometry analysis, cells were washed with PBS, centrifuged at 400 × g for 3 minutes, and resuspended in FACS buffer (PBS containing 2% FBS and 1 mM EDTA). Data acquisition was performed on a BD Accuri C6 flow cytometer (BD Biosciences, USA) using BD Accuri C6 software (v.1.0.264.21). A minimum of 10,000 events were recorded per sample. Debris and doublets were excluded based on forward scatter (FSC) and side scatter (SSC) properties. The gating strategy used to identify the main cell population and determine Cy5.5 fluorescence intensity is outlined in Supplementary Figure 21. To further assess the selective uptake capacity of CCM@PM in heterologous cell types, the three types of nanoparticles were separately incubated with bone marrow mesenchymal stem cells (BMSCs, CP-M131, Procell, China) and macrophages (RAW264.7, CL-0190, Procell, China). Uptake efficiency in each cell type was evaluated using the same flow cytometry procedure and gating parameters. Final data analysis was conducted using FlowJo software (v10.8, Tree Star, USA).

Endocytic Mechanism of Chondrocyte Uptake for Membrane-Coated Nanoparticles

To investigate endocytic pathways, Cy5.5-labeled PM, RM@PM, and CCM@PM were incubated with primary mouse chondrocytes. Cells were seeded in 20 mm glass-bottom confocal dishes and cultured overnight to approximately 50% confluence, then incubated in serum-free DMEM containing nanoparticles (200 μg/mL) for 4 hours. During the final 30 minutes, Alexa Fluor 488-labeled pathway markers were added: cholera toxin (5 μg/mL, caveolae-mediated, C34775, Invitrogen, USA), transferrin (50 μg/mL, clathrin-mediated, T13342, Invitrogen, USA), and dextran (500 μg/mL, macropinocytosis, D22910, Invitrogen, USA). Cells were fixed with 4% paraformaldehyde (PFA; P0099, Beyotime, China) for 15 minutes, washed with PBS, counterstained with DAPI (1 μg/mL) for 5 minutes, and imaged by confocal microscopy to assess fluorescence colocalization.

For inhibitor-based validation, chondrocytes were seeded in six-well plates at 2×10^5 cells/well and cultured overnight, then pretreated at 37 °C for 30 minutes with Dynasore (40 μM, clathrin-mediated inhibition), Rottlerin (2 μM, macropinocytosis inhibition), Nystatin (54 μM, caveolae-mediated inhibition), or Cytochalasin D (10 μM, phagocytosis inhibition) (all from Sigma-Aldrich, USA). Cells were subsequently incubated with Cy5.5-labeled PM, RM@PM, or CCM@PM (200 μg/mL) for 2 hours. Parallel incubation at 4 °C was performed to assess energy dependence, and cells incubated at 37 °C without inhibitors served as positive controls. After washing with PBS, 1×10^4 cells were collected and analyzed using the BD Accuri C6 (BD Biosciences, USA), with data processed using FlowJo (v10.5, BD Biosciences, USA).

Confocal Imaging of Subcellular Localization of BRD4-PROTAC

Chondrocytes were seeded on glass coverslips or confocal-compatible culture dishes and

incubated with FITC-labeled BRD4-PROTAC after attachment. At designated time points, culture medium was replaced with medium containing antibodies against Rab5 or LAMP1 for immunofluorescence labeling. Cells were washed with PBS, fixed with 4% PFA for 10 minutes, permeabilized with 0.1% Triton X-100, and incubated with appropriate primary and fluorescent secondary antibodies. Nuclei were counterstained with DAPI. Multichannel fluorescence images were acquired using a laser scanning confocal microscope (Leica or Zeiss) and saved for subsequent image analysis.

Scanning Electron Microscopy (SEM) Observation

To examine the adsorption capacity of surface-modified nanoparticles on mouse cartilage tissue, fresh femoral head cartilage was harvested from 8-week-old male C57BL/6J mice and pre-equilibrated for 2 hours in phenol red-free DMEM supplemented with 10% FBS (Gibco, USA) and 1% penicillin-streptomycin (Gibco, USA) at 37 °C in a 5% CO_2 incubator. Cy5.5-labeled PM, RM@PM, and CCM@PM were then added at a final concentration of 200 μg/mL and incubated for an additional 12 hours. After incubation, the cartilage tissues were thoroughly rinsed with PBS and immediately fixed in 2.5% glutaraldehyde for 12 hours. The fixed tissues were cryoprotected with 15% sucrose, followed by graded ethanol dehydration (30%, 50%, 70%, 90%, and 100%), freeze-dried, and sputter-coated with gold. The distribution and surface adsorption of nanoparticles on the cartilage were subsequently observed using an SEM (S-4800, Hitachi, Japan).

Cartilage Tissue Penetration Assay

Fresh femoral head cartilage from 8-week-old male C57BL/6J mice was treated under conditions identical to the SEM experiment. Cartilage samples were incubated with Cy5.5-labeled PM, RM@PM, and CCM@PM at 200 μg/mL for 3 days, washed with PBS, and embedded in

Tissue-Tek O.C.T. compound. Frozen sections (10 μm) were prepared using a cryostat (Leica Biosystems, Germany), stained with DAPI (1 μg/mL) for 5 minutes, washed, and mounted with Fluoromount-G (SouthernBiotech, USA). Penetration depth and fluorescence distribution were examined using a confocal laser scanning microscope.

Intra-articular Retention and *In Vivo* Distribution

An intra-articular injection model was established to evaluate joint retention of nanoparticles. Cy5.5-labeled PM, RM@PM, and CCM@PM were prepared, along with a free Cy5.5 control. Each formulation was prepared at 5 mg/mL (based on total nanoparticle mass), and 50 μL diluted in sterile 0.9% NaCl was injected into the right knee joint cavity. All formulations were injectable in situ gelling systems. Specifically, Rh-Gel@CCM@PM remained in a flowable sol state at ambient temperature and was injected through a 27 G needle, rapidly forming a gel in response to the local microenvironment without implantation of a preformed hydrogel. On days 1, 10, 28, and 35 post-injection, fluorescence signals from the joint region were captured using an *in vivo* imaging system (IVIS Spectrum, PerkinElmer, USA). The region of interest (ROI) was defined as the knee joint area. Image analysis was conducted using Living Image software (v4.5, PerkinElmer, USA), with excitation/emission wavelengths set to 675/720 nm for Cy5.5. In addition, at days 1 and 10 post-injection, major organs, including the heart, spleen, liver, lungs, and kidneys, were harvested to assess the biodistribution and tissue accumulation of fluorescence signals.

Preparation and Characterization of Hydrogel

The rhein-based hydrogel (Rh-Gel) was formed through the self-assembly of the herbal compound rhein (Rh, R726100, Aladdin, China). Rh was dissolved in 0.1 M $NaHCO_3$ buffer (pH 8.3) at 4 mg/mL, heated to 60 °C until fully dissolved, and slowly cooled to ambient

temperature to form a uniform red, transparent gel. Rh-Gel was stored at 4 °C in the dark until use. UV-Vis absorption spectra were recorded from 200–800 nm using a spectrophotometer (UV-2600, Shimadzu, Japan), with characteristic peaks at 260 nm and 435 nm. Fluorescence spectra were acquired using a fluorescence spectrophotometer (F-7000, Hitachi, Japan) at an excitation wavelength of 435 nm and an emission range of 500–700 nm, with an emission peak at 592 nm.

Zeta potential was measured at 25 °C using a Zetasizer Nano ZS90 (Malvern Instruments, UK), with triplicate measurements averaged. Lyophilized Rh-Gel samples were sputter-coated with gold and examined by FE-SEM (SU8020, Hitachi, Japan) at 5 kV to visualize the three-dimensional nanofiber microstructure.

Construction and Characterization of Rhein-Based Hydrogel Loaded with Chondrocyte Cell Membrane-Coated Peptide-Modified Mesoporous Silica Nanoparticles (Rh-Gel@CCM@PM)

Rh-Gel precursor sol was prepared as above and maintained in a flowable state. CCM@PM dispersion was added to achieve a final nanoparticle concentration of 20 mg/mL, yielding an injectable Rh-Gel@CCM@PM composite sol with an embedded CCM@PM content of 2 mg/mL gel. For *in vitro* characterization, the sol was injected into molds (~5 mm diameter) and allowed to gel for 30–60 minutes. PBS (pH 7.4) was then added, and samples were equilibrated for 1 h to obtain composite hydrogels.

UV-Vis spectra were collected over 300–700 nm (1 nm step size) in a 1 cm quartz cuvette using the UV-2600, with absorption peaks at 554 nm for Rh and 495 nm for FITC-labeled CCM@PM. Zeta potential was measured at 25 °C using the Zetasizer Nano ZS90 (Malvern Instruments, UK), with results expressed as mean ± SD. Confocal laser scanning microscopy was used to visualize nanoparticle distribution within the hydrogel using a 40× water-immersion

objective, with excitation at 488 nm for FITC and 561 nm for Rh. Z-stack imaging was performed at 1 μm step size to assess spatial localization within hydrogel pores.

Rheological Characterization

Rheological measurements of Rh-Gel@CCM@PM hydrogels were performed using a parallel-plate rheometer (MCR 302, Anton Paar, Austria). Freshly prepared hydrogels were equilibrated at ambient temperature for 30 min and loaded onto a 25 mm parallel-plate geometry with a 1.0 mm gap. Excess material was trimmed to ensure uniform stress distribution. All measurements were conducted at 25°C under solvent trap protection to prevent dehydration. Amplitude sweep tests were performed in oscillatory mode over a strain range of 0.01%-500% at a fixed frequency of 1 Hz to obtain strain-dependent storage modulus (G′) and loss modulus (G″). Cyclic shear tests were conducted by alternately applying 1% and 300% strain with a cycle duration of 30 seconds. Frequency sweep measurements were carried out within the linear viscoelastic region at 1% strain over a frequency range of 0.1-100 Hz. Time sweep tests were performed at a constant strain of 1% and frequency of 1 Hz for 10-30 minutes. Viscosity-shear rate profiles were obtained under steady-state flow by increasing the shear rate from 0.1 to 1000 s^{-1}. All data were collected and exported using RheoCompass for subsequent analysis.

Hydrogel Storage Stability and Injectability Assessment

Freshly prepared brown hydrogels were sealed in nitrogen-filled centrifuge tubes and stored at 4°C for 0, 1, 2, 4, and 8 weeks. At each time point, samples were photographed to document macroscopic appearance under identical conditions. Hydrogels were then loaded into 1 mL syringes fitted with 27 G needles for injectability testing. Injection was performed under consistent applied pressure and experimental conditions, and extrusion behavior, including flow continuity

and shape retention, was recorded in real time. Hydrogels stored for 0, 1, 2, 4, and 8 weeks were further subjected to shear rheological testing to evaluate shear-thinning behavior. Viscosity-shear rate curves were generated, with each storage time point measured in triplicate to ensure reproducibility.

pH-Responsive Drug Release Assay

To evaluate the pH-responsive release behavior of Rh-Gel@CCM@PM, hydrogel samples (4 mg/mL) were sealed in dialysis bags (molecular weight cut-off, 3.5 kDa; Solarbio, China) and immersed in 100 mL PBS buffer at pH 7.4 or pH 5.5, simulating the physiological joint environment and the mildly acidic inflammatory microenvironment, respectively. The dialysis systems were incubated at 37 °C on a shaker at 60 rpm. At predetermined time points (0.5, 1, 2, 3, 4, 5, 6, and 7 days), 10 mL of release medium was collected and replaced with an equal volume of fresh PBS to maintain a constant system volume. The absorbance of the collected samples was measured at 452 nm using a UV spectrophotometer (UV-2600, Shimadzu, Japan), and the cumulative release percentage was calculated to generate the drug release profile. To monitor the release of FITC-labeled CCM@PM nanoparticles, fluorescence intensity of the collected medium was measured using a fluorescence spectrophotometer (F-7000, Hitachi, Japan) with excitation at 488 nm and emission at 516 nm. Samples collected at each time point were examined by TEM (JEM-2100, JEOL, Japan) to evaluate particle size and structural integrity of CCM@PM nanoparticles.

ATDC5 Cell Culture and Experimental Grouping

ATDC5 mouse chondrogenic progenitor cells were obtained from Wuhan Procell Life Science & Technology Co., Ltd. (CL-0856, Procell, China). Human articular chondrocytes (HAC) and

mouse synovial cells (MSC) were purchased from the same supplier (CP-H096 and CP-M083, respectively). ATDC5 cells were cultured as adherent monolayers in DMEM/F12 medium (11320-033, Gibco, USA) supplemented with 10% FBS (10099-141, Gibco, USA) and 1% penicillin-streptomycin (15140122, Gibco, USA), and maintained in a humidified incubator at 37 °C with 5% CO_2. The culture medium was refreshed every 2-3 days. HACs were cultured in human articular chondrocyte complete medium (CM-H096, Procell, China) with medium changes every 3-4 days, while MSCs were maintained in mouse synovial cell complete medium (CM-M083, Procell, China) with medium replaced every 2-3 days. Cells within two passages were used for all experiments [40].

When ATDC5 cells reached approximately 70% confluence, they were randomly assigned to the following groups: Ctrl group (untreated control); TNF-α group (10 ng/mL recombinant mouse TNF-α, 315-01A, PeproTech, USA, 24 hours); TNF-α + sh-NC group (sh-NC lentiviral transduction followed by TNF-α treatment); TNF-α + sh-BRD4 group (sh-BRD4 lentiviral transduction followed by TNF-α treatment); sh-NC group; sh-BRD4 group; OD1 group (Nav1.7 agonist OD1, 100 nM; 5941, Tocris Bioscience, USA, 4 hours); and sh-BRD4 + OD1 group (sh-BRD4 transduction followed by OD1 treatment). For patch-clamp electrophysiology, two additional groups were included: TTX group (TTX, 1 μM, Tocris Bioscience, UK, 48 hours following TNF-α priming at 10 ng/mL for 24 hours) and ProTx II group (Nav1.7-specific blocker ProTx II, 25 nM; HY-P1221, MedChemExpress, China, 48 hours following TNF-α priming) [41, 42]. When HACs reached approximately 70% confluence, they were randomly assigned to a TNF-α group (10 ng/mL recombinant human TNF-α, SRP3177, Sigma-Aldrich, USA, 24 hours), an Rh-Gel group, a CCM@PM group, and an Rh-Gel@CCM@PM group.

shRNA Transfection Assay

To achieve stable BRD4 knockdown in ATDC5 cells, two BRD4-specific short hairpin RNA

sequences (sh-BRD4) as well as a non-targeting sequence (a negative control [sh-NC]) were designed and synthesized (Supplementary Table 2).

All sequences were subcloned into the lentiviral vector GV493 (U6-MCS-Ubiquitin-EGFP-IRES-puromycin, GeneChem). Lentiviruses were produced in HEK293T cells (CL-0005, Procell, China), yielding a viral titer of 2×10^8 TU/mL. The viral supernatant was purified by ultrafiltration for subsequent infection. ATDC5 cells were seeded in six-well plates at 2×10^5 cells/well and cultured to 40-50% confluence. For transduction, 500 μL of transfection mixture containing lentivirus (MOI = 50), 5 μg/mL PolyJet (SL100688, SignaGen, USA), and 1 μg/mL Polybrene (TR-1003, Sigma-Aldrich, USA) was added to each well and incubated for 6 hours. Subsequently, 1 mL of complete medium was added. At 48 hours post-infection, cells were selected with 2 μg/mL puromycin (A1113803, Gibco, USA) for 72 hours to establish stable cell lines. Infection efficiency was evaluated by GFP fluorescence using a fluorescence microscope (Leica DMi8, Leica Microsystems, Germany), and only cultures with ≥80% GFP positivity were used for subsequent experiments. On day 5 post-infection, cells were harvested for total RNA and protein extraction. BRD4 knockdown efficiency was evaluated by RT-qPCR and WB analysis.

Membrane and Cytoplasmic Protein Isolation

Membrane and cytoplasmic proteins were isolated using a membrane protein extraction kit (P0033, Beyotime, China). The separated fractions were subjected to WB analysis to assess Nav1.7 expression in the membrane compartment.

Whole-Cell Patch-Clamp Recording of Sodium Currents

Whole-cell patch-clamp recordings were performed at ambient temperature using the Axon Patch-Clamp 700B system (Molecular Devices, USA). The extracellular solution contained

140 mM NaCl, 3 mM KCl, 1 mM $MgCl_2$, 1 mM $CaCl_2$, 10 mM HEPES, 5 mM CsCl, and 20 mM tetraethylammonium chloride (TEA-Cl), adjusted to pH 7.3 with CsOH. The pipette (intracellular) solution consisted of 110 mM CsF, 25 mM NaCl, 1 mM $CaCl_2$, 10 mM EGTA, 20 mM TEA, 10 mM glucose, and 10 mM HEPES, also adjusted to pH 7.3 with CsOH. Patch pipettes had a resistance of 3-5 MΩ. Recordings were conducted with a holding potential of -60 mV. A series of depolarizing voltage steps from -60 mV to +50 mV, in 10 mV increments and each lasting 50 ms, was applied to evoke inward sodium currents. Electrical signals were amplified using an Axopatch 200B amplifier and digitized via a Digidata 1322A interface at a sampling rate of 5-10 kHz. Data were acquired using pCLAMP 9.2 software and analyzed with Clampfit 9.2 (Molecular Devices, USA). Nav1.7 channel functionality was verified by repeating the recording protocol following treatment with either 1 μM TTX (Tocris Bioscience, UK) or 25 nM ProTx II (HY-P1221, MCE, China).

Detection of Intracellular ROS Levels Using DCFH-DA Probe

ATDC5 cells were seeded in six-well plates and, after designated treatments, washed twice with PBS. Cells were incubated with 10 μM DCFH-DA probe (50101ES01, YEASEN, China) for 30 min at 37 °C in the dark, washed three times with PBS, and counterstained with DAPI (1 μg/mL, D9542, Sigma-Aldrich, USA) for 5 minutes. Coverslips were mounted after a final PBS rinse. Green fluorescence was imaged using a laser scanning confocal microscope (TCS SP8, Leica Microsystems, Germany) with excitation/emission wavelengths of 488 nm/500-530 nm for DCFH-DA and 405 nm/420-480 nm for DAPI. Intracellular ROS levels were quantified using ImageJ (v1.53c, NIH, USA) based on fluorescence intensity.

TEM for Mitochondrial Morphology

Following treatment, cells were collected and immediately fixed in 2.5% glutaraldehyde solution (P1126, Solarbio, China) at 4 °C for 12 h. Post-fixation was carried out using 1% osmium tetroxide (P1125, Solarbio, China) for 2 h, followed by PBS washing. Samples were dehydrated through a graded ethanol series (30%, 50%, 70%, 90%, and 100%) and embedded in epoxy resin. Ultrathin sections (~70 nm) were obtained using an ultramicrotome and stained with uranyl acetate and lead citrate. Mitochondrial morphology and cristae structure were examined using a TEM at an accelerating voltage of 80 kV, and representative images were captured for further analysis.

JC-1 Dye Detection of Mitochondrial Membrane Potential (ΔΨm)

Following treatment, cells were incubated with JC-1 working solution (C2006, Beyotime, China) for 20 minutes at 37 °C in the dark, then washed three times with PBS. Red fluorescence (JC-1 aggregates, high membrane potential) and green fluorescence (JC-1 monomers, low membrane potential) were imaged using an inverted fluorescence microscope (DMi8, Leica Microsystems, Germany). The red-to-green fluorescence intensity ratio (Aggregate/Monomer, A/M ratio) was calculated using ImageJ to evaluate changes in ΔΨm.

ATP Content Measurement

Following treatment, ATP levels were quantified using an ATP assay kit (S0026, Beyotime, China). Cell lysates were mixed with the ATP detection reagent, and luminescence intensity (RLU) was measured using a Luminoskan Ascent microplate luminometer (Thermo Fisher Scientific, USA). ATP standard solutions (1-10 μmol/L) were used to generate a standard curve, and ATP concentrations were calculated accordingly. Results were expressed as ATP content (μmol/L) to evaluate cellular energy metabolism.

ChIP-qPCR Detection of Histone H3 Acetylation (H3ac) Modification at the Scn9a Promoter

Chromatin immunoprecipitation was performed using the ChIP Assay Kit (17-295, Millipore, USA). ATDC5 cells were crosslinked with 1% formaldehyde for 10 minutes, quenched with 125 mM glycine, lysed, and sonicated to 200-600 bp fragments using a Bioruptor Plus (Diagenode, Belgium). Equal amounts of chromatin were incubated overnight at 4 °C with magnetic Protein A/G beads pre-coated with either an anti-H3ac antibody (06-599, Millipore, USA, 1:100) or rabbit IgG isotype control (ab172730, Abcam, UK, 1:100). Following elution and proteinase K digestion, DNA was purified and subjected to qPCR targeting the promoter region of Scn9a (Nav1.7). Relative enrichment was quantified using the $2^{-\Delta Ct}$ method, with the IgG group serving as the negative control.

Dual-Luciferase Reporter Assay for Scn9a Promoter Activity

The mouse Scn9a promoter was cloned into the pGL3-Basic vector (E1751, Promega, USA). ATDC5 cells were co-transfected with pGL3-Scn9a (500 ng/well) and Renilla luciferase control pGM-T (50 ng/well, Invitrogen, USA) using Lipofectamine 2000 (11668500, Invitrogen, USA). After 24 h of transfection, cells were treated with TNF-α and cultured for an additional 24 h. Luciferase activity was measured using the Dual-Luciferase® Reporter Assay System (E1910, Promega, USA) on a GloMax luminometer (Promega, USA). Promoter activity was calculated as the Firefly to Renilla luciferase ratio and expressed as a fold change relative to the NC group.

Establishment and Grouping of Animal Models

Eight-week-old male C57BL/6J mice (20-22 g; Slaccas, Shanghai, China) were housed under SPF conditions (22 ± 2 °C, 50 ± 10% humidity, 12-h light/dark cycle). Chondrocyte-specific Nav1.7 knockout mice ($Nav1.7^{chondrocyte}$) and their littermate controls ($Nav1.7^{flox}$) were generated

by crossing Agc1-creERT2 mice (Jackson, 019148) with Scn9a flox mice (S-CKO-04938, Cyagen, China). At 10 weeks, CreERT2 was induced by intraperitoneal tamoxifen (150 mg/kg; T5648, Sigma-Aldrich, USA) in sunflower oil (S5007, Sigma-Aldrich, USA) once daily for five days. Littermate controls were used throughout.

DMM Model: Mice were anesthetized with sodium pentobarbital (50 mg/kg, i.p.). The right knee underwent medial parapatellar incision and transection of the medial meniscotibial ligament; Sham mice received capsule incision only. Animals were randomized into Sham, DMM, Rh-Gel, CCM@PM, and Rh-Gel@CCM@PM groups. Intra-articular injections (10 μL PBS or treatment) were administered weekly for eight weeks. CCM@PM was dosed at 2.0 mg/mL (20 μg per joint). For Rh-Gel@CCM@PM, CCM@PM was embedded at 2 mg/mL gel, delivering an equivalent 20 μg per joint. Behavioral testing followed the final injection, and knees were harvested for analysis.

Monosodium Iodoacetate (MIA) Model: Anesthesia was performed as described above. On day 3, 10 μL of MIA (2 mg/mL, 12513, Sigma-Aldrich, USA) was injected intra-articularly into the knee joint to establish the model. Mice were randomly assigned to five groups (n = 6 per group): Sham, MIA, Rh-Gel, CCM@PM, and Rh-Gel@CCM@PM. Animals received weekly intra-articular injections of 10 μL PBS or the designated treatment for four consecutive weeks. Doses were standardized across groups: CCM@PM was administered at a final concentration of 2.0 mg/mL, corresponding to 20 μg CCM@PM per joint. For the Rh-Gel@CCM@PM group, CCM@PM was embedded in Rh-Gel at 2 mg/mL gel, and injection of 10 μL delivered an equivalent 20 μg CCM@PM per joint. Behavioral assessments were conducted in week 5, followed by knee joint harvesting for analysis [40].

Behavioral Testing

All behavioral assessments were conducted under blinded conditions between 12:00 and 17:00.

In the DMM model, mice underwent three baseline measurements before surgery, followed by weekly testing starting from week 8 post-operation. In the MIA model, behavioral assessments were performed on days 0, 2, 4, 8, 14, 20, and 28 post-injection. Mechanical sensitivity was evaluated using the von Frey test with standard von Frey filaments (Stoelting, USA). Mice were individually placed in transparent Plexiglass chambers on a metal mesh floor and acclimated for 30 minutes. Filaments of increasing force were applied to the plantar surface of the hind paw. Each filament was applied 10 times with a 30-second interval between stimulations. A brisk paw withdrawal was considered a positive response, and the mechanical threshold was defined as the lowest force eliciting at least five positive responses out of ten applications. Open field behavior was assessed using a video tracking system (Smart 3.0, Panlab Harvard Apparatus, Spain). Each mouse was placed in the center of a 45 cm × 45 cm transparent arena and allowed to explore freely for 2 minutes. Locomotor trajectories and total distance traveled were recorded under standard room lighting conditions.

Micro-CT Analysis

After anesthesia, hind limbs were immobilized and scanned using a micro-CT system (Skyscan 1275, Bruker, Germany) at 40 kV tube voltage, 55 μA current, and 10 μm spatial resolution. Three-dimensional reconstruction was performed using Bruker software. Subchondral bone parameters, including bone volume fraction (BV/TV), bone mineral density (BMD), and trabecular thickness (Tb.Th), were quantitatively analyzed.

Histological Staining and Evaluation

Mouse knee joints were fixed in 4% PFA for 24 hours and decalcified in 10% EDTA (pH 7.4) for two weeks. Samples were embedded in paraffin, and serial sections (5 μm) were prepared for

hematoxylin and eosin (H&E) staining (G1120, Solarbio, China) and Safranin O/Fast Green (SO/FG) staining (G1371, Solarbio, China). Cartilage morphology was examined under a light microscope (Zeiss) and blindly scored according to the OARSI grading system (0-6). Glycosaminoglycan (GAG) content and articular cartilage thickness were also quantified.

RT-qPCR

Total RNA was extracted from cell or tissue samples using TRIzol reagent (15596018, Invitrogen, USA). One microgram of RNA was reverse transcribed into cDNA using the Hifair II 1st Strand cDNA Synthesis Kit (Yeasen Biotech Co., Ltd., China). Quantitative PCR was performed with the TB Green Fast qPCR Mix Kit (Takara Biomedical Technology Co., Ltd., China) on a QuantStudio 5 real-time PCR system (Thermo Fisher Scientific, USA). The thermal cycling conditions were as follows: initial denaturation at 95°C for 30 seconds, followed by 40 cycles of 95°C for 5 seconds and 60°C for 30 seconds. Relative mRNA expression levels of target genes were calculated using the ΔΔCt method, with β-actin as the internal control. Primer sequences used for qPCR analysis are listed in Supplementary Table 3.

WB Analysis

Samples included CCM@PM and Rh-Gel@CCM@PM nanoparticles, ATDC5 cells, and cartilage tissue. CCM@PM-related samples were lysed in RIPA buffer with protease inhibitors (P0013B, Beyotime, China). ATDC5 cells and cartilage tissues were homogenized and lysed in standard RIPA buffer. All lysates were sonicated on ice and centrifuged at 12,000 × g for 15 minutes at 4°C. Supernatants were collected, and protein concentrations were determined using a BCA Protein Assay Kit (23225, Thermo Fisher Scientific, USA), then standardized to 2 mg/mL. Proteins (30 μg per sample) were separated by 10% SDS-PAGE and transferred to 0.22 μm PVDF

membranes (IPVH00010, Millipore, USA). Membranes were blocked at ambient temperature for 1 hour in TBST containing 5% BSA or non-fat milk. After blocking, membranes were incubated overnight at 4°C with the following primary antibodies: CD44 (Rabbit monoclonal, ab189524, Abcam, UK, 1:1000), Integrin β1 (Rabbit monoclonal, ab179471, Abcam, UK, 1:2000), N-cadherin (Rabbit polyclonal, ab98952, Abcam, UK, 1:1000), TFAM (Rabbit monoclonal, ab307302, Abcam, UK, 1:1000), ATPB (Rabbit polyclonal, 17247-1-AP, Proteintech, China, 1:1000), BRD4 (Rabbit monoclonal, ab128874, Abcam, UK, 1:1000), Nav1.7 (Rabbit polyclonal, ab65167, Abcam, UK, 1:1000), IL-6 (Rabbit monoclonal, ab290735, Abcam, UK, 1:1000), SOX9 (Rabbit monoclonal, ab185966, Abcam, UK, 1:1000), COL II (Rabbit polyclonal, ab188570, Abcam, UK, 1:1000), MMP13 (Rabbit polyclonal, ab39012, Abcam, UK, 1:3000), and β-actin (Rabbit monoclonal, ab8226, Abcam, UK, 1:2000). After washing with TBST, membranes were incubated at ambient temperature for 1 hour with HRP-conjugated secondary antibodies, including Goat Anti-Rabbit IgG (A0208, Beyotime, China, 1:5000), Goat Anti-Rabbit IgG H&L (HRP) (ab6721, Abcam, UK, 1:5000), or HRP-conjugated antibodies (111-035-144/115-035-146, Jackson ImmunoResearch, USA, 1:8000). Signal detection was carried out using ECL chemiluminescence reagents (P0018, Beyotime, China; WBKLS0500, Millipore, USA; PE0010, Solarbio, China), and images were captured using imaging systems (Tanon 5200, Tanon, China; ChemiDoc XRS+, Bio-Rad, USA; Science Lab 2003, Fuji, Japan). Densitometric analysis of protein bands was conducted with ImageJ software, and results were averaged from three independent experiments for statistical evaluation.

Immunohistochemical Staining

Immunohistochemical staining was performed on paraffin-embedded mouse knee joint sections to evaluate metabolism-related protein expression. Sections were deparaffinized in xylene

and rehydrated through graded ethanol (100%, 95%, 80%). Antigen retrieval was conducted in sodium citrate buffer (pH 6.0, C9999, Sigma-Aldrich, USA) at 95°C for 20 minutes. After cooling, nonspecific binding was blocked with 5% BSA (A2153, Sigma-Aldrich, USA) for 30 minutes. Primary antibodies were applied and incubated overnight at 4°C. The antibodies used included anti-Col2 (Rabbit polyclonal, 1:200, ab34712, Abcam, UK), anti-Mmp13 (Rabbit polyclonal, 1:200, ab39012, Abcam, UK), anti-Aggrecan (Rabbit polyclonal, 1:200, 13880-1-AP, Proteintech, China), and anti-COMP fragment (Mouse monoclonal, 1:200, affinity-purified monoclonal). The following day, sections were washed with PBS and incubated with HRP-conjugated secondary antibody (1:500, A0216, Beyotime, China) at ambient temperature for 1 hour. Color development was performed using a DAB Substrate Kit (ZLI-9019, ZSGB-BIO, China), followed by hematoxylin counterstaining for nuclei. Sections were examined using a light microscope (BX53, Olympus, Japan). Positive staining was semi-quantified using ImageJ (Version 1.51k, Rawak Software, Germany).

Immunofluorescence Staining

Cells were seeded on glass coverslips in 24-well plates, while tissue sections underwent standard deparaffinization and rehydration. Cells were fixed with 4% PFA for 15 minutes and permeabilized with 0.1% Triton X-100 (T8787, Sigma-Aldrich, USA) for 10 minutes following PBS washing. Tissue sections were incubated with 0.1% trypsin at 37°C for 30 minutes, then treated sequentially with 0.25 U/mL chondroitinase ABC (C3667, Sigma-Aldrich, USA) and 1 U/mL hyaluronidase (H3560, Sigma-Aldrich, USA) for 60 minutes. After blocking with 1% BSA for 30 minutes, samples were incubated overnight at 4°C with the following primary antibodies: rabbit anti-N-Cadherin (Rabbit monoclonal, 1:50, ab321897, Abcam, UK), rabbit anti-E-Cadherin (Rabbit monoclonal, 1:50, ab314063, Abcam, UK), rabbit anti-Integrin αV (Rabbit monoclonal,

1:50, ab150361, Abcam, UK), rabbit anti-Integrin β1 (Rabbit monoclonal, 1:50, ab183666, Abcam, UK), rabbit anti-Integrin α3 (Rabbit monoclonal, 1:50, ab131055, Abcam, UK), rabbit anti-CD44 (Rabbit monoclonal, 1:100, ab243894, Abcam, UK), rabbit anti-IL-6 (Rabbit monoclonal, 1:50, ab290735, Abcam, UK), rabbit anti-SOX9 (Rabbit monoclonal, 1:50, ab185966, Abcam, UK), rabbit anti-COL II (Rabbit polyclonal, 1:50, ab34712, Abcam, UK), rabbit anti-MMP13 (Rabbit polyclonal, 1:100, ab39012, Abcam, UK), rabbit anti-ATPB (Rabbit polyclonal, 1:300, 17247-1-AP, Proteintech, China), rabbit anti-TFAM (Rabbit monoclonal, 1:100, ab307302, Abcam, UK), rabbit anti-Nav1.7 (Rabbit polyclonal, 1:50, ASC-027, Alomone Labs, USA), rabbit anti-BRD4 (Rabbit monoclonal, 1:200, ab128874, Abcam, UK), and rabbit anti-ACAN (Rabbit polyclonal, 1:200, 13880-1-AP, Proteintech, China). The following day, samples were washed with PBS and incubated for 1 hour at ambient temperature with either Goat Anti-Rabbit IgG H&L (Alexa Fluor® 488) (ab150077) or Goat Anti-Mouse IgG H&L (Alexa Fluor® 647) (ab150115). Nuclei were counterstained with DAPI. Imaging was conducted using a laser scanning confocal microscope.

Statistical Analysis and Sample Size Determination

No statistical methods were used to predetermine sample size. Sample sizes were determined based on previous experience with similar experimental models and standard practices in the field of osteoarthritis research [43, 44]. Specifically, for *in vivo* studies, a sample size of n = 6 mice per group was chosen to account for biological variability in surgical outcomes and disease progression, providing sufficient power to detect significant differences in histological scores and behavioral parameters.

All data were obtained from at least three independent experiments and are presented as Mean ± SD. Comparisons between two groups were performed using an independent-samples t-test, while comparisons among three or more groups were conducted using one-way analysis of

variance (ANOVA). All statistical analyses were carried out using GraphPad Prism 9.5.0 (GraphPad Software, Inc.) and R 4.2.1 (R Foundation for Statistical Computing). A two-tailed *p*-value < 0.05 was considered statistically significant, whereas $p > 0.05$ was regarded as not significant.

Blinding and Randomization

For *in vivo* studies, animals were randomly assigned to treatment groups. Investigators performing the surgeries, intra-articular injections, and behavioral assessments were blinded to group allocation.

For histological and micro-CT analyses, samples were assigned random identification numbers to ensure blinded evaluation during data acquisition and quantification.

For *in vitro* molecular biology experiments (e.g., RT-qPCR, Western blot), blinding was not performed during sample processing due to the requirement for specific labeling of treatment conditions; however, data analysis was conducted using automated software (e.g., ImageJ, QuantStudio) to minimize operator bias.

Data Availability

The bulk RNA sequencing and single-cell RNA sequencing data generated in this study have been deposited in the NCBI Sequence Read Archive (SRA) under the BioProject accession number PRJNA1400711.

Bulk RNA-seq data are available under the following SRA accession numbers:

Control group: SRR36764747, SRR36764746, SRR36764741, SRR36764740, SRR36764739, SRR36764738;

Case group: SRR36764737, SRR36764736, SRR36764735, SRR36764734, SRR36764745, SRR36764744.

Single-cell RNA-seq data are available under the following SRA accession numbers:

Control group: SRR36764743;

Case group: SRR36764742.

All other data supporting the findings of this study are available within the Article, Supplementary Information, or Source Data files. Source Data are provided with this paper.

References

1. Leszczyński, P. *et al.* Clinical expert statement on osteoarthritis: diagnosis and therapeutic choices. *Rheumatology* (2025) doi:10.5114/reum/199980.

2. Chow, Y. Y. & Chin, K.-Y. The Role of Inflammation in the Pathogenesis of Osteoarthritis. *Mediators of Inflammation* vol. 2020 1–19 (2020).

3. Chen, H., Liu, S., Xing, J., Wen, Y. & Chen, L. Orientin alleviates chondrocyte senescence and osteoarthritis by inhibiting PI3K/AKT pathway. *Bone & Joint Research* vol. 14 245–258 (2025).

4. Lisco, G., Jo, H. G. & Colaianni, G. Editorial: Metabolic disorders as risk factors for

osteoarthritis and targeted therapies for this pathology. *Frontiers in Endocrinology* vol. 15 (2025).

5. Steinmetz, J. D. *et al.* Global, regional, and national burden of osteoarthritis, 1990–2020 and projections to 2050: a systematic analysis for the Global Burden of Disease Study 2021. *The Lancet Rheumatology* vol. 5 e508–e522 (2023).

6. Cho, Y. *et al.* Disease-modifying therapeutic strategies in osteoarthritis: current status and future directions. *Experimental & Molecular Medicine* vol. 53 1689–1696 (2021).

7. McClurg, O., Tinson, R. & Troeberg, L. Targeting Cartilage Degradation in Osteoarthritis. *Pharmaceuticals* vol. 14 126 (2021).

8. Xu, Y.-D. *et al.* Apoptotic body-inspired nanotherapeutics efficiently attenuate osteoarthritis by targeting BRD4-regulated synovial macrophage polarization. *Biomaterials* vol. 306 122483 (2024).

9. Sun, J. *et al.* Inhibition of Brd4 alleviates osteoarthritis pain via suppression of neuroinflammation and activation of Nrf2-mediated antioxidant signalling. *British Journal of Pharmacology* vol. 180 3194–3214 (2023).

10. Jiang, Y. *et al.* BRD4 has dual effects on the HMGB1 and NF-κB signalling pathways and is a potential therapeutic target for osteoarthritis. *Biochimica et Biophysica Acta (BBA) - Molecular Basis of Disease* vol. 1863 3001–3015 (2017).

11. Lee, H. *et al.* Novel molecule BBC0901 inhibits BRD4 and acts as a catabolic regulator in the pathogenesis of osteoarthritis. *Biomedicine & Pharmacotherapy* vol. 166 115426 (2023).

12. Zhou, D., Tian, J.-M., Li, Z. & Huang, J. Cbx4 SUMOylates BRD4 to regulate the expression of inflammatory cytokines in post-traumatic osteoarthritis. *Experimental & Molecular Medicine* vol. 56 2184–2201 (2024).

13. Huang, Z. *et al.* BRD4 inhibition alleviates mechanical stress-induced TMJ OA-like pathological changes and attenuates TREM1-mediated inflammatory response. *Clinical*

Epigenetics vol. 13 (2021).

14. Fu, W. *et al.* Nav1.7 as a chondrocyte regulator and therapeutic target for osteoarthritis. *Nature* vol. 625 557–565 (2024).

15. Zhou, R., Fu, W., Vasylyev, D., Waxman, S. G. & Liu, C. Ion channels in osteoarthritis: emerging roles and potential targets. *Nature Reviews Rheumatology* vol. 20 545–564 (2024).

16. Wang, X. & Li, X. Regulation of pain neurotransmitters and chondrocytes metabolism mediated by voltage-gated ion channels: A narrative review. *Heliyon* vol. 9 e17989 (2023).

17. Wang, Q. *et al.* A ROS-responsive hydrogel encapsulated with matrix metalloproteinase-13 siRNA nanocarriers to attenuate osteoarthritis progression. *Journal of Nanobiotechnology* vol. 23 (2025).

18. Li, J., Chen, X., Lu, A. & Liang, C. Targeted protein degradation in cancers: Orthodox PROTACs and beyond. *The Innovation* vol. 4 100413 (2023).

19. Xi, M. *et al.* Small molecule PROTACs in targeted therapy: An emerging strategy to induce protein degradation. *European Journal of Medicinal Chemistry* vol. 174 159–180 (2019).

20. Xu, J. *et al.* A platinated prodrug leveraging PROTAC technology for targeted protein degradation and enhanced antitumor efficacy. *Inorganic Chemistry Frontiers* vol. 12 3981–3987 (2025).

21. Catlett, J. L. *et al.* Abstract 3758: Discovery of a bridged proteolysis targeting chimera (PROTAC) recruiting the SPOP E3 ubiquitin ligase for targeted protein degradation. *Cancer Research* vol. 85 3758–3758 (2025).

22. Li, Z. Highly Efficient and Long-acting Split-and-Mix Proteolysis Targeting Chimera Based on Self-assembled Polylactic acid. (2025) doi:10.21203/rs.3.rs-5971994/v1.

23. Weng, Z. *et al.* Emerging Strategies in Smart Nano-PROTAC for Stimuli-Responsive Protein Degradation and Precision Cancer Therapy. *Nano Biomedicine and Engineering* vol. 17 315–332

(2025).

24. Laul, E. Therapeutic Potential of Bromodomain Targeting – Development of Anti-Inflammatory Bromodomain Inhibitors & Tumour Targeting SelecPROTACs. doi:10.5167/uzh-270782.

25. Xie, S. *et al.* Versatile Copper-Chalcogenide-Based Nanoparticles for the Treatment of Brain Diseases. *Nano Biomedicine and Engineering* vol. 17 91–110 (2025).

26. Zhu, H., Fan, J., Yang, C., Liu, J. & Ding, B. DNA Nanocarriers for Delivery of sgRNA/Cas9 Ribonucleoprotein. *Nano Biomedicine and Engineering* vol. 16 331–344 (2024).

27. Liu, Y. *et al.* Single-cell transcriptomics reveals novel chondrocyte and osteoblast subtypes and their role in knee osteoarthritis pathogenesis. *Signal Transduction and Targeted Therapy* vol. 10 (2025).

28. Rai, M. F. Nip it in the bud: potential for the early treatment of osteoarthritis. *Osteoarthritis and Cartilage* vol. 29 6–7 (2021).

29. Zhou, R., Hu, W., Waxman, S. G. & Liu, C.-J. Ion channels as therapeutic targets in osteoarthritis. *Trends in Pharmacological Sciences* vol. 46 792–813 (2025).

30. Yu, L. *et al.* Mechanical stress overload promotes NF-κB/NLRP3-mediated osteoarthritis synovitis and fibrosis through Piezo1. *Cellular Signalling* vol. 132 111786 (2025).

31. Zheng, J. *et al.* Directed self-assembly of herbal small molecules into sustained release hydrogels for treating neural inflammation. *Nature Communications* vol. 10 (2019).

32. Feng, Y. H., Zhang, X. P., Hao, Y. Y., Ren, G. Y. & Guo, X. D. Simulation study of the pH sensitive directed self-assembly of rheins for sustained drug release hydrogel. *Colloids and Surfaces B: Biointerfaces* vol. 195 111260 (2020).

33. Liang, X. *et al.* Enhanced Mechanical Strength and Sustained Drug Release in Carrier-Free Silver-Coordinated Anthraquinone Natural Antibacterial Anti-Inflammatory Hydrogel for

Infectious Wound Healing. *Advanced Healthcare Materials* vol. 13 (2024).

34. Donati, B., Lorenzini, E. & Ciarrocchi, A. BRD4 and Cancer: going beyond transcriptional regulation. *Molecular Cancer* vol. 17 (2018).

35. Shi, J. & Vakoc, C. R. The Mechanisms behind the Therapeutic Activity of BET Bromodomain Inhibition. *Molecular Cell* vol. 54 728–736 (2014).

36. Huang, B., Yang, X.-D., Zhou, M.-M., Ozato, K. & Chen, L.-F. Brd4 Coactivates Transcriptional Activation of NF-κB via Specific Binding to Acetylated RelA. *Molecular and Cellular Biology* vol. 29 1375–1387 (2009).

37. Wu, S.-Y., Lee, A.-Y., Lai, H.-T., Zhang, H. & Chiang, C.-M. Phospho Switch Triggers Brd4 Chromatin Binding and Activator Recruitment for Gene-Specific Targeting. *Molecular Cell* vol. 49 843–857 (2013).

38. Vasylyev, D. V., Zhao, P., Schulman, B. R. & Waxman, S. G. Interplay of Nav1.8 and Nav1.7 channels drives neuronal hyperexcitability in neuropathic pain. *Journal of General Physiology* vol. 156 (2024).

39. Emery, E. C., Luiz, A. P. & Wood, J. N. Nav1.7 and other voltage-gated sodium channels as drug targets for pain relief. *Expert Opinion on Therapeutic Targets* vol. 20 975–983 (2016).

40. Liang, F. *et al.* Microalgae-Derived Extracellular Vesicles Synergize with Herbal Hydrogel for Energy Homeostasis in Osteoarthritis Treatment. *ACS Nano* vol. 19 8040–8057 (2025).

41. Jalali, A. *et al.* OD1, the first toxin isolated from the venom of the scorpion Odonthobuthus doriae active on voltage-gated Na+ channels. *FEBS Letters* vol. 579 4181–4186 (2005).

42. Jewett, K. A. *et al.* Tumor necrosis factor enhances the sleep-like state and electrical stimulation induces a wake-like state in co-cultures of neurons and glia. *European Journal of Neuroscience* vol. 42 2078–2090 (2015).

43. Longo, U. G. *et al.* Induced Models of Osteoarthritis in Animal Models: A Systematic Review.

Biology vol. 12 283 (2023).

44. Zaki, S., Blaker, C. L. & Little, C. B. OA foundations – experimental models of osteoarthritis. *Osteoarthritis and Cartilage* vol. 30 357–380 (2022).

Acknowledgment

This work was supported from Project of International Cooperation and Exchanges of the National Natural Science Foundation of China (No. 82020108017, D.C), 2025 Henan Provincial Medical Science and Technology Research Plan - Major Provincial-Ministerial Jointly FundedProject (SBGJ202501009, D.C.), China Postdoctoral Science Foundation under Grant Number(2025M781970, Q.Z.), Innovation Group Project of National Natural Science Foundation of China(No.81921002, D.C.), National Key Research and Development Program of China(No.2017FYA0205301, D.C.), Projects of Shanghai Science and Technology Commission (21DZ2203200,and No. 20142201300, D.C.), and Natural Science Foundation of Shanghai (No. 22ZR1467600, D.C.).

Author Contributions Statement

Q.Z., T.X., Z.D., X.L., and Y.Z. contributed equally to this work. Q.Z., T.X., Z.D., X.L., and Y.Z. designed and performed the majority of experiments, analyzed the data, and drafted the manuscript.

L.P., Z.G., W.W. (Weicheng Wang), and B.Z. were responsible for nanoparticle synthesis, hydrogel construction, and physicochemical characterization.

Z.L., G.Y., H.Z., and Z.S. assisted with animal experiments and histological analyses.

Q.L., J.L., Z.R., and Z.Y. performed bioinformatics analyses, including single-cell RNA sequencing and transcriptomic profiling.

W.W. (Wei Wang) and Y.L. contributed to pain behavior assessment and imaging analysis.

H.L. and J.M.F. provided critical technical support and conceptual advice.

All authors discussed the results, critically revised the manuscript, and approved the final version.

Competing Interests Statement

The authors declare no competing interests.

Figure Legends

Figure 1. Identification of degeneration-associated chondrocyte subpopulations via single-cell RNA sequencing (scRNA-seq).

Note: (A) Schematic workflow of scRNA-seq: Knee joint cartilage was collected from Sham (control) and destabilization of the medial meniscus (DMM) (OA model, 8 weeks post-surgery) mice for 10x Genomics single-cell analysis (Created in BioRender. Q.Zhao (2026) https://BioRender.com/629f3gb); (B) t-Distributed Stochastic Neighbor Embedding (t-SNE) plot displaying 19 distinct cell clusters; (C) Annotation of the 19 clusters based on marker gene expression; (D) Dot plot visualizing the expression levels and percent expressed of top marker genes used to annotate cell clusters. Dot size represents the percentage of cells expressing the gene, and color intensity indicates average expression level; (E) Bar graph showing the distribution of cell populations in cartilage from Sham and DMM groups; (F) Dot plot illustrating changes in cell proportions between Sham and DMM groups. Data for single-cell analysis were derived from pooled cartilage samples (n = 1 biological replicate per group consisting of pooled tissue from 3 mice) to maximize cell yield for cluster identification; therefore, statistical significance testing was not applied to the cell proportion changes in this exploratory phase. OA: osteoarthritis. Source data are provided as a Source Data file.

Figure 2. Evaluation of Nav1.7 expression and functional status in ATDC5 cells under osteoarthritis (OA) conditions.

Note: (A) Experimental workflow of TNF-α-induced OA model in ATDC5 cells (Created in BioRender. Q.Zhao (2026) https://BioRender.com/or5jts9); (B) RT-qPCR analysis of *Scn9a* gene expression in ATDC5 cells, Statistical analysis was performed using a two-tailed unpaired t-test ($t = 9.26$, $df = 4$, $p < 0.001$, 95% CI = 0.425 to 0.788); (C) WB analysis of Nav1.7 protein expression, Statistical analysis was performed using a two-tailed unpaired t-test ($t = 168$, $df = 4$, $p < 0.001$,

95% CI = 7.89 to 8.16); (D) Immunofluorescence staining of Nav1.7 protein localization in ATDC5 cells (scale bar: 25 μm); (E) WB analysis of Nav1.7 distribution in membrane and cytoplasmic fractions (Two-tailed unpaired t-test, t = 59.7, df = 4, $p < 0.001$, 95% CI = 2.85 to 3.13); (F) Patch-clamp recording of sodium current changes under varying voltage stimuli in ATDC5 cells; (G) Comparative analysis of sodium current responses across different groups; (H) Sodium current responses before and after tetrodotoxin (TTX) treatment; (I) Patch-clamp analysis comparing sodium current responses between TNF-α + TTX and TNF-α + ProTx II groups; (J) Superimposed current traces of TTX-Sensitive (TTX-S) (red) and ProTx II-sensitive (blue) components normalized by peak current amplitude; (K) Analysis of inactivation time constants and peak times of TTX-S and ProTx II-S sodium currents Statistical analysis was performed using a two-tailed unpaired t-test (Left panel [Time constant]: t = 0.655, df = 4, $p = 0.548$, 95% CI = -0.173 to 0.279; Right panel [Time to peak]: t = 1.46, df = 4, $p = 0.217$, 95% CI = -0.0718 to 0.232). Data are presented as mean ± standard deviation (SD) of n = 3 independent biological replicates. Individual data points represent biological replicates. Source data are provided as a Source Data file.

Figure 3. BRD4 regulates Scn9a transcription and mediates histone acetylation modifications. Note: (A) Schematic diagram illustrating BRD4-mediated regulation of Scn9a transcription (Created in BioRender. Q. Zhao (2026) https://BioRender.com/kkgzxz8); (B) RT–qPCR analysis showing Scn9a mRNA expression in ATDC5 cells under different treatments; (C) Western blot analysis of Nav1.7 protein expression in ATDC5 cells; (D) Immunofluorescence co-staining of Nav1.7 and BRD4 in ATDC5 cells showing changes in Nav1.7 expression and Nav1.7/BRD4 double-positive cells (scale bar, 25 μm); (E) Chromatin immunoprecipitation followed by quantitative PCR (ChIP–qPCR) analysis showing H3ac enrichment at the Scn9a promoter region; (F) Dual-luciferase reporter assay evaluating transcriptional activity of the Scn9a promoter;TNF-

α stimulation increased Scn9a transcription and Nav1.7 protein expression, whereas BRD4 knockdown significantly suppressed these effects. Immunofluorescence analysis showed reduced Nav1.7 expression and decreased Nav1.7/BRD4 co-localization after BRD4 silencing. ChIP-qPCR demonstrated that BRD4 knockdown reduced histone H3 acetylation enrichment at the Scn9a promoter. Consistently, dual-luciferase assays showed that BRD4 silencing attenuated Scn9a promoter activity. Data are presented as mean ± standard deviation (SD) from three independent biological replicates. Individual data points represent biological replicates. NC, negative control. Source data are provided as a Source Data file.

Figure 4. Preparation and characterization of the Rh-Gel@CCM@PM.

Note: (A) Schematic illustration of the construction of Rh-Gel@CCM@PM (Created in BioRender. Q.Zhao (2026) https://BioRender.com/z0nuvkm); (B) UV-Vis absorption spectra showing characteristic peaks of different components; (C) Fluorescence spectra displaying the intrinsic fluorescence properties of Rhein-Based Hydrogel (Rh-Gel); (D) Zeta potential analysis revealing surface charge differences between Rh-Gel and Rh-Gel@CCM@PM, Statistical analysis was performed using a two-tailed unpaired t-test ($t = 3.104$, $df = 4$, $p = 0.0361$, 95% CI = 1.162 to 20.84); (E) SEM image of the Rh-Gel showing a 3D nanofiber network (scale bar: 1 μm); (F) Visual comparison of gel states and fluidity changes at 25 °C and 37 °C over time; (G) UV-Vis spectra confirming dual absorption peaks of Rh and FITC-CCM@PM within Rh-Gel@CCM@PM; (H) Zeta potential analysis of Rh-Gel@CCM@PM surface charge characteristics, Statistical analysis was performed using one-way ANOVA ($F(2, 6) = 25.65$, $p = 0.0011$); (I) Confocal microscopy demonstrating colocalization of FITC-CCM@PM (green) with Rh-Gel (red) signals (scale bar: 100 μm); (J) Release profiles of Rh-Gel@CCM@PM under pH 7.4 and pH 5.5 buffer conditions, Statistical analysis at day 7 was performed using a two-tailed unpaired t-test ($t = 3.051$, $df = 4$, $p = 0.0380$); (K) TEM monitoring of CCM@PM particle size changes during the release

process (scale bar: 100 nm); (L) WB analysis of cartilage membrane proteins CD44, Integrin β1, and N-cadherin in Rh-Gel@CCM@PM. Data are presented as mean ± standard deviation (SD) of n = 3 independent experiments. Individual data points represent biological replicates. CCM: chondrocyte cell membrane. Source data are provided as a Source Data file.

Figure 5. Rh-Gel@CCM@PM alleviates TNF-α-induced mitochondrial dysfunction in ATDC5 cells.

Note: (A) Schematic diagram illustrating experimental grouping and treatment procedures in TNF-α–stimulated ATDC5 cells (Created in BioRender. Q. Zhao (2026) https://BioRender.com/u7qfyy8); (B–C) Western blot analysis of BRD4 and Nav1.7 protein expression in ATDC5 cells following different treatments; (D) RT–qPCR analysis of Nav1.7 and Brd4 mRNA expression levels; (E) Detection of intracellular reactive oxygen species (ROS) using DCFH-DA fluorescence probes (scale bar, 25 μm); (F–G) JC-1 staining used to assess mitochondrial membrane potential (ΔΨm) with quantification of the JC-1 aggregate/monomer (A/M) fluorescence ratio (scale bar, 25 μm); (H) Transmission electron microscopy (TEM) images showing mitochondrial ultrastructure and cristae morphology in ATDC5 cells (scale bar, 500 nm); (I) Western blot analysis of mitochondrial function-related proteins TFAM and ATPB; (J) Colorimetric assay measuring intracellular ATP levels. TNF-α stimulation induced mitochondrial dysfunction characterized by increased ROS production, decreased mitochondrial membrane potential, disrupted mitochondrial ultrastructure, and reduced mitochondrial functional proteins and ATP levels. Treatment with CCM@PM partially improved these parameters, whereas Rh-Gel@CCM@PM produced a more pronounced restoration of mitochondrial function. Data are presented as mean ± standard deviation (SD) from three independent biological replicates. Individual data points represent biological replicates. CCM, chondrocyte cell membrane; Rh-Gel, Rhein-based hydrogel. Source data are provided as a Source Data file.

Figure 6. Rh-Gel@CCM@PM hydrogel regulates cartilage anabolism and catabolism in ATDC5 cells following TNF-α stimulation.

Note: (A) Schematic illustration of experimental grouping and treatment procedures in TNF-α–stimulated ATDC5 cells (Created in BioRender. Q. Zhao (2026) https://BioRender.com/279h19v); (B) RT–qPCR analysis of mRNA expression levels of inflammatory cytokines IL-6 and IL-1β; (C) Western blot analysis of IL-6 protein expression;

(D) Immunofluorescence staining showing IL-6 protein expression (scale bar, 25 μm); (E) RT–qPCR analysis of cartilage anabolic markers Sox9 and Col2a1; (F) Western blot analysis of SOX9 and COL II protein expression;

(G) Immunofluorescence staining of SOX9 and COL II expression (scale bar, 25 μm); (H) RT–qPCR analysis of mRNA expression of matrix degradation-related genes Mmp13, Adamts4, and Adamts5; (I) Western blot analysis of MMP13 protein expression; (J–K) Quantitative analysis; (J) and representative immunofluorescence images (K) of MMP13 expression (scale bar, 25 μm). TNF-α stimulation increased inflammatory cytokine expression and cartilage matrix–degrading enzymes while suppressing anabolic markers in ATDC5 cells. Treatment with Rh-Gel and CCM@PM partially reduced inflammatory responses and catabolic gene expression and restored anabolic marker levels. Notably, Rh-Gel@CCM@PM treatment produced the most pronounced effects, significantly suppressing inflammatory and catabolic markers while enhancing anabolic protein expression, indicating restoration of cartilage metabolic balance. Data are presented as mean ± standard deviation (SD) from three independent biological replicates. Individual data points represent biological replicates. CCM, chondrocyte cell membrane; Rh-Gel, Rhein-based hydrogel. Source data are provided as a Source Data file.

Figure 7. Effects of Rh-Gel@CCM@PM on cartilage degradation and pain behavior in destabilization of the medial meniscus (DMM)-induced osteoarthritis (OA).

Note: (A) Schematic illustration of DMM model establishment and treatment strategies for each group (Created in BioRender. Q. Zhao (2026) https://BioRender.com/4o84enj); (B) Western blot analysis of BRD4 and Nav1.7 protein expression in knee cartilage tissue; (C) Open field test assessing spontaneous locomotor activity in DMM mice; (D) von Frey mechanical stimulation test evaluating mechanical pain threshold; (E) Micro-CT three-dimensional reconstruction analysis of subchondral bone architecture; (F) Quantitative analysis of bone volume per total volume (BV/TV), bone mineral density (BMD), and trabecular thickness (Tb.Th); (G) Hematoxylin and eosin (H&E) and Safranin O/Fast Green (SO/FG) staining used to evaluate cartilage morphology (scale bars, 100 μm); (H) Osteoarthritis Research Society International (OARSI) scoring to assess cartilage degeneration severity; (I) Immunofluorescence staining showing expression of COL II, ACAN, and IL-6 in cartilage tissue (scale bar, 50 μm). DMM surgery induced cartilage degeneration, subchondral bone remodeling, and pain-related behavioral changes. Treatment with Rh-Gel and CCM@PM partially alleviated these pathological alterations. Notably, Rh-Gel@CCM@PM treatment produced the most pronounced therapeutic effects, reducing BRD4 and Nav1.7 expression, improving locomotor activity and mechanical pain thresholds, restoring subchondral bone architecture, preserving cartilage morphology, decreasing inflammatory marker IL-6, and increasing cartilage matrix proteins COL II and ACAN. Data are presented as mean ± standard deviation (SD) (n = 6 biologically independent male C57BL/6J mice per group). Individual data points represent biological replicates. CCM, chondrocyte cell membrane; Rh-Gel, Rhein-based hydrogel; DMM, destabilization of the medial meniscus. Source data are provided as a Source Data file.

Figure 8. Effects of Rh-Gel@CCM@PM on cartilage degradation and pain behavior in monosodium iodoacetate (MIA)-induced osteoarthritis (OA).

(A) Schematic diagram illustrating the establishment of the MIA-induced OA model and treatment

strategies for each group (Created in BioRender. Q. Zhao (2026) https://BioRender.com/y4o2jcr); (B) Open field test assessing locomotor activity; (C) von Frey mechanical stimulation test evaluating mechanical pain sensitivity; (D) Micro-CT three-dimensional reconstruction analysis of subchondral bone structure in the knee joint; (E) Quantitative analysis of bone volume per total volume (BV/TV), bone mineral density (BMD), and trabecular thickness (Tb.Th); (F) Hematoxylin and eosin (H&E) and Safranin O/Fast Green (SO/FG) staining used to evaluate cartilage structure (scale bars, 100 μm); (G) Osteoarthritis Research Society International (OARSI) scoring to assess cartilage degeneration severity; (H) Quantification of glycosaminoglycan (GAG) content in cartilage tissue; (I) Quantitative analysis of cartilage thickness; (J) Western blot analysis of BRD4 and Nav1.7 expression in joint tissues; (K) Immunofluorescence staining showing COL II, ACAN, and IL-6 expression in cartilage tissue (scale bar, 50 μm); MIA injection induced severe cartilage degeneration, subchondral bone remodeling, and pain-related behavioral changes. Treatment with Rh-Gel and CCM@PM partially alleviated these pathological alterations. Notably, Rh-Gel@CCM@PM treatment produced the most pronounced therapeutic effects, improving locomotor activity and mechanical pain thresholds, restoring subchondral bone architecture, preserving cartilage morphology and thickness, increasing GAG content, suppressing BRD4 and Nav1.7 expression, and enhancing cartilage matrix proteins COL II and ACAN while reducing inflammatory marker IL-6. Data are presented as mean ± standard deviation (SD) (n = 6 biologically independent male C57BL/6J mice per group). Individual data points represent biological replicates. CCM, chondrocyte cell membrane; Rh-Gel, Rhein-based hydrogel. Source data are provided as a Source Data file.

Figure 9. The Rh-Gel@CCM@PM facilitates targeted degradation of BRD4 to suppress the voltage-gated sodium channel Nav1.7, thereby modulating cartilage degeneration and attenuating osteoarthritis (OA) progression. Rh-Gel: Rhein-Based Hydrogel; CCM:

chondrocyte cell membrane; PM: Peptide-Modified Mesoporous Silica Nanoparticle. (Created in BioRender. Q.Zhao (2026) https://BioRender.com/j5fs8zw)

Osteoarthritis is driven by epigenetic dysregulation, yet targeted therapies remain elusive. Here, the authors develop a cartilage-targeting hydrogel delivering BRD4-degrading PROTACs to suppress the BRD4- Nav1.7 axis and alleviate osteoarthritis.

Peer review information: *Nature Communications* thanks the anonymous reviewers for their contribution to the peer review of this work. A peer review file is available.

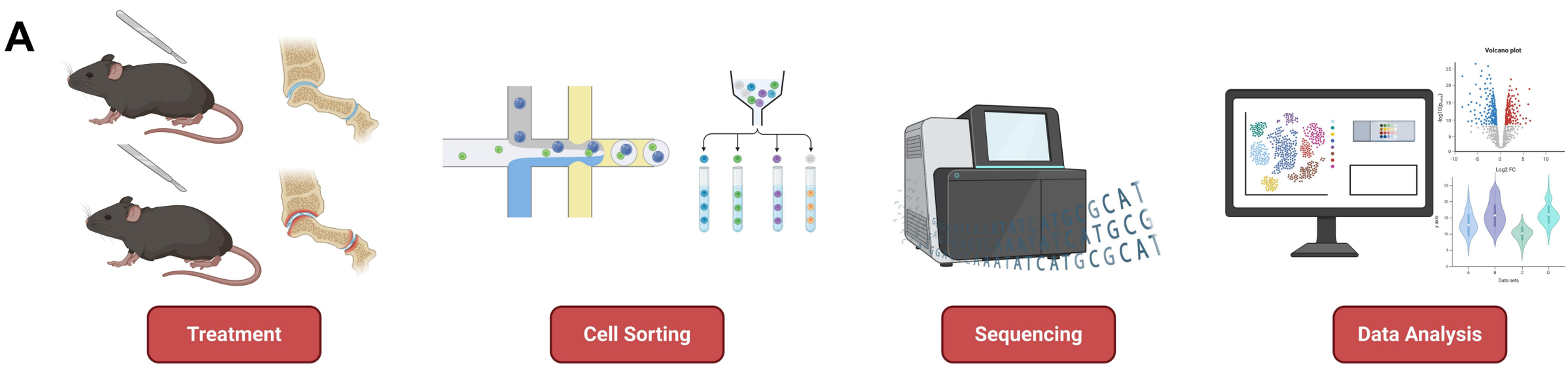
A
Treatment
Cell Sorting
Sequencing
Data Analysis
Volcano plot
Log2 FC
Data sets
B
OA
Sham
tSNE_1
tSNE_2
C
t-SNE projection
Reticular cells
Dendritic cells
Granulocyte_1
Monocytes likes
Monocyte-macrophages
Granulocyte_2
Granulocyte_3
B cells
Degenerative chondrocytes
Chondrocytes
Osteoblast
T cells
Erythrocytes
Progenitor cells
Smooth muscle cells
D
Percent Expressed
Average Expression
Features
Identity
E
Ratio
Sample
Var1
F
Granulocyte_1
Chondrocytes
Monocyte−macrophages
Degenerative chondrocytes
Granulocyte_2
B cells
Monocytes likes
T cells
Reticular cells
Osteoblast
Dendritic cells
Granulocyte_3
Erythrocytes
Progenitor cells
Smooth muscle cells
Percentage
group

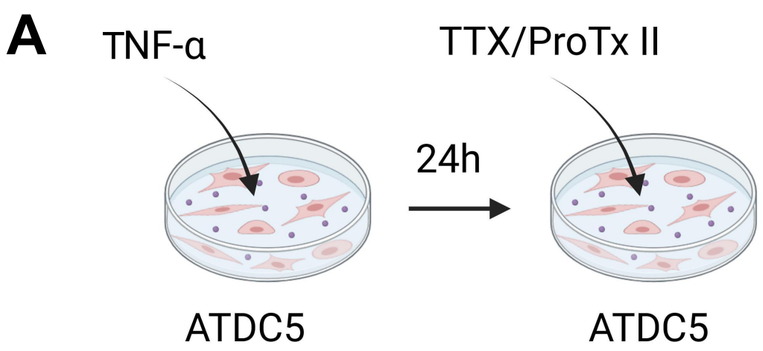
A
TNF-α
TTX/ProTx II
24h
ATDC5
ATDC5

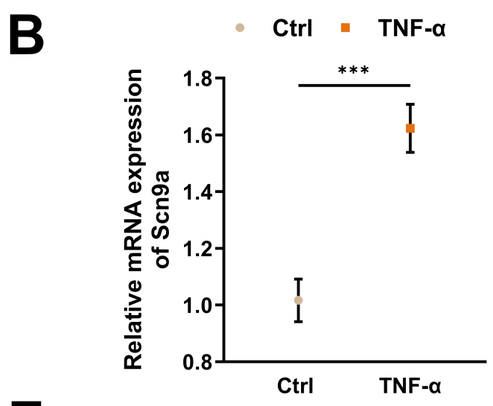
B
Ctrl
TNF-α
***
Relative mRNA expression of Scn9a
1.8
1.6
1.4
1.2
1.0
0.8
Ctrl
TNF-α

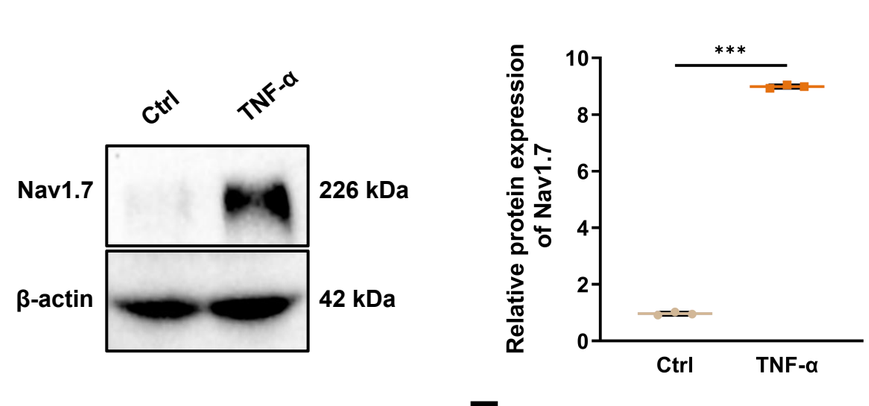
C
Ctrl
TNF-α
Nav1.7
226 kDa
β-actin
42 kDa
***
Relative protein expression of Nav1.7
10
8
6
4
2
0
Ctrl
TNF-α

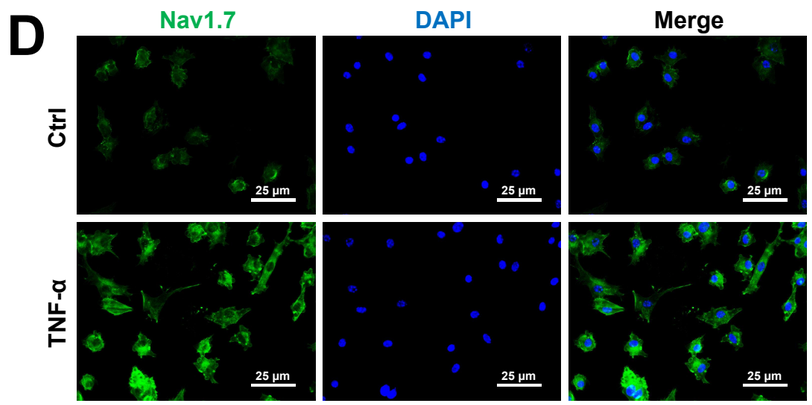
D
Nav1.7
DAPI
Merge
Ctrl
TNF-α
25 μm

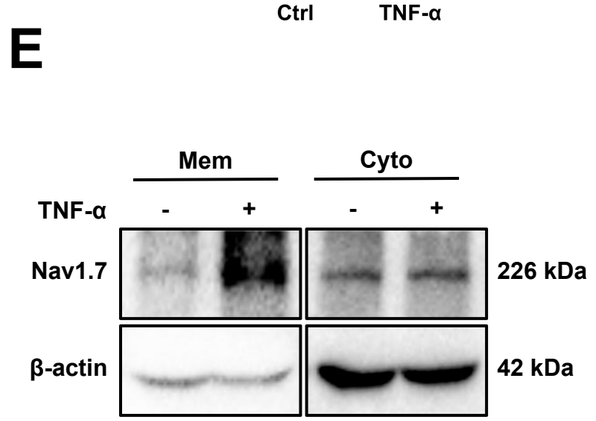
E
Mem
Cyto
TNF-α
-
+
-
+
Nav1.7
226 kDa
β-actin
42 kDa

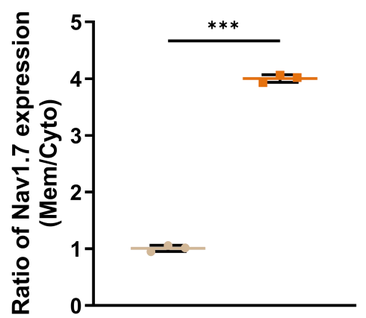
***
Ratio of Nav1.7 expression (Mem/Cyto)
5
4
3
2
1
0
Ctrl
TNF-α

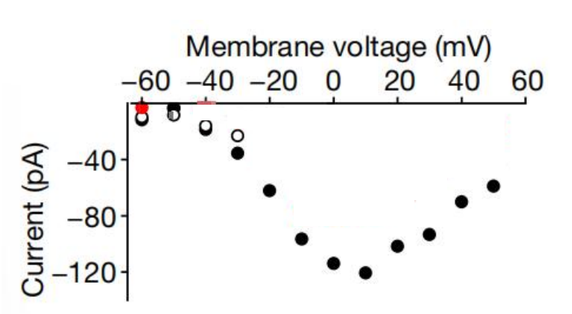
F
Membrane voltage (mV)
−60
−40
−20
0
20
40
60
Current (pA)
−40
−80
−120

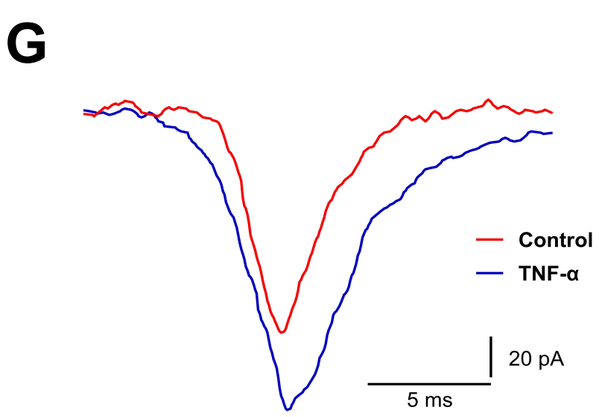
G
Control
TNF-α
20 pA
5 ms

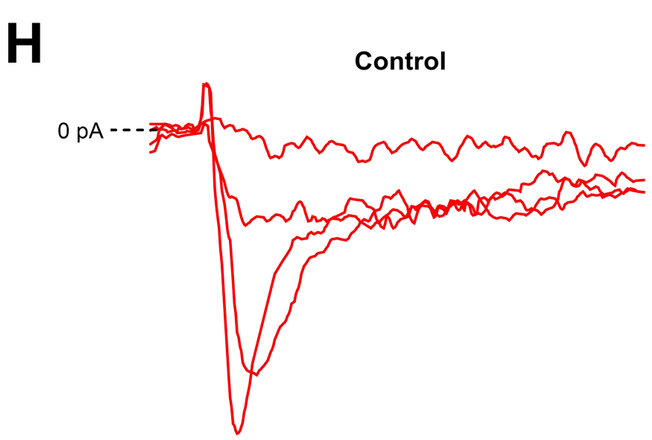
H
Control
0 pA

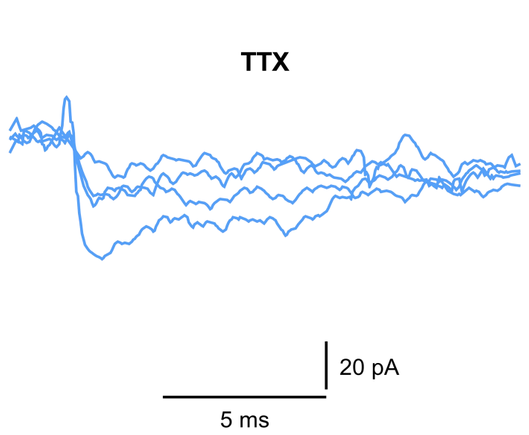
TTX
20 pA
5 ms

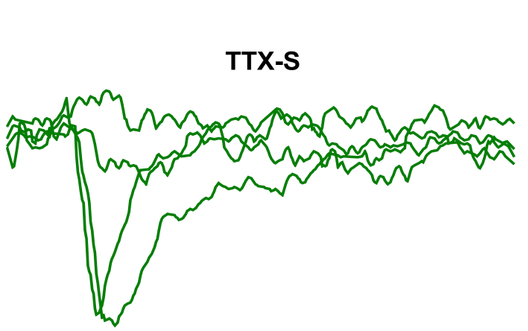
TTX-S

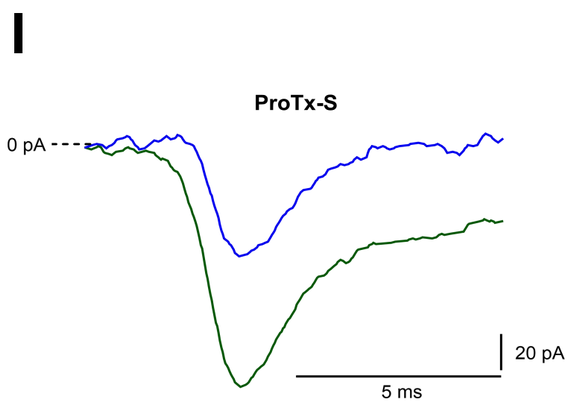
I
ProTx-S
0 pA
20 pA
5 ms

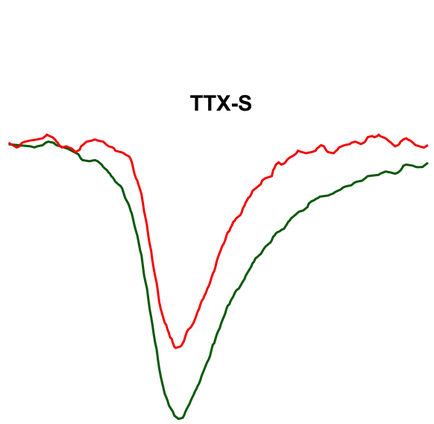
TTX-S

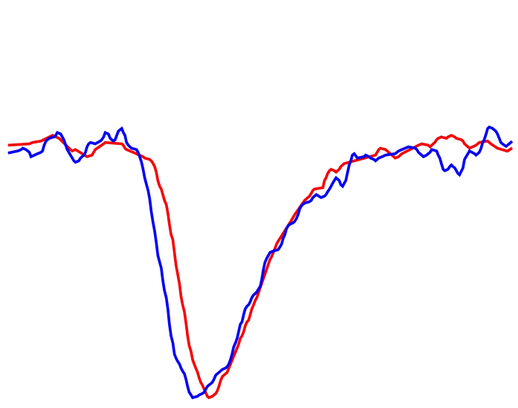
J

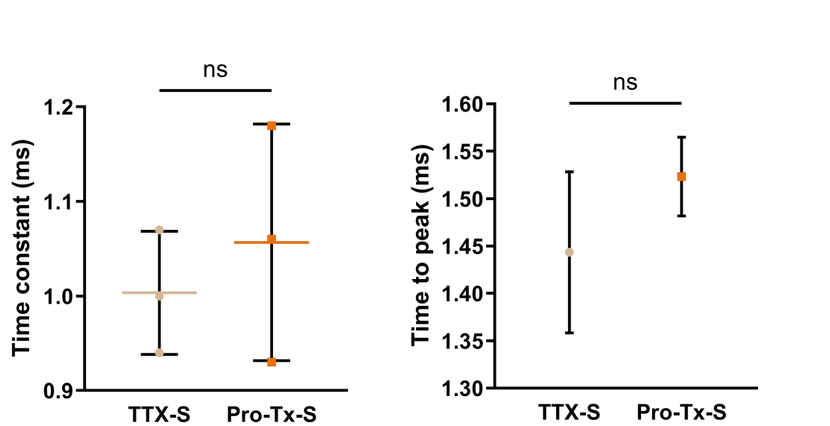
K
ns
Time constant (ms)
1.2
1.1
1.0
0.9
TTX-S
Pro-Tx-S
ns
Time to peak (ms)
1.60
1.55
1.50
1.45
1.40
1.35
1.30
TTX-S
Pro-Tx-S

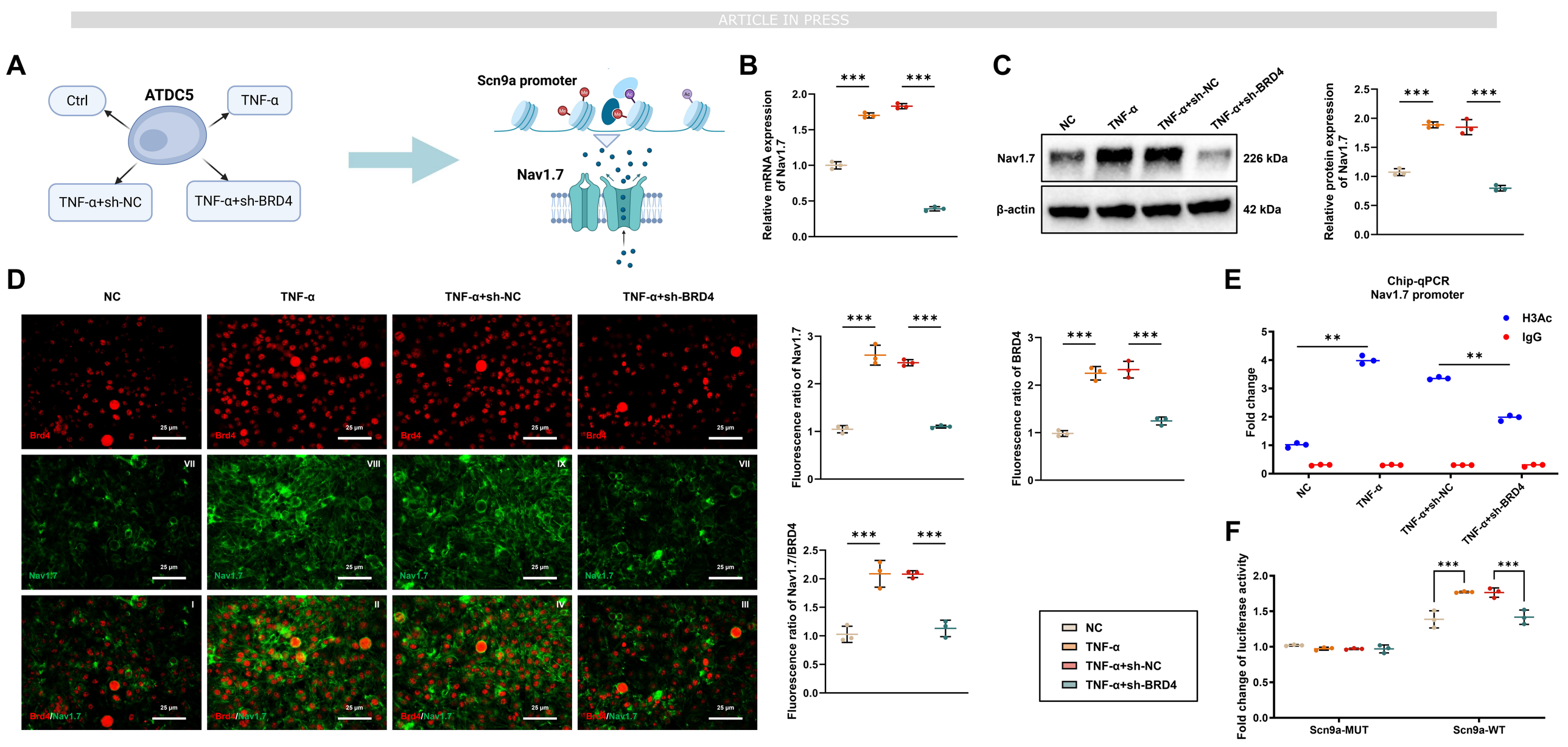
A
Ctrl
ATDC5
TNF-α
TNF-α+sh-NC
TNF-α+sh-BRD4
Scn9a promoter
Nav1.7
B
Relative mRNA expression of Nav1.7
C
NC
TNF-α
TNF-α+sh-NC
TNF-α+sh-BRD4
Nav1.7
226 kDa
β-actin
42 kDa
Relative protein expression of Nav1.7
D
NC
TNF-α
TNF-α+sh-NC
TNF-α+sh-BRD4
Brd4
Nav1.7
Brd4/Nav1.7
25 μm
Fluorescence ratio of Nav1.7
Fluorescence ratio of BRD4
Fluorescence ratio of Nav1.7/BRD4
E
Chip-qPCR
Nav1.7 promoter
H3Ac
IgG
Fold change
F
Fold change of luciferase activity
Scn9a-MUT
Scn9a-WT

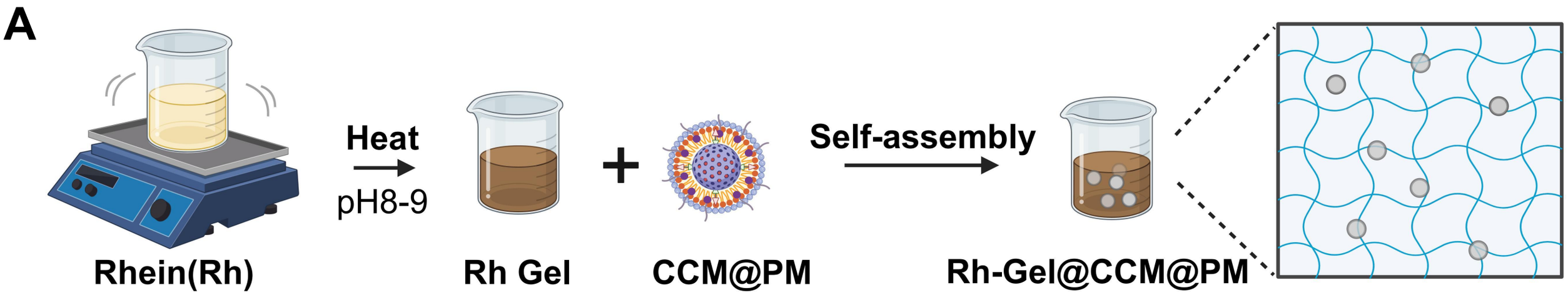
A
Heat
pH8-9
Self-assembly
Rhein(Rh)
Rh Gel
CCM@PM
Rh-Gel@CCM@PM

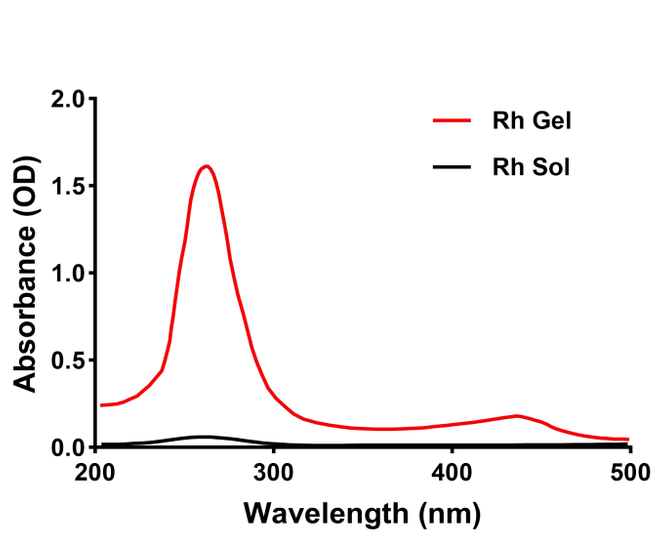
B
Absorbance (OD)
Wavelength (nm)
Rh Gel
Rh Sol

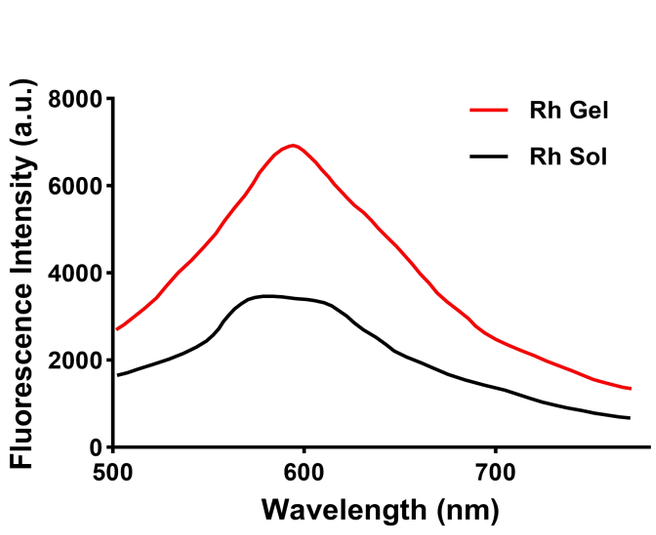
C
Fluorescence Intensity (a.u.)
Wavelength (nm)
Rh Gel
Rh Sol

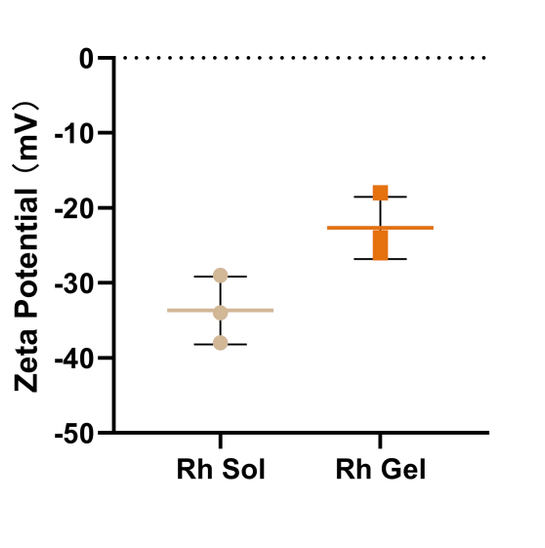
D
Zeta Potential（mV）
Rh Sol
Rh Gel

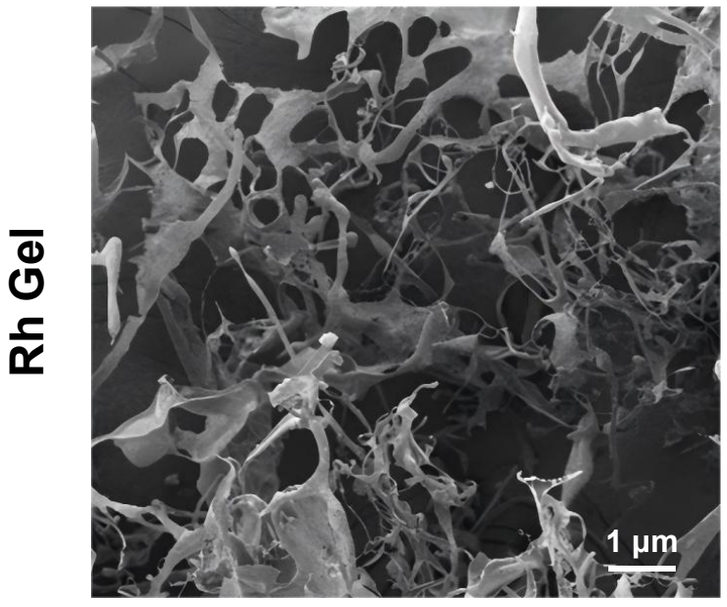
E
Rh Gel
1 μm

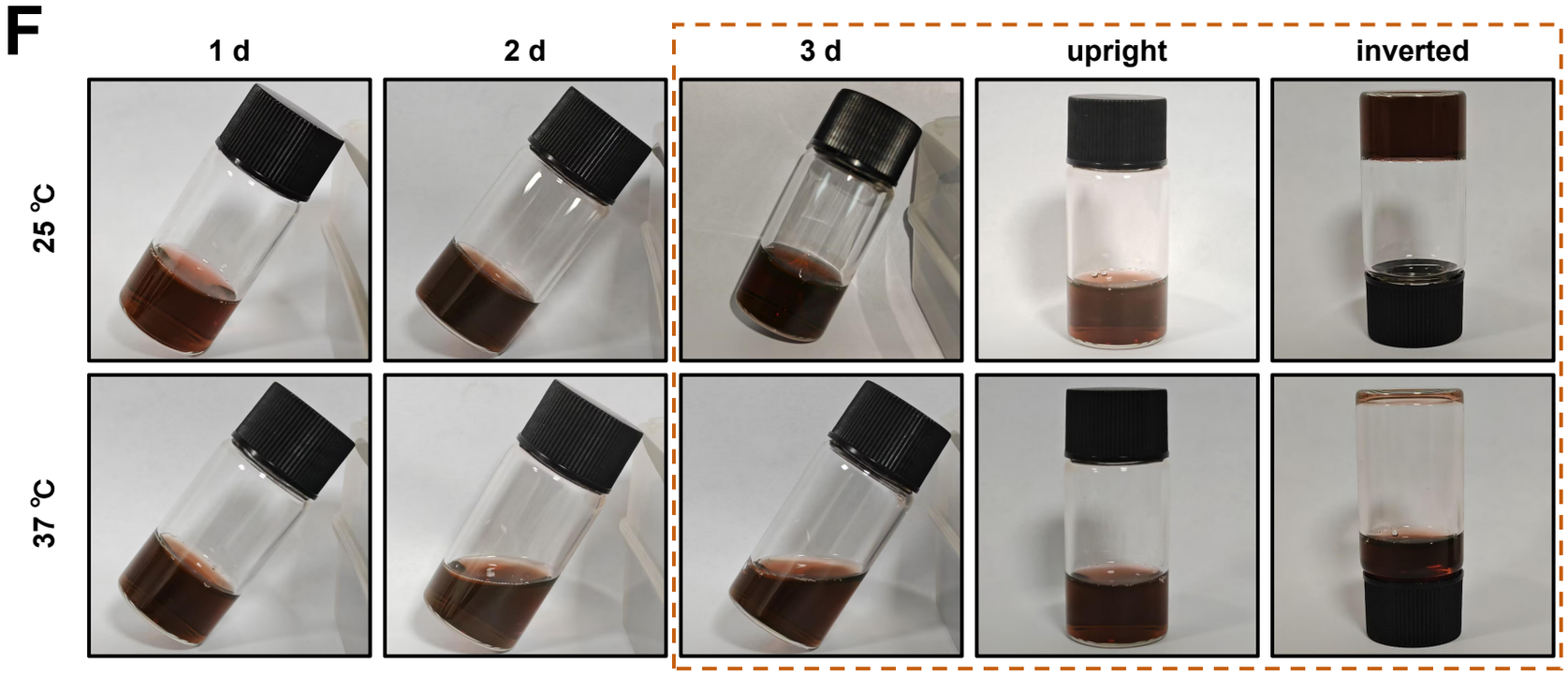
F
1 d
2 d
3 d
upright
inverted
25 ℃
37 ℃

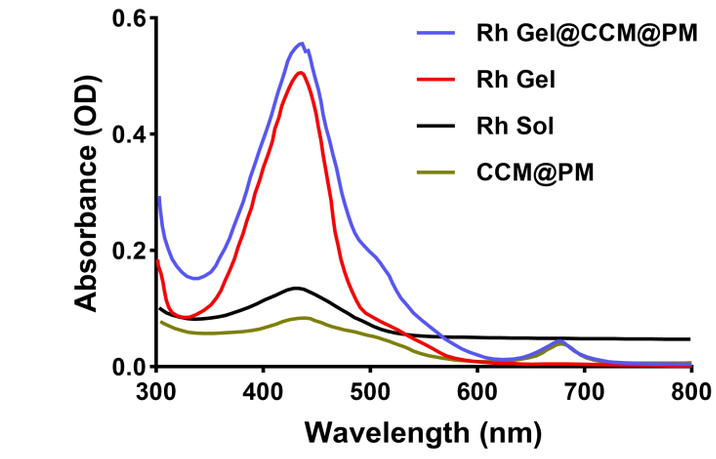
G
Absorbance (OD)
Wavelength (nm)
Rh Gel@CCM@PM
Rh Gel
Rh Sol
CCM@PM

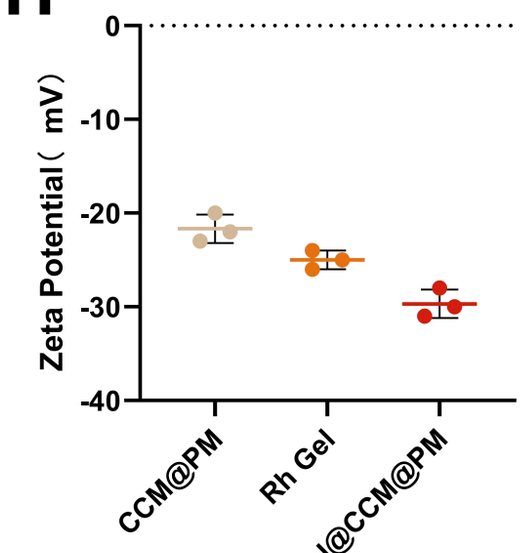
H
Zeta Potential（ mV）
CCM@PM
Rh Gel
Rh Gel@CCM@PM

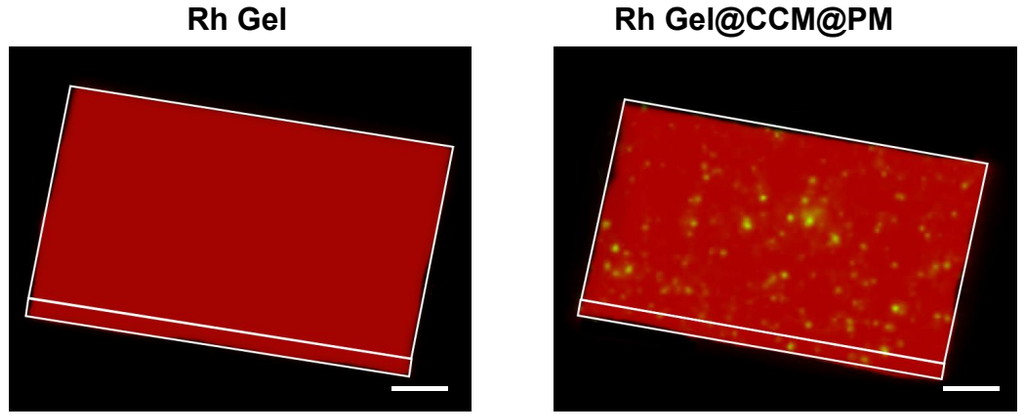
I
Rh Gel
Rh Gel@CCM@PM

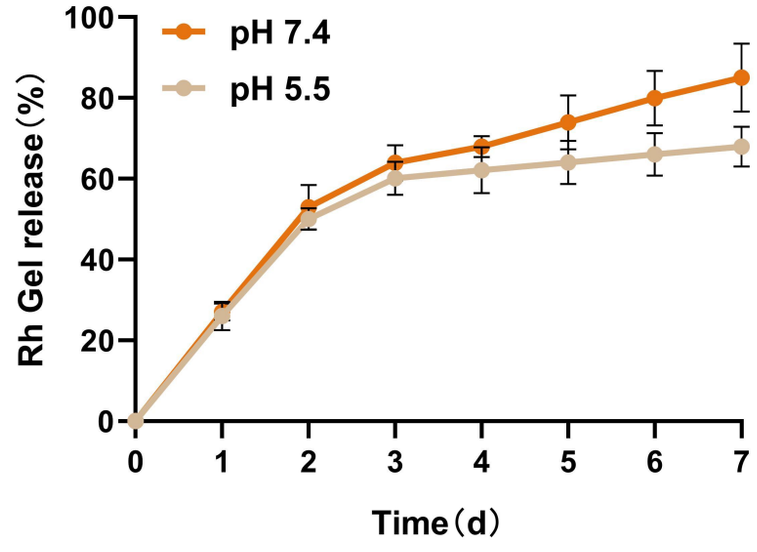
J
Rh Gel release（%）
Time（d）
pH 7.4
pH 5.5

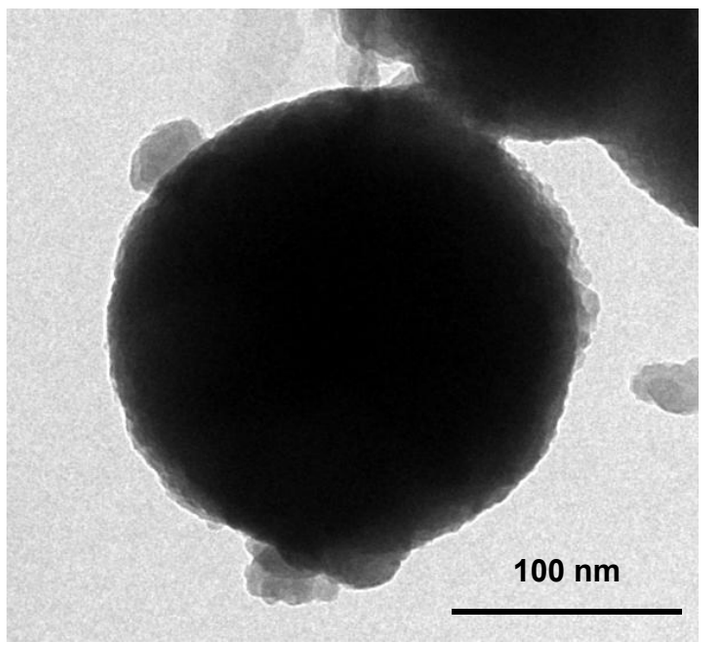
K
100 nm

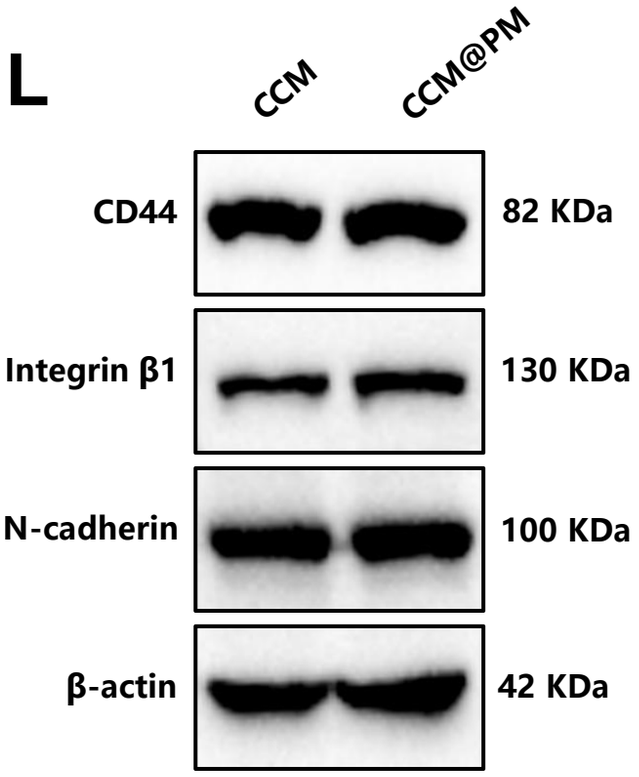
L
CCM
CCM@PM
CD44
82 KDa
Integrin β1
130 KDa
N-cadherin
100 KDa
β-actin
42 KDa

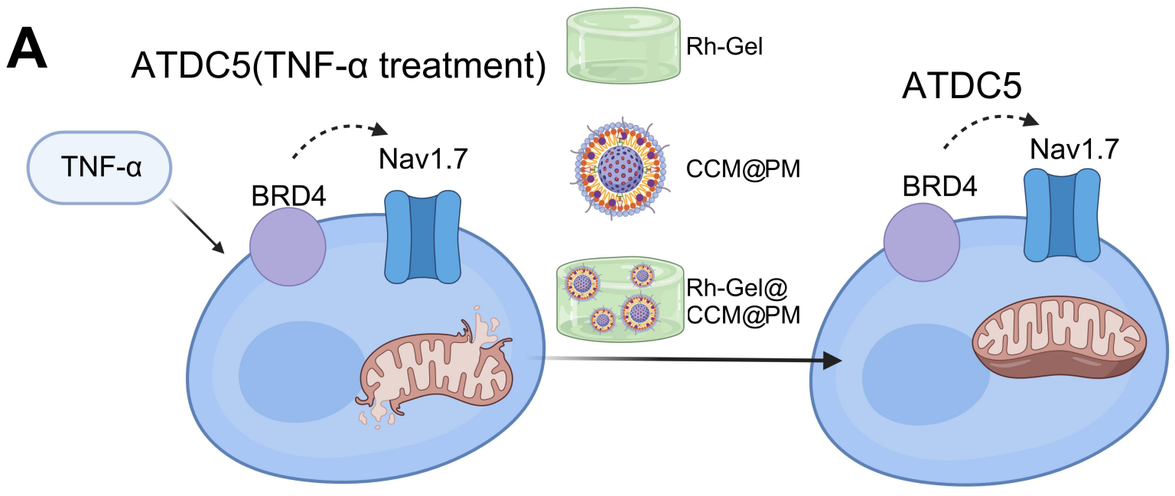
A
ATDC5(TNF-α treatment)
Rh-Gel
CCM@PM
Rh-Gel@
CCM@PM
TNF-α
Nav1.7
BRD4
ATDC5
Nav1.7
BRD4

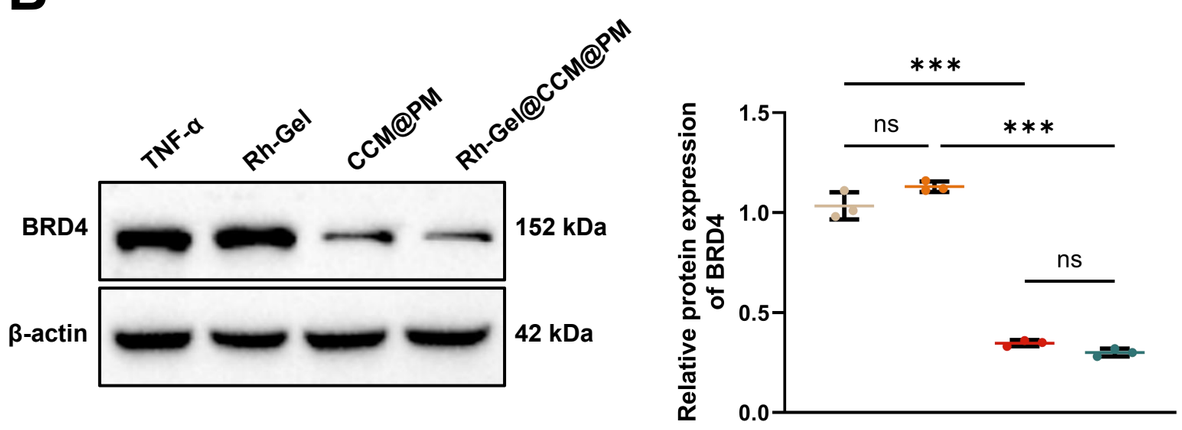
B
TNF-α
Rh-Gel
CCM@PM
Rh-Gel@CCM@PM
BRD4
152 kDa
β-actin
42 kDa
Relative protein expression of BRD4
***
ns
***
ns

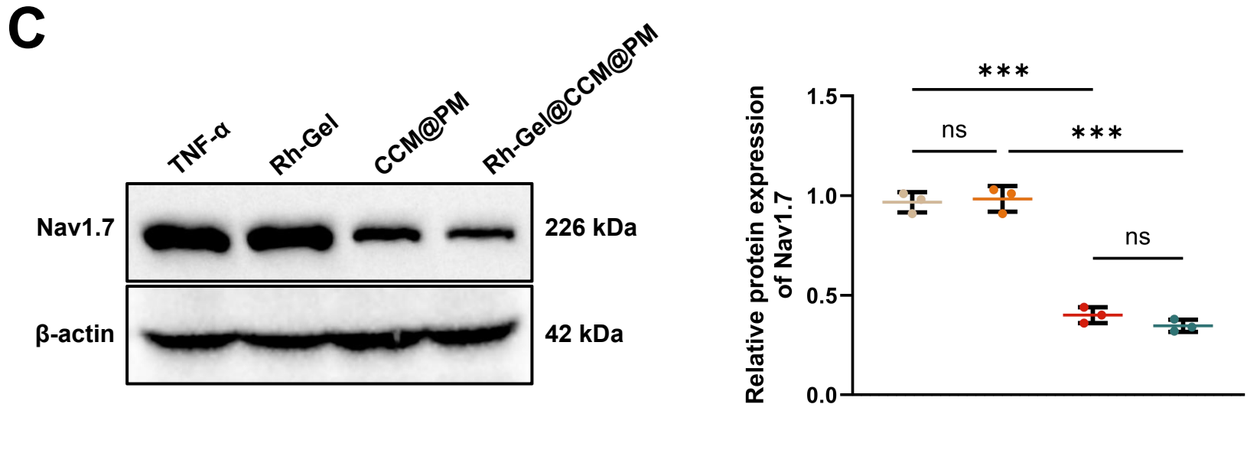
C
TNF-α
Rh-Gel
CCM@PM
Rh-Gel@CCM@PM
Nav1.7
226 kDa
β-actin
42 kDa
Relative protein expression of Nav1.7
***
ns
***
ns

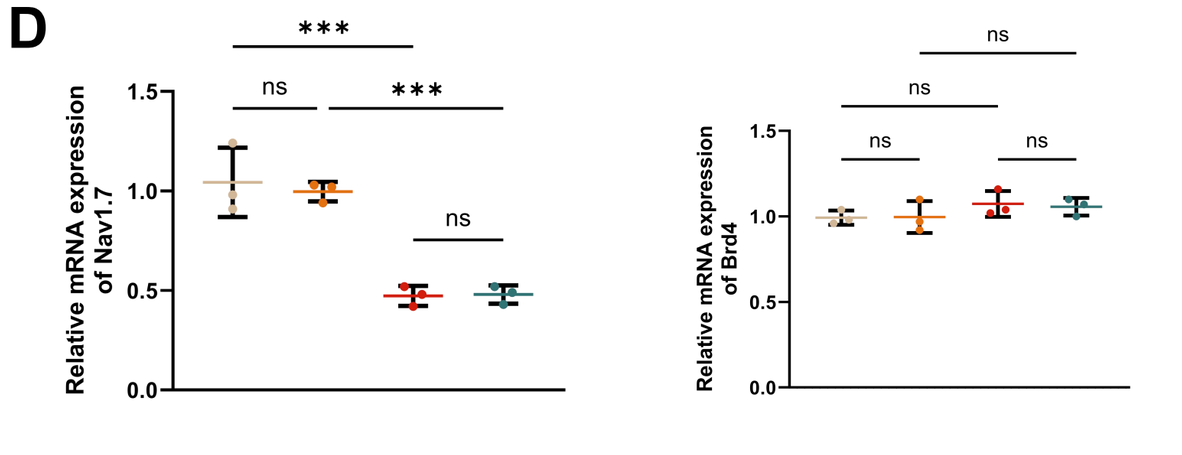
D
Relative mRNA expression of Nav1.7
***
ns
***
ns
Relative mRNA expression of Brd4
ns
ns
ns
ns

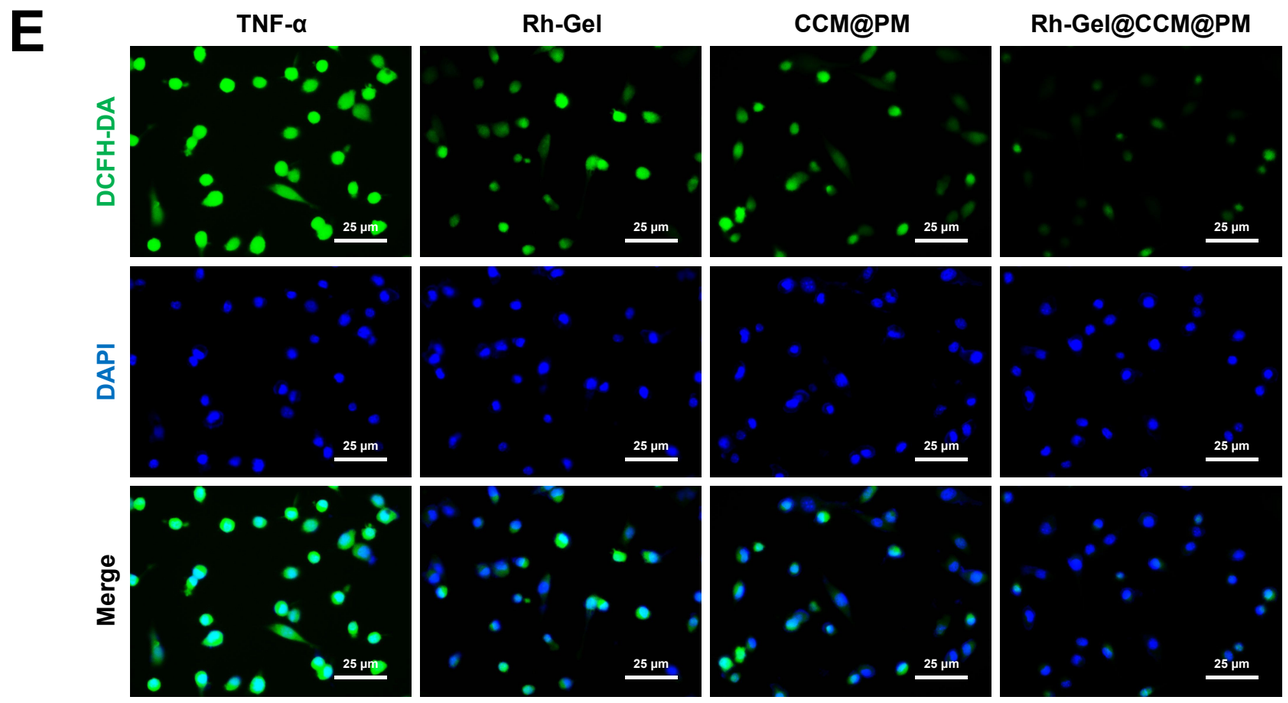
E
TNF-α
Rh-Gel
CCM@PM
Rh-Gel@CCM@PM
DCFH-DA
DAPI
Merge
25 μm

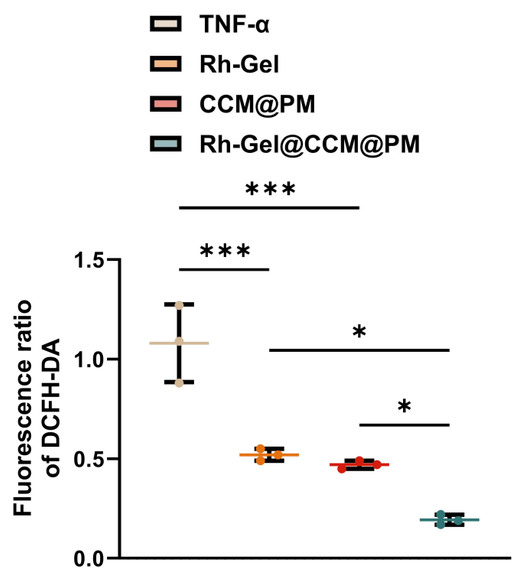
TNF-α
Rh-Gel
CCM@PM
Rh-Gel@CCM@PM
Fluorescence ratio of DCFH-DA
***
***
*
*

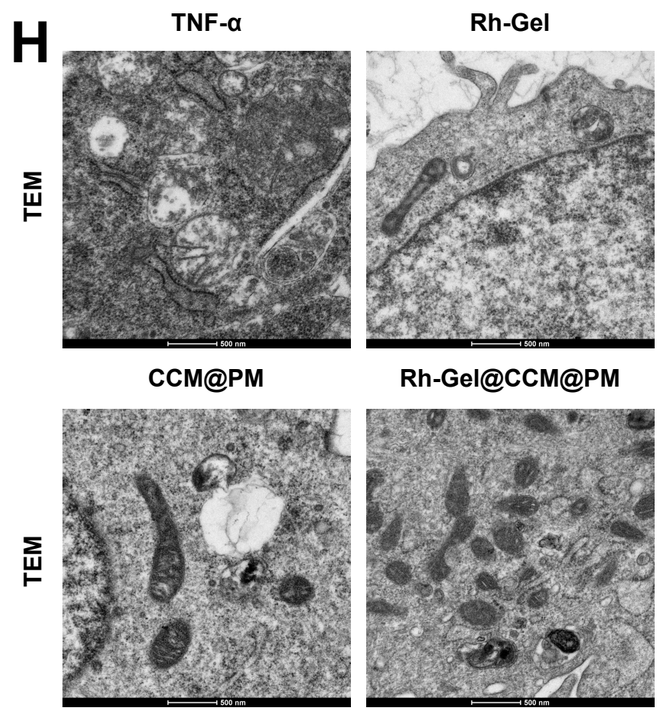
H
TNF-α
Rh-Gel
CCM@PM
Rh-Gel@CCM@PM
TEM
500 nm

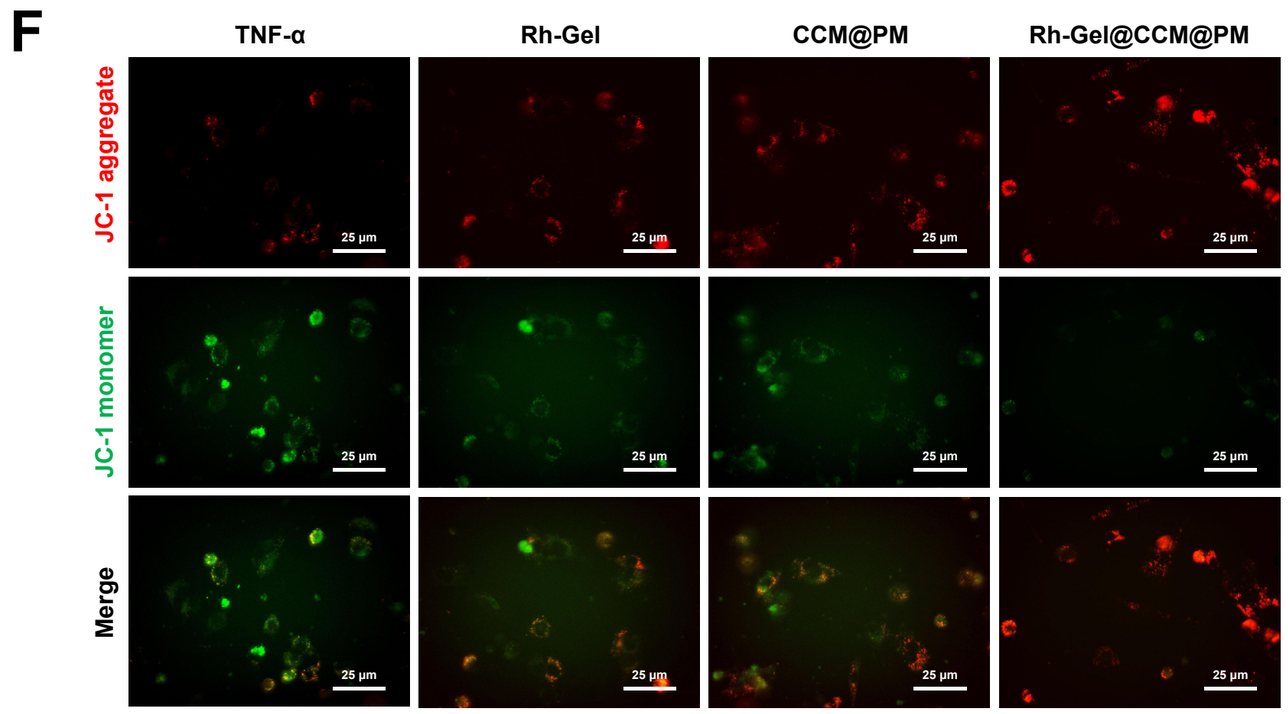
F
TNF-α
Rh-Gel
CCM@PM
Rh-Gel@CCM@PM
JC-1 aggregate
JC-1 monomer
Merge
25 μm

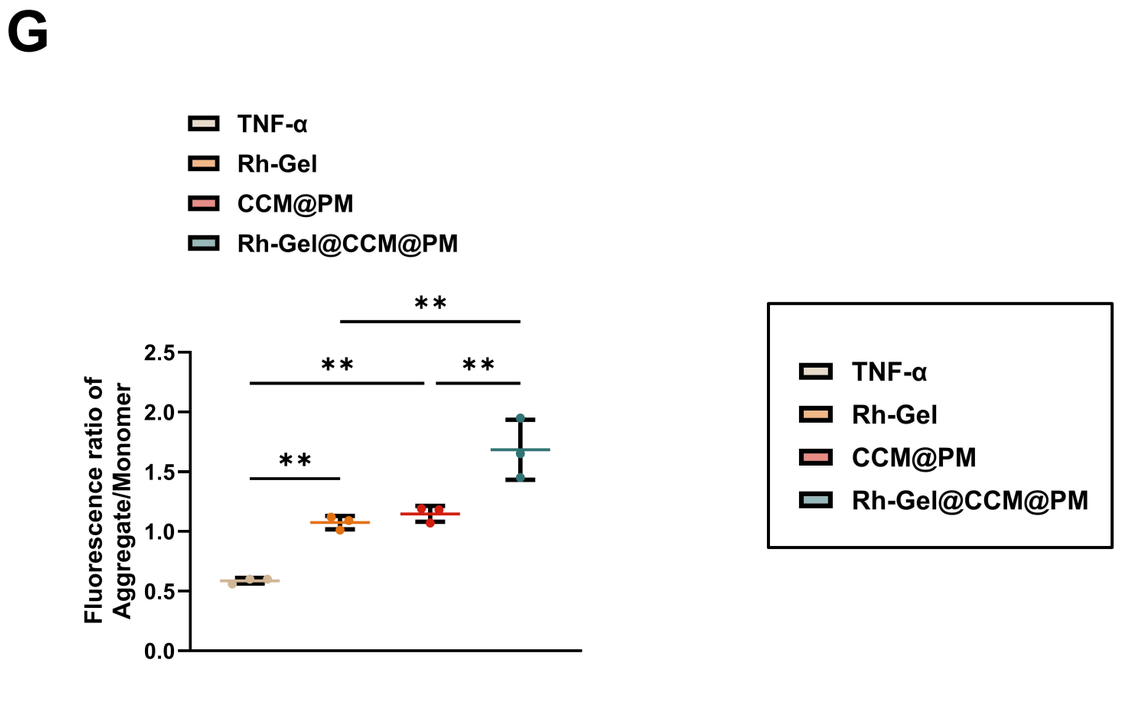
G
TNF-α
Rh-Gel
CCM@PM
Rh-Gel@CCM@PM
Fluorescence ratio of Aggregate/Monomer
**
**
**
**

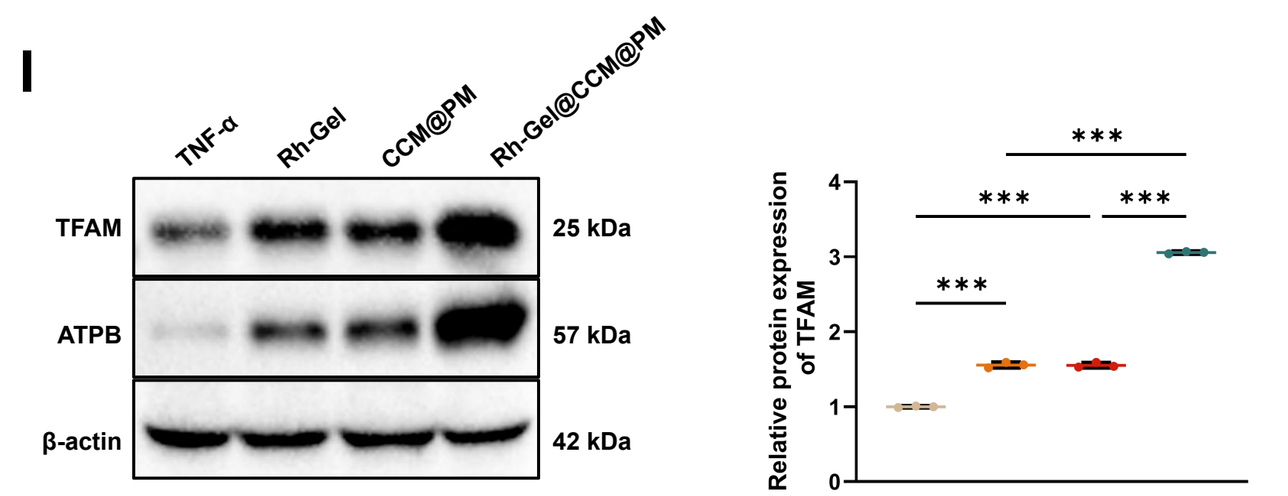
I
TNF-α
Rh-Gel
CCM@PM
Rh-Gel@CCM@PM
TFAM
25 kDa
ATPB
57 kDa
β-actin
42 kDa
Relative protein expression of TFAM
***
***
***
***
Relative protein expression of ATPB
***
***
***
***

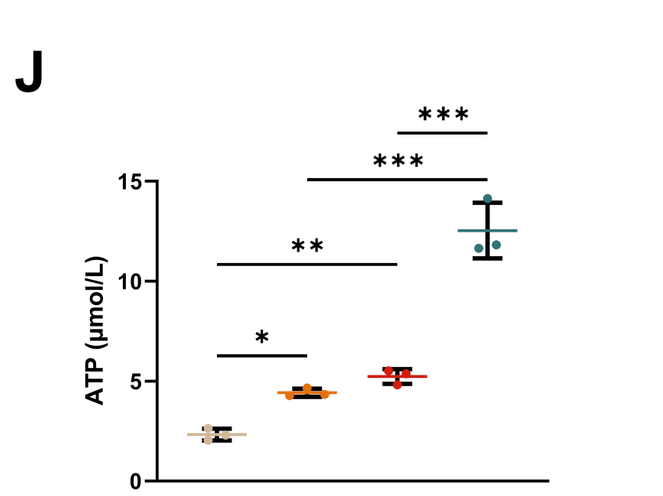
J
ATP (μmol/L)
***
***
**
*

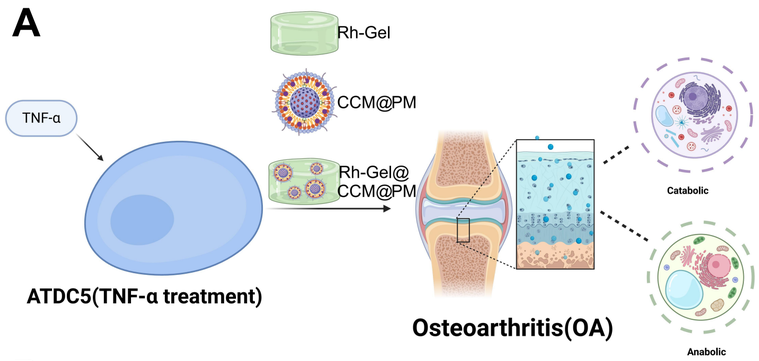
A
Rh-Gel
CCM@PM
Rh-Gel@
CCM@PM
TNF-α
ATDC5(TNF-α treatment)
Osteoarthritis(OA)
Catabolic
Anabolic

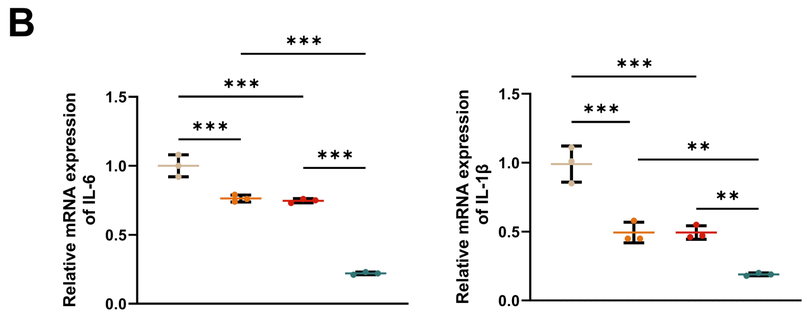
B
Relative mRNA expression of IL-6
Relative mRNA expression of IL-1β

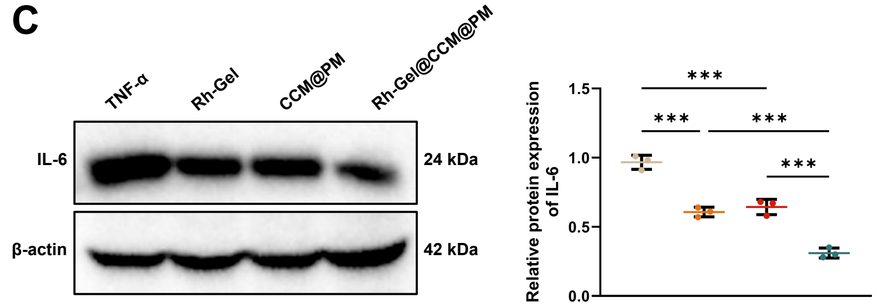
C
TNF-α
Rh-Gel
CCM@PM
Rh-Gel@CCM@PM
IL-6
24 kDa
β-actin
42 kDa
Relative protein expression of IL-6

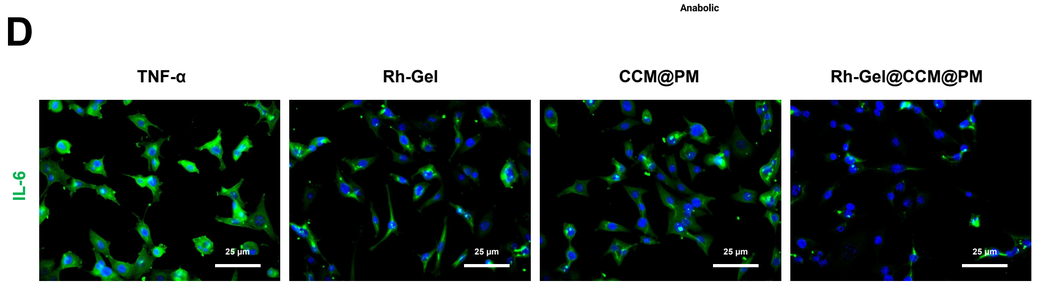
D
TNF-α
Rh-Gel
CCM@PM
Rh-Gel@CCM@PM
IL-6
25 μm
Fluorescence ratio of IL-6

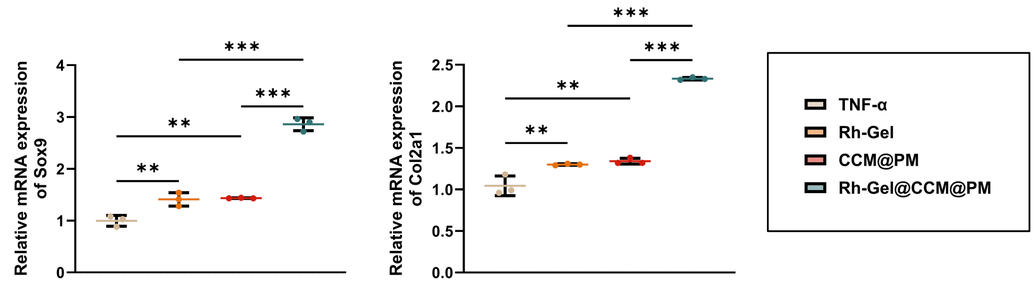
E
Relative mRNA expression of Sox9
Relative mRNA expression of Col2a1
TNF-α
Rh-Gel
CCM@PM
Rh-Gel@CCM@PM

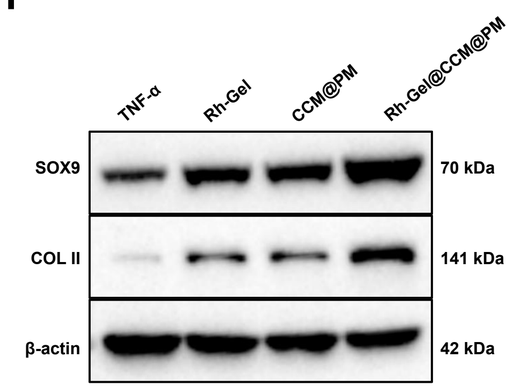
F
TNF-α
Rh-Gel
CCM@PM
Rh-Gel@CCM@PM
SOX9
70 kDa
COL II
141 kDa
β-actin
42 kDa

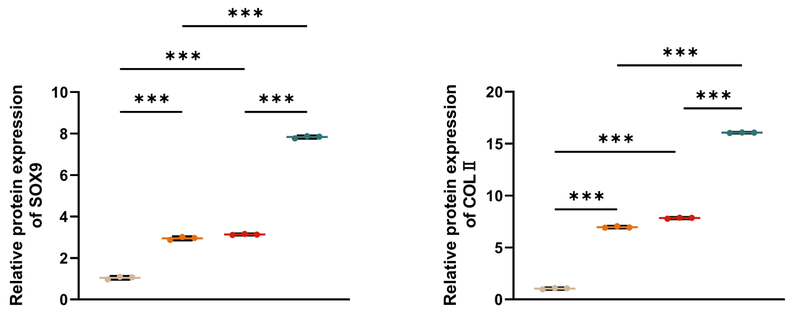
Relative protein expression of SOX9
Relative protein expression of COL Ⅱ

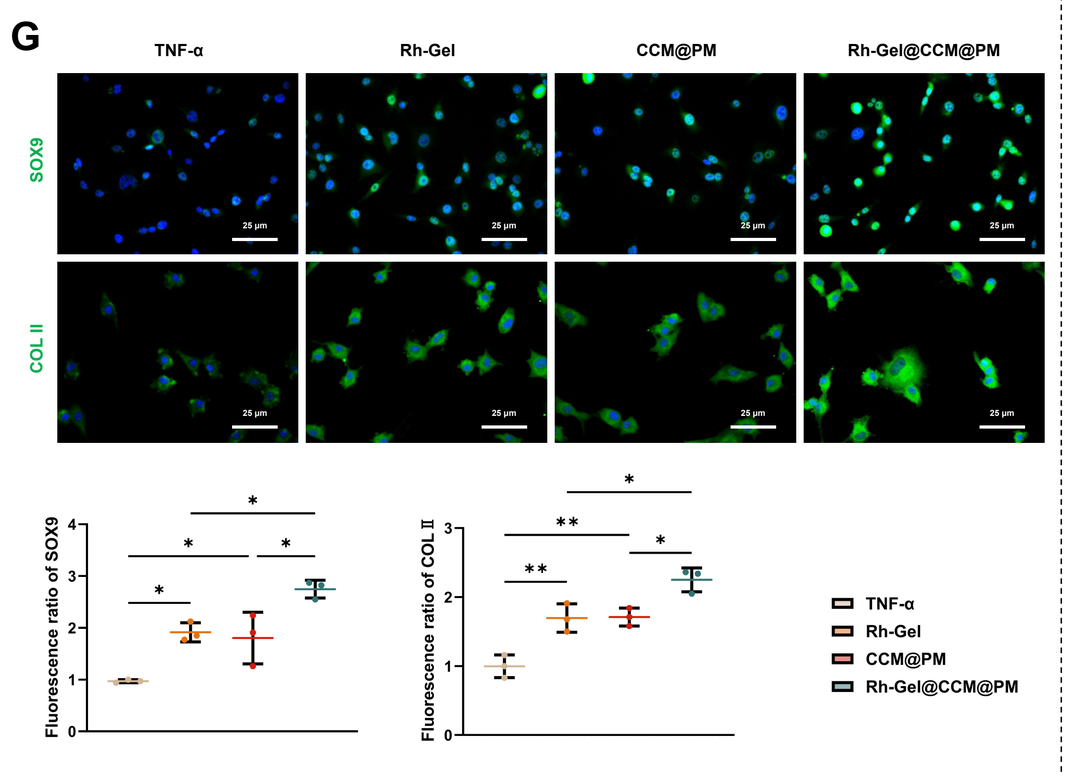
G
TNF-α
Rh-Gel
CCM@PM
Rh-Gel@CCM@PM
SOX9
COL II
25 μm
Fluorescence ratio of SOX9
Fluorescence ratio of COL Ⅱ
TNF-α
Rh-Gel
CCM@PM
Rh-Gel@CCM@PM

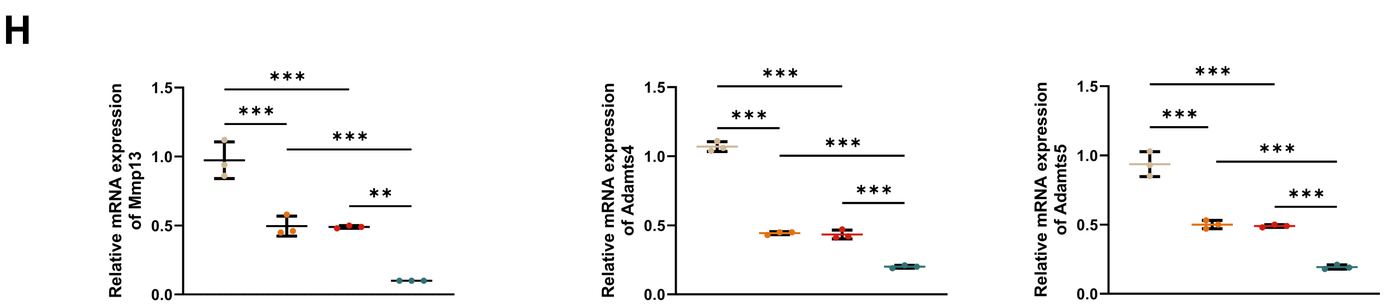
H
Relative mRNA expression of Mmp13
Relative mRNA expression of Adamts4
Relative mRNA expression of Adamts5

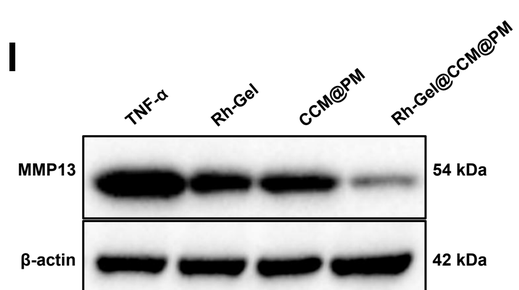
I
TNF-α
Rh-Gel
CCM@PM
Rh-Gel@CCM@PM
MMP13
54 kDa
β-actin
42 kDa

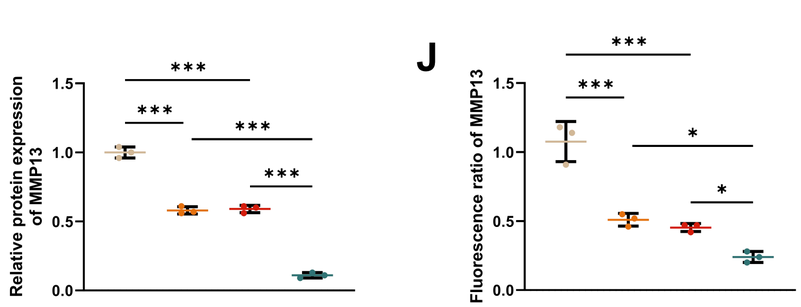
Relative protein expression of MMP13

J
Fluorescence ratio of MMP13

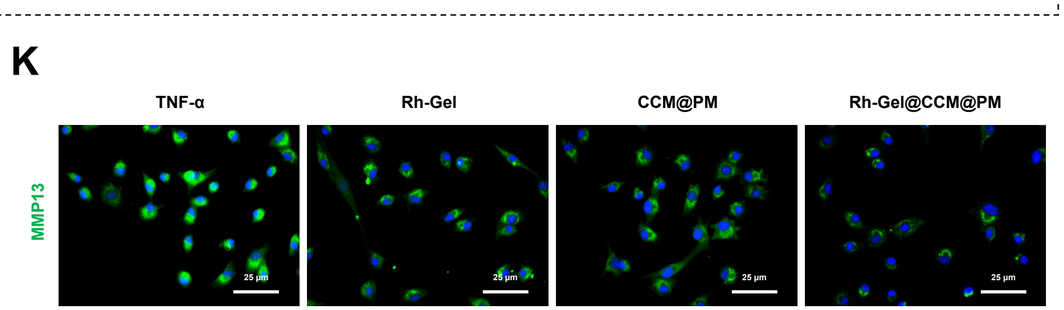
K
TNF-α
Rh-Gel
CCM@PM
Rh-Gel@CCM@PM
MMP13
25 μm

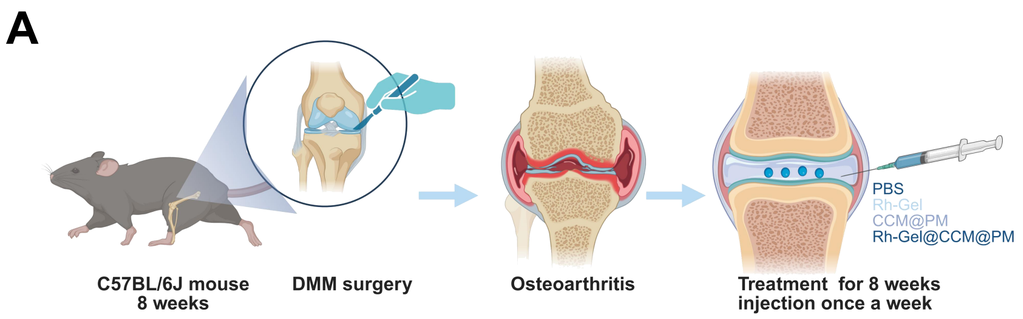
A
C57BL/6J mouse
8 weeks
DMM surgery
Osteoarthritis
Treatment for 8 weeks
injection once a week
PBS
Rh-Gel
CCM@PM
Rh-Gel@CCM@PM

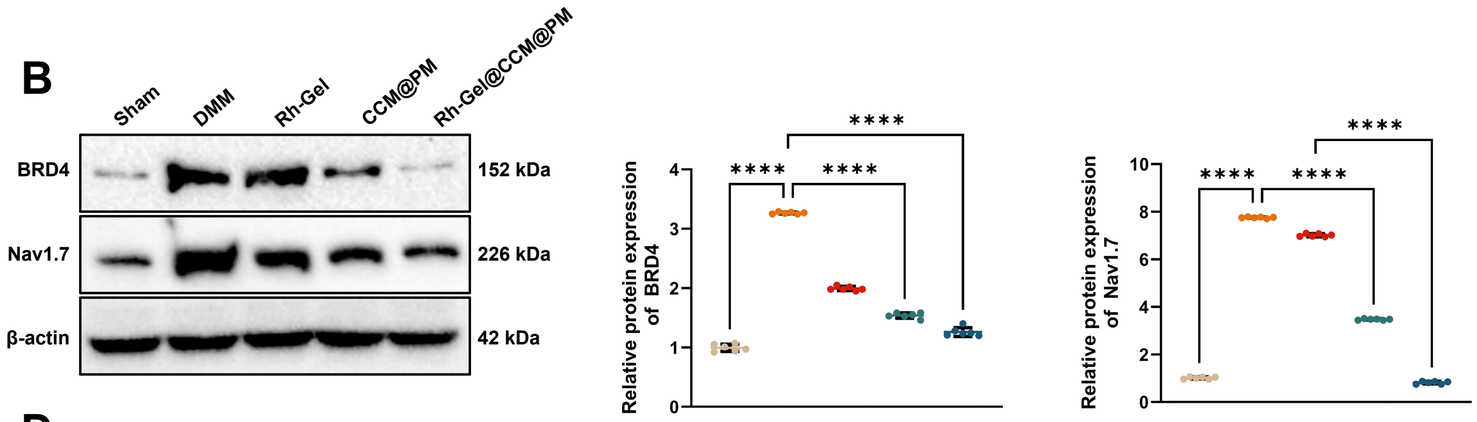
B
Sham
DMM
Rh-Gel
CCM@PM
Rh-Gel@CCM@PM
BRD4
Nav1.7
β-actin
152 kDa
226 kDa
42 kDa
Relative protein expression of BRD4
Relative protein expression of Nav1.7

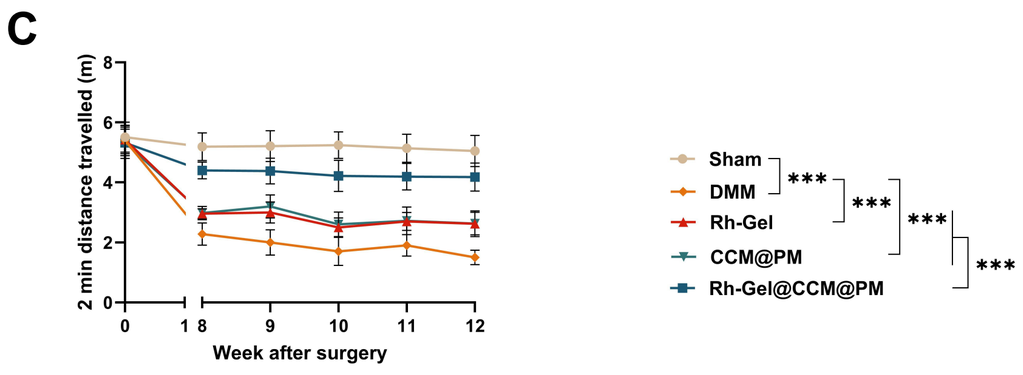
C
2 min distance travelled (m)
Week after surgery
Sham
DMM
Rh-Gel
CCM@PM
Rh-Gel@CCM@PM

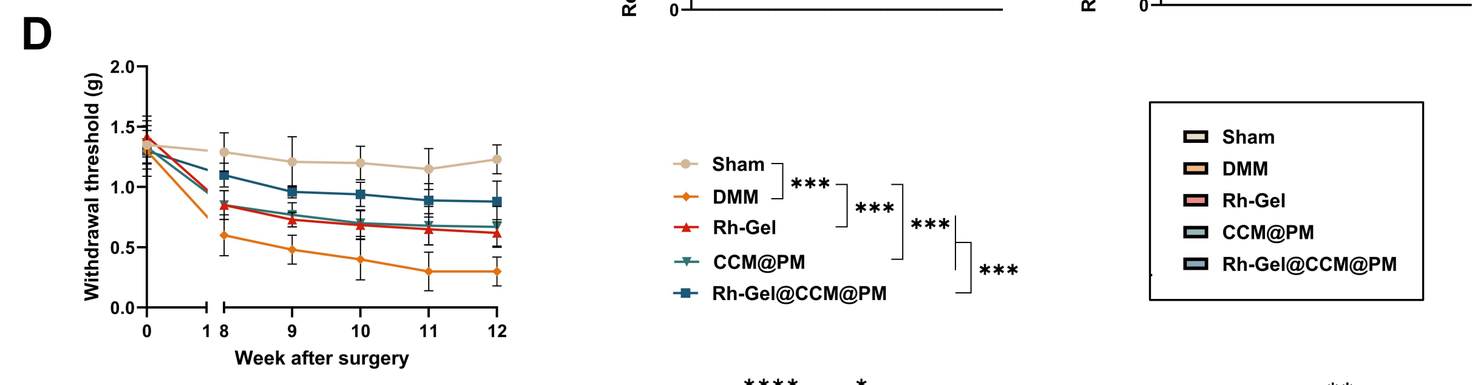
D
Withdrawal threshold (g)
Week after surgery
Sham
DMM
Rh-Gel
CCM@PM
Rh-Gel@CCM@PM

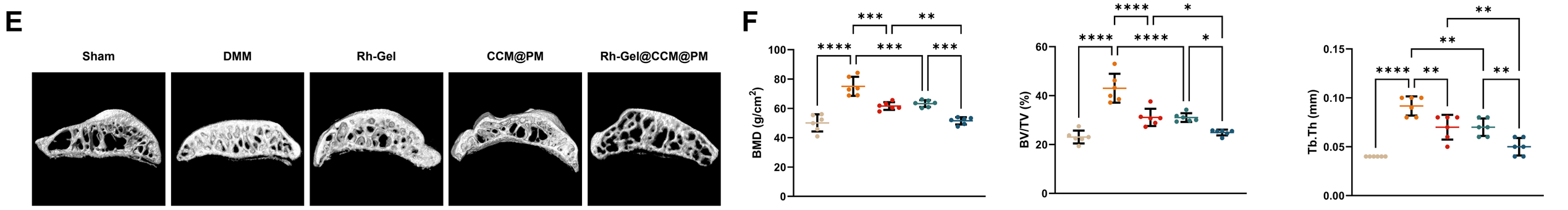
E
Sham
DMM
Rh-Gel
CCM@PM
Rh-Gel@CCM@PM
F
BMD (g/cm²)
BV/TV (%)
Tb.Th (mm)

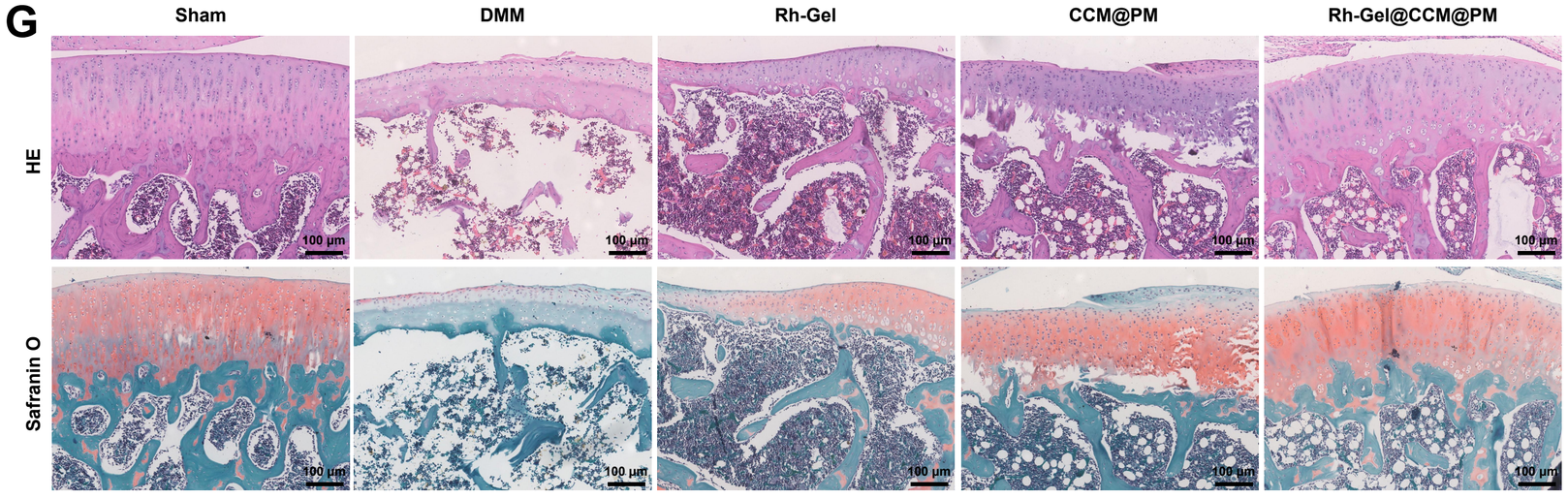
G
Sham
DMM
Rh-Gel
CCM@PM
Rh-Gel@CCM@PM
HE
Safranin O
100 μm

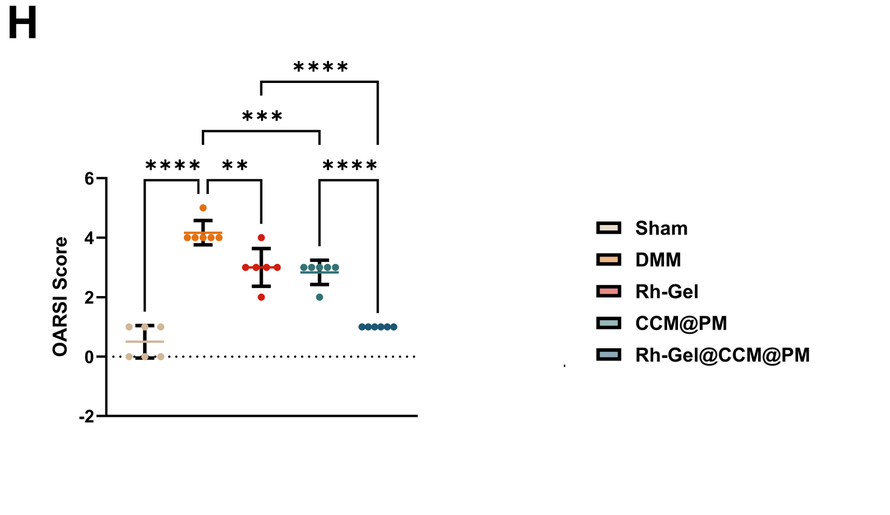
H
OARSI Score
Sham
DMM
Rh-Gel
CCM@PM
Rh-Gel@CCM@PM

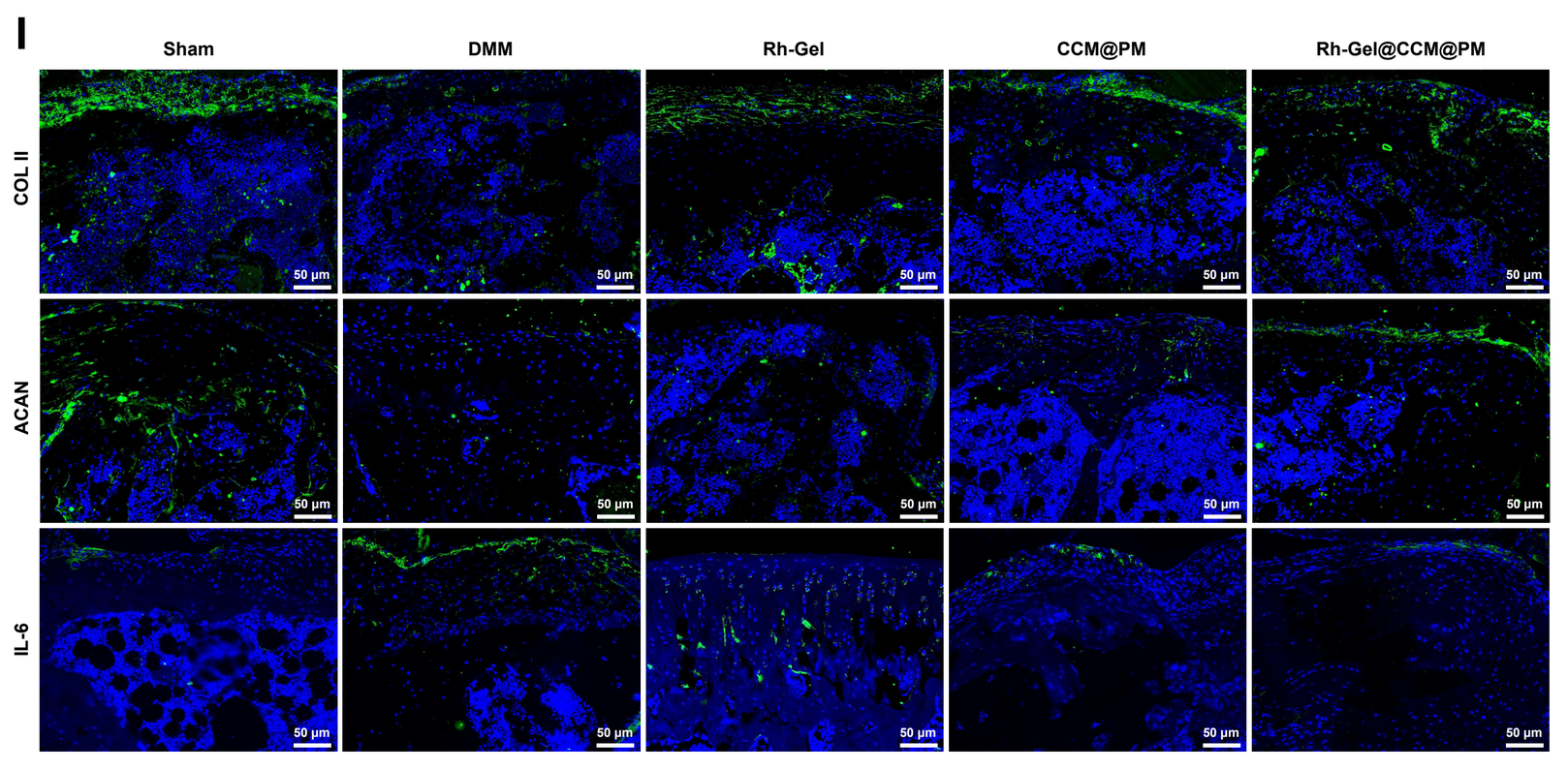
I
Sham
DMM
Rh-Gel
CCM@PM
Rh-Gel@CCM@PM
COL II
ACAN
IL-6
50 μm

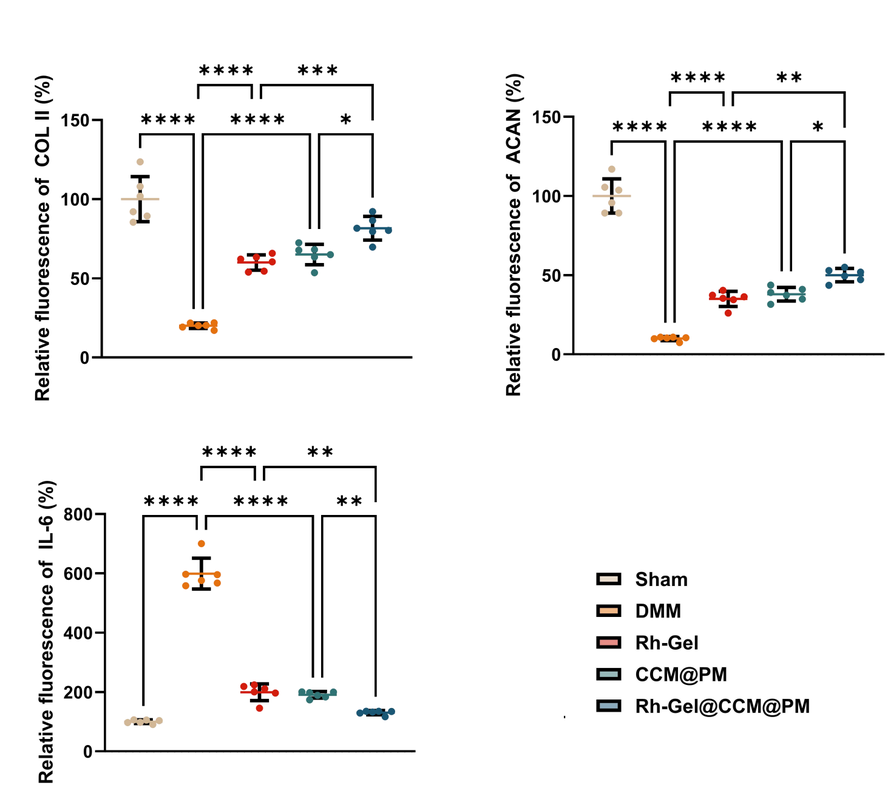
Relative fluorescence of COL II (%)
Relative fluorescence of ACAN (%)
Relative fluorescence of IL-6 (%)
Sham
DMM
Rh-Gel
CCM@PM
Rh-Gel@CCM@PM

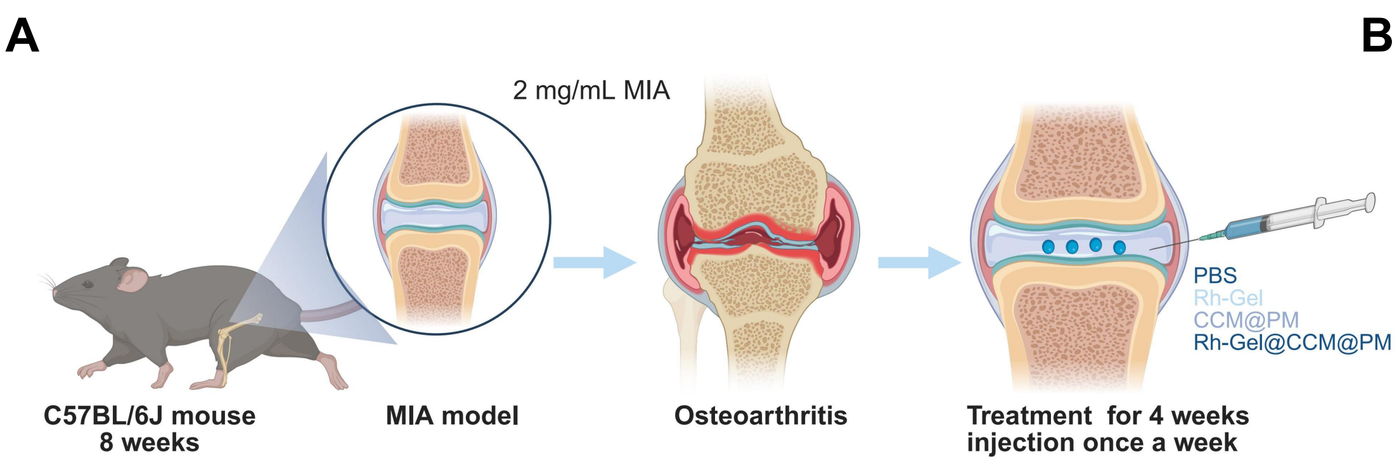
A
2 mg/mL MIA
C57BL/6J mouse
8 weeks
MIA model
Osteoarthritis
Treatment for 4 weeks
injection once a week
PBS
Rh-Gel
CCM@PM
Rh-Gel@CCM@PM

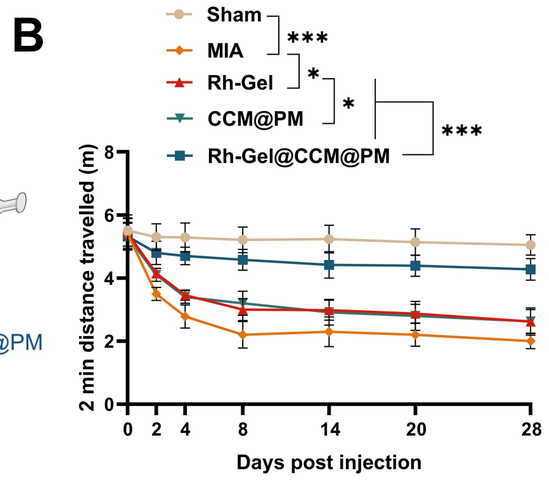
B
Sham
MIA
Rh-Gel
CCM@PM
Rh-Gel@CCM@PM
2 min distance travelled (m)
Days post injection

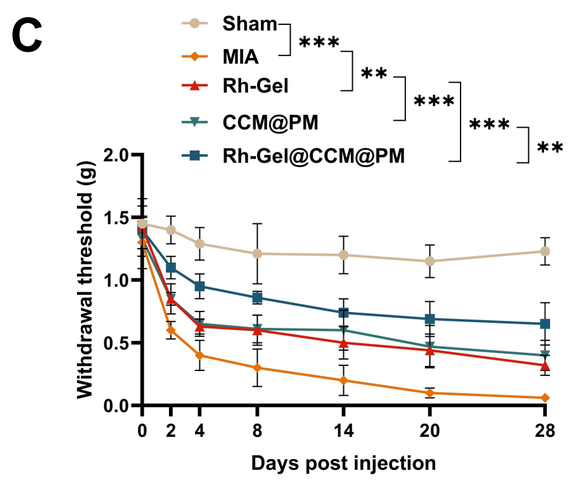
C
Withdrawal threshold (g)
Days post injection

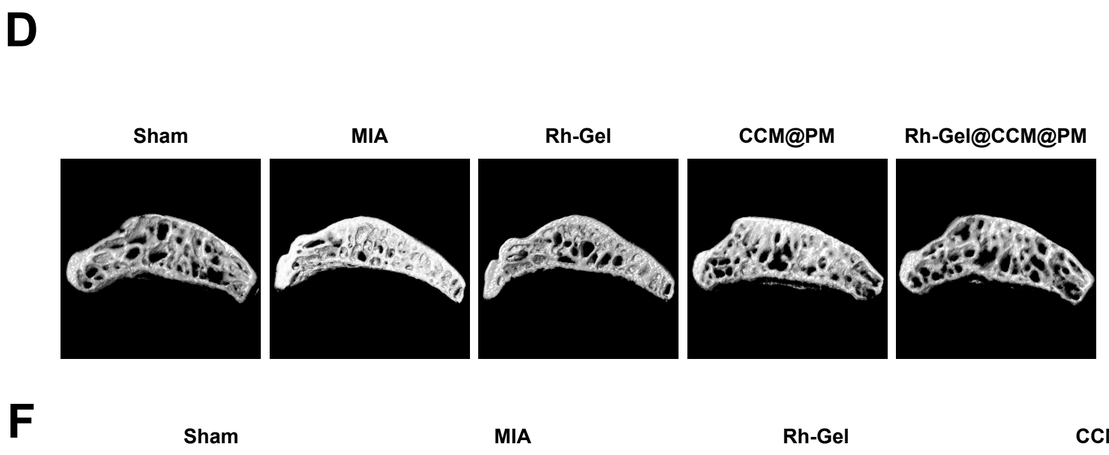
D
Sham
MIA
Rh-Gel
CCM@PM
Rh-Gel@CCM@PM

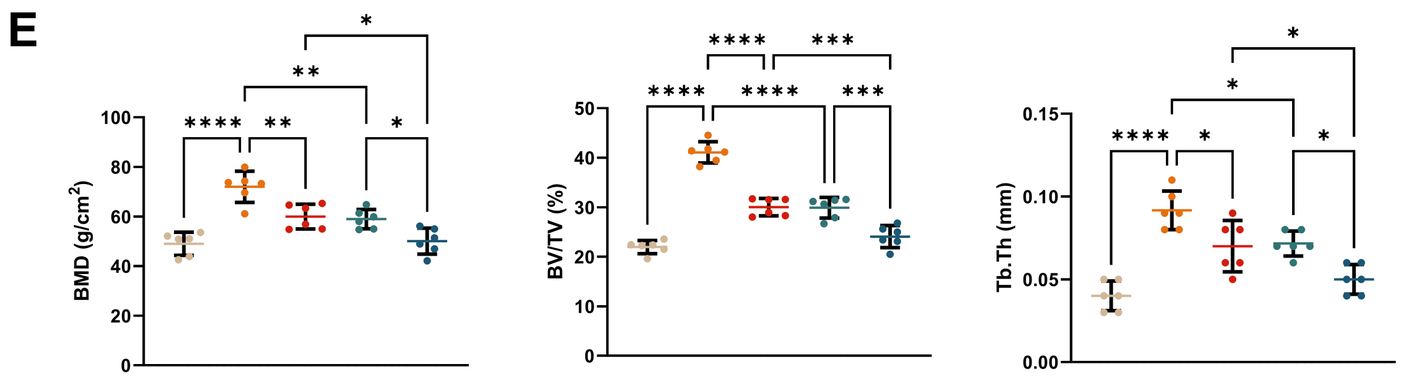
E
BMD (g/cm²)
BV/TV (%)
Tb.Th (mm)

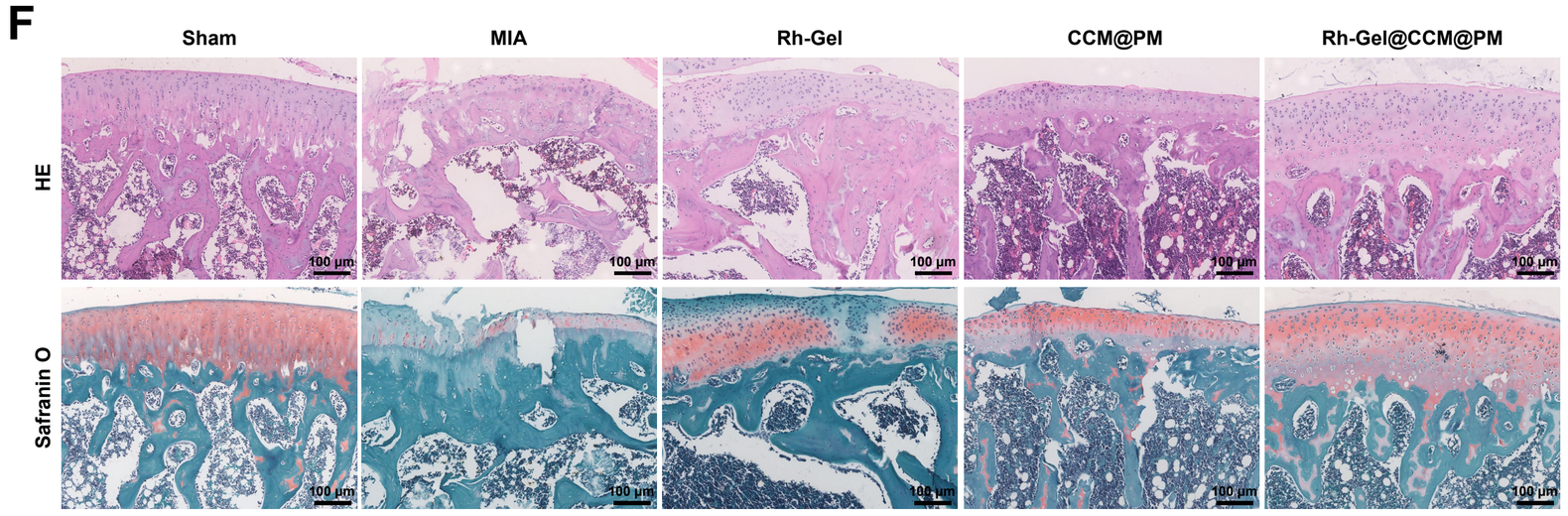
F
Sham
MIA
Rh-Gel
CCM@PM
Rh-Gel@CCM@PM
HE
Safranin O
100 μm

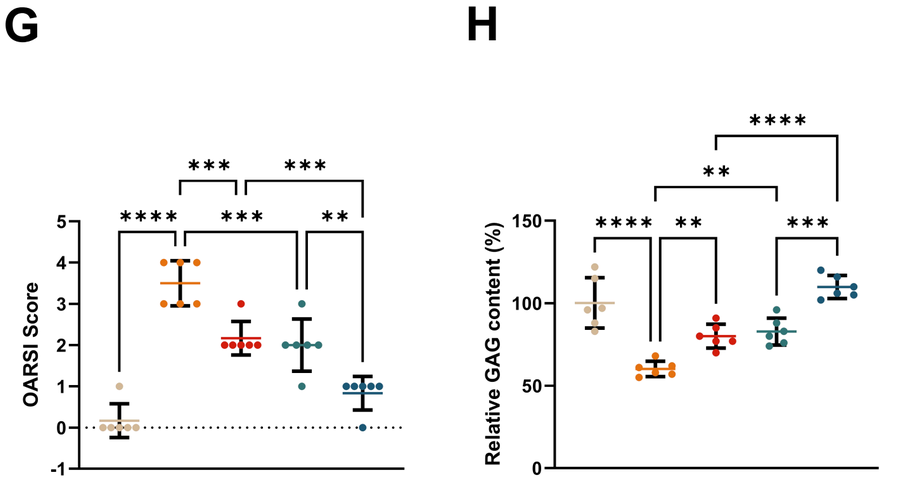
G
OARSI Score
H
Relative GAG content (%)

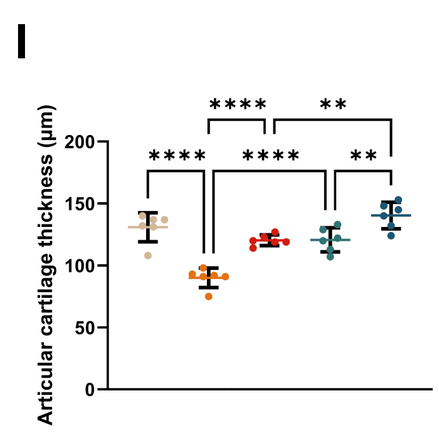
I
Articular cartilage thickness (μm)

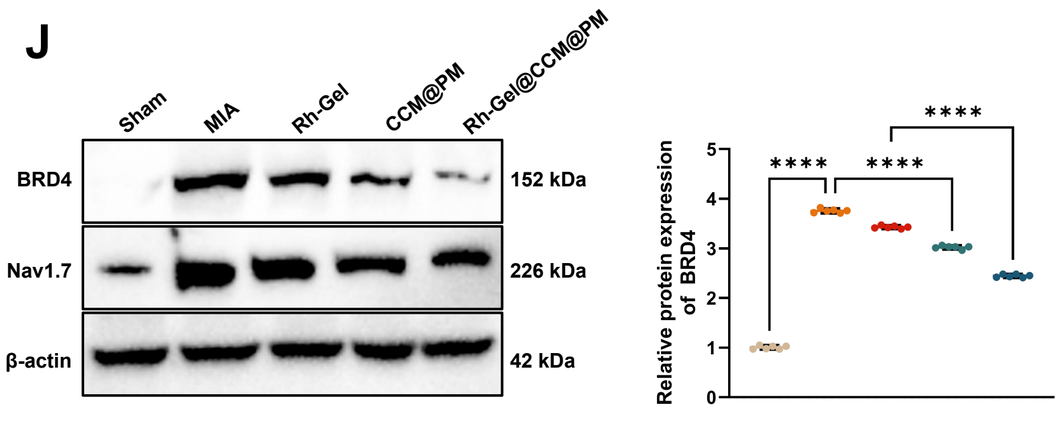
J
Sham
MIA
Rh-Gel
CCM@PM
Rh-Gel@CCM@PM
BRD4
Nav1.7
β-actin
152 kDa
226 kDa
42 kDa
Relative protein expression of BRD4
Relative protein expression of Nav1.7

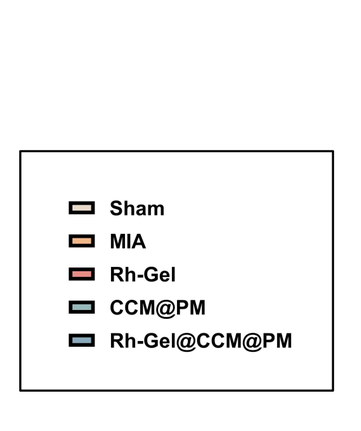
Sham
MIA
Rh-Gel
CCM@PM
Rh-Gel@CCM@PM

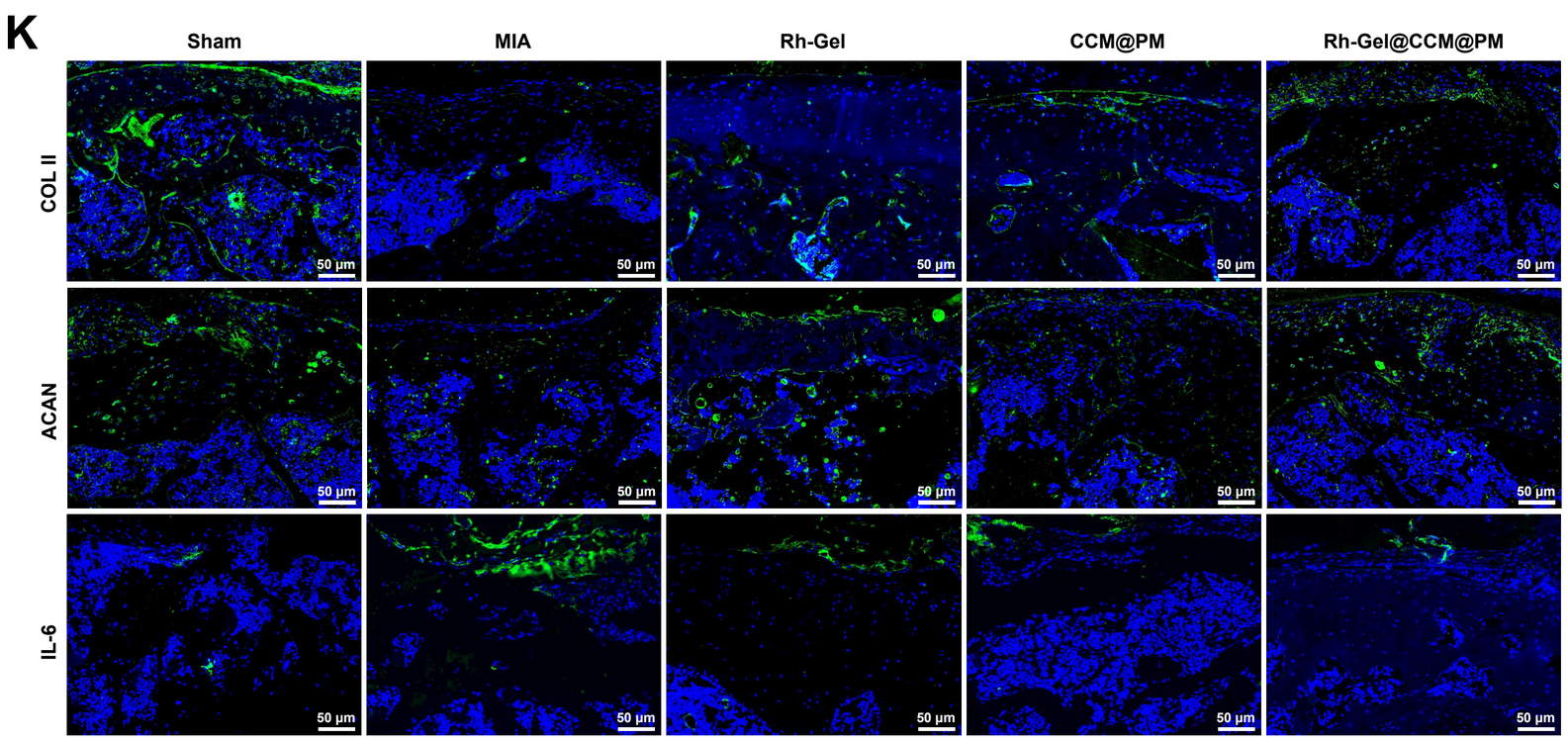
K
Sham
MIA
Rh-Gel
CCM@PM
Rh-Gel@CCM@PM
COL II
ACAN
IL-6
50 μm

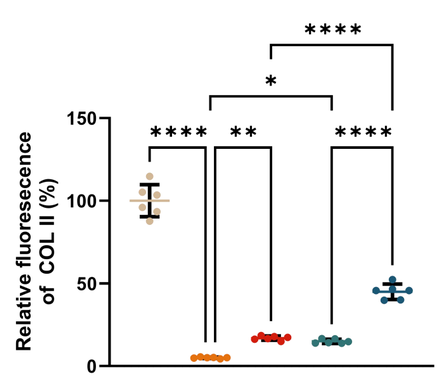
Relative fluorescence of COL II (%)

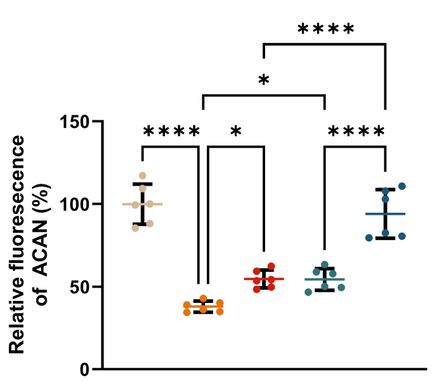
Relative fluorescence of ACAN (%)

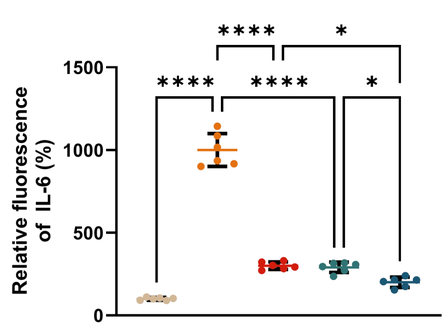
Relative fluorescence of IL-6 (%)

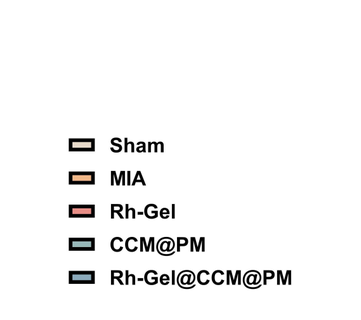
Sham
MIA
Rh-Gel
CCM@PM
Rh-Gel@CCM@PM

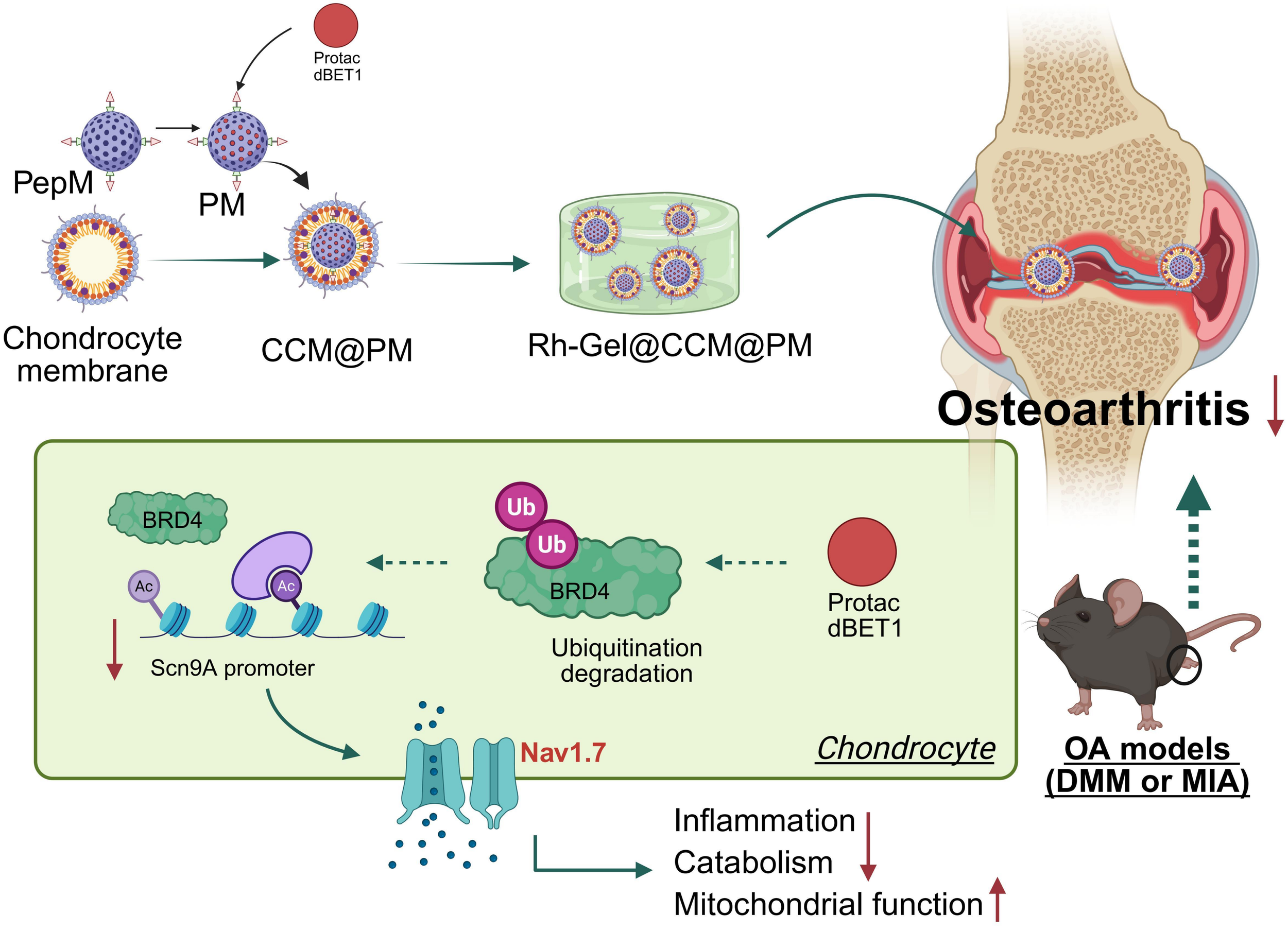
Protac
dBET1
PepM
PM
Chondrocyte
membrane
CCM@PM
Rh-Gel@CCM@PM
Osteoarthritis
BRD4
Ac
Ac
Scn9A promoter
Ub
Ub
BRD4
Ubiquitination
degradation
Protac
dBET1
Nav1.7
Chondrocyte
Inflammation
Catabolism
Mitochondrial function
OA models
(DMM or MIA)